THE UNIVERSITY OF CHICAGO

A SEARCH FOR THE EXTRAGALACTIC MAGNETIC FIELD VIA ITS INFLUENCE ON THE GAMMA-RAY SIGNALS FROM BLAZARS

A DISSERTATION SUBMITTED TO
THE FACULTY OF THE DIVISION OF THE PHYSICAL SCIENCES
IN CANDIDACY FOR THE DEGREE OF
DOCTOR OF PHILOSOPHY

DEPARTMENT OF PHYSICS

BY
THOMAS RAYMOND WEISGARBER

CHICAGO, ILLINOIS
JUNE 2012

ProQuest LLC.
789 East Eisenhower Parkway
P.O. Box 1346
Ann Arbor, MI 48106 - 1346

You bore me through a fog of years,
And now I walk, for I have run
A journey half complete, begun
By you, which love of wisdom steers.

TABLE OF CONTENTS

CHAPTER

APPENDIX

LIST OF FIGURES

LIST OF TABLES

ACKNOWLEDGMENTS

For my growth as a scientist, for my emotional stability, and for my continued fascination with the laws by which this universe is governed, I am indebted to innumerable individuals. I regret that, in the interests of economy, I cannot name them all in the space of these Acknowledgments. Nevertheless, the influence of those colleagues, friends, and family members who have guided and continue to guide me remains present in my thoughts.

For my intellectual development as a scientist, I am most grateful to my advisor, Scott Wakely. Of all the things he taught me, the most important is to focus on the simple explanations without which a truly deep understanding of the physics can never be cultivated. Scott was there when I needed him and absent when I didn't. Hao Huan, my friend and colleague, also helped me via many insightful discussions that lead to new approaches and new ideas. My interactions with Hao made me realize how valuable it is to have someone with whom I can toss around new ideas, no matter how crazy they sound. Steph Wissel, Brian Humensky, and Luis Reyes helped me immensely in finding my place at the University of Chicago and in embarking and continuing on the path of astroparticle physics research. I am also particularly grateful to the late Simon Swordy, whose unique perspective convinced me to come to Chicago in the first place, and who taught me that it is not only progress, but "progress plus initial conditions," that has made the world what it is today.

In addition to my advisor, Scott Wakely, I would like to thank the members of my thesis committee, Dietrich Müller, Carlos Wagner, and David Schuster, for taking time out of their busy schedules to meet with me and discuss my research. I would particularly like to thank Dietrich Müller for frequently stopping by my office with interesting questions.

My membership in the Very Energetic Radiation Imaging Telescope Array System (VERITAS) collaboration has inspired in me a sense of teamwork in addition to a fondness for inordinately contrived acronyms. Tim Arlen and Vladimir Vassiliev deserve my especial thanks for the hospitality they showed me on my two visits to UCLA, during which we tested much of the Monte Carlo simulation used in this work and discussed the interpretation of its results. Other members of VERITAS to whom I am grateful include, in no particular order, Ester Aliu, Taylor Aune, Reshmi Mukherjee, Nahee Park, Jeff Grube, Jamie Holder, Vikram Dwarkadas, and Daniel Gall.

Someone once told me that graduate school is the best time of your life. That may be so. Like any other aspect of life, however, it follows a pattern of highs and lows. The many friends that I have made while a graduate student have helped me through these trying times. I am grateful to Michael Herman and Austin Carter for going along with my crazy ideas and over-fondness for games, to Tomm Scaife for spelling his name with more m's than mine, and to Phil Killewald, the source of all sarcasm, for being patient enough to work on problems in quantum field theory with me. Thanks are due also to Wes Ketchum and Dave McCowan for keeping me in fine spirits, to Chris Williams for keeping me up to date on news and politics and trying to graduate before me, and to the members of Physics House, Ellen Martinsek, Joey Paulsen, Gabe Lee, and Emily Conover, for being interesting and entertaining roommates. My heartiest thanks go to Andreas Obermeier, who taught me that sometimes it's okay not to eat lunch at your desk, even though I'm doing exactly that as I write this, and to Peggy Eppink, who is one of the few people I know who is willing to follow nearly any spontaneous suggestion at least once. I could not have hoped[1] for a better pair of friends with whom to ride in a convertible in winter or be off in our back-of-the-envelope calculations by more than fifteen orders of magnitude.

I also owe special thanks to Sandy Heinz. When I first came to Chicago, it was a challenging time for me personally, and I felt overwhelmed settling into a new routine. Sandy set me up in the visitors' office, helped me figure out how to get around Chicago, and made me feel right at home. As someone who knows everything about how the university works, Sandy has been both essential and a good friend.

A few individuals deserving of thanks defy classification and so I include them here. I thank Jim Beatty for advising me to apply to the University of Chicago, the members of the Astroparticle Journal Club for choosing interesting topics for review, Linn Van Woerkom, Enam Chowdhury, and Patrick Randerson for encouraging me during my undergraduate years and making physics fun, Randy Balch for calling every few months to remind me that I haven't graduated yet, Kit and Possamer for their unswerving devotion, and the Hausen for maintaining the logical operation of physics in the observable universe.

I owe eternal thanks to Nahee Park for her patience during these past few months, and apologies for assuming she was a professor when we first met. Thanks to Nahee, the past year or so has been one of the most exciting and happiest times of my life. She possesses

---

[1] In any reasonable sense.

an aggravating but honest frankness about my ability to discuss physics. While now I may not be matching her in rank, at least I will have attained the same educational level. It is my sincere hope that for us the friendship of the past and the excitement of the present may actualize all of the promise of the future.

Most importantly, I thank my family for their love and devotion throughout my life. My parents taught me to be imaginative and disciplined. My brother Michael, through long suffering, taught me compassion and empathy. Grandma Alice taught me to be curious and Grandma Dawn taught me to be self-reliant. All of them taught me love. Together, their support has been the garden within which the seeds of my knowledge took root and grew. What they have done for me I hope also I have done for them.

ABSTRACT

Observations of the galaxies, clusters, and filaments of the large-scale structure (LSS) of the universe reveal that these objects possess magnetic fields exhibiting complicated structure with strengths on the order of a microGauss. Recent observations have also begun to shed light on the extragalactic magnetic field (EGMF), which is believed to exist in the voids that likely comprise the majority of the LSS. Such a field could have been generated primordially, for instance during phase transitions in the early universe. In this case, its detection and characterization could reveal information about conditions in the early universe. A primordially generated field is also physically compelling because many models of magnetic field formation in galaxies require an initial seed field, a role that can be readily filled by an EGMF existing prior to galaxy formation. Alternatively, astrophysical mechanisms have been proposed to generate the EGMF via bulk outflows of magnetized plasma from active and starburst galaxies. In this case, the detection of an EGMF would provide evidence for the unexpected efficiency in the transport of magnetic energy into the voids.

Over the past few decades, the development of ground-based gamma-ray astronomy has opened many new opportunities to study the universe at high energies. One such opportunity involves a recently developed technique exploiting the observations of distant blazars to measure or constrain the EGMF. Because of the cosmological distances that they must cross to propagate to Earth, very-high-energy gamma rays from blazars are attenuated by their interactions with the extragalactic background light and cosmic microwave background radiation. Due to this attenuation, an electromagnetic cascade of electrons, positrons, and gamma rays arises in extragalactic space. The deflection of the electrons and positrons by the EGMF ultimately produces two effects on the secondary gamma rays in the cascades. These gamma rays are delayed in time with respect to a primary gamma ray that travels directly from the source to Earth, and they form an angular distribution, or "halo," around what would otherwise appear as a pointlike blazar.

In this work, I develop a new method for accurately quantifying the extended gamma-ray halo that arises due to the influence of the EGMF on the extragalactic cascades. This method is sensitive to EGMF strengths between 3×10^{-17} and 10^{-14} Gauss. I compare the predictions from a Monte Carlo simulation to combined data from ground-based imaging atmospheric Cherenkov telescopes and the *Fermi* Gamma-Ray Space Telescope in an attempt to measure or constrain the properties of the EGMF. Depending on certain assumptions about the source lifetime, I interpret the absence of any detectable gamma-ray halo around the blazars RGB J0710+591 and 1ES 0229+200 as evidence for an EGMF with a strength greater than 3×10^{-15} Gauss. This represents the strongest firm lower limit on the EGMF strength at the present time.

CHAPTER 1

EXTRAGALACTIC MAGNETIC FIELDS

Large-scale magnetic fields are common throughout the universe. Within our own Galaxy, numerous measurements have revealed a rich structure of magnetic fields via such diverse techniques as the detection of polarized starlight, synchrotron emission from populations of relativistic electrons, Zeeman splitting of absorption lines, and the wavelength-dependent Faraday rotation of light from extragalactic sources. These observations indicate that the Galactic magnetic field strength is on the order of a few μGauss, with both large-scale and random components (Beck, 2008).

As might be expected, outside of the Galaxy, magnetic fields trace the matter distribution in the large-scale structure (LSS) of the universe remarkably well. Galaxies in the LSS are grouped into large regions known as clusters, which are connected by relatively thin regions of galaxies known as filaments. Surrounding the clusters and filaments are the mostly empty void regions that comprise the majority of the volume of the universe. Observations of polarized synchrotron radiation from galaxies and clusters provide an *in situ* measurement of the magnetic field and have been used to demonstrate that magnetic fields on the order of 0.1 to 10 μGauss exist in nearly all galaxies and clusters (Widrow, 2002). Somewhat surprisingly, the intracluster fields can be just as strong, if not stronger, than the galactic fields. Magnetic fields in the filaments have also been measured in at least one instance near the Coma cluster (Kim et al., 1989; Kronberg et al., 2007). In general, the detection of these fields rules out still higher field strengths in the voids.

In spite of the many measurements of magnetic fields in galaxies and clusters, a positive detection of the extragalactic magnetic field (EGMF), presumed to exist in the voids, remains elusive. Theoretical motivation for the existence of this field comes from a variety of sources. The existence of an EGMF during the epoch of galaxy formation could provide the seed fields necessary for many models of galactic magnetic field formation (Grasso & Rubinstein, 2001). One possible source of the EGMF is from phase transitions in the early universe, during which the misalignment between density and pressure gradients in the plasma can generate a field via the Biermann battery mechanism (Biermann, 1950). Alternative scenarios in which the EGMF is generated due to the bulk transport of magnetized plasma from the lobes of active galaxies or other astrophysical sources have also been proposed (Kronberg, 1994; Kronberg et al., 2001).

If it is generated through astrophysical processes, the EGMF is expected to have a very small strength. To get a sense of what small means in this context, it is helpful to consider a very simple case in which the magnetic field of a galaxy is approximated by a dipole. Let us take the characteristic size of the galaxy to be 10 kpc and assume that the dipole field at this distance is 1 μGauss. If the galaxy is located on the edge of a void whose center is 10 Mpc away, then the distance from the galaxy to the center of the void is a factor of 10^3 times larger than the size of the galaxy. Consequently, the dipole field, which decreases with the cube of the distance from the dipole, will be reduced by a factor of 10^9 to a magnetic field strength of 10^{-15} Gauss.

However, the dipole approximation applied to galactic fields is likely to be quite poor. Observationally, the field strength in the galaxy does not fall with the cube of the distance, but is relatively constant throughout the galactic plane. The conventional explanation for these observations is that galactic magnetic fields are formed via magnetohydrodynamic processes in the galaxy (Widrow, 2002). In the limit of large conductivity, magnetic field lines are "frozen in" to the plasma in the galaxy and can be stretched and enhanced by the bulk movement of the plasma due to the differential rotation of the galaxy. The magnetic field outside the galaxy is then expected to be much weaker than the simple estimate supplied by the dipole approximation.

If the source of the EGMF is primordial instead of astrophysical, then the problem of its generation is moved from the present day to the early universe. In some sense this makes the problem easier, since collective effects in the plasma of the early universe can generate the field. A magnetic field of any strength generated in the early universe can survive to the present day, provided that its correlation length is sufficiently large to overcome magnetic diffusion.

Faraday rotation and Zeeman splitting measurements of the light from distant quasars rule out the existence of an EGMF with a strength greater than the Galactic field. When the effects of the Galactic magnetic field are subtracted from these measurements, upper limits on the EGMF strength remain. However, until recently, no lower limits on the EGMF strength existed. In this work, I focus on a newly developed method that enables a search for the dominant component of the EGMF in the void regions of the LSS. The method relies on gamma-ray observations of blazars, active galactic nuclei (AGN) with a jet oriented along or near the line of sight. Blazars that are detected at energies above 1 TeV can produce electromagnetic cascades via interactions with background photons, and observations of the secondary gamma rays from these cascades can then be used to place limits on the strength of the EGMF. In some cases, it may be possible to measure the EGMF via these observations.

Unless otherwise specified, throughout the rest of this work, I use the term EGMF to denote the dominant component of magnetic fields in the voids, ignoring the fields in the rest of the LSS.

1.1 EGMF Formation

The motivation for detecting the EGMF is intricately connected to its method of production and its relationship to the fields detected in galaxies and clusters. If the EGMF is of primordial origin, it may have been produced during the electroweak or quantum chromodynamic phase transitions, during inflation, or via exotic processes such as the generation of primordial vorticity by cosmic strings (Grasso & Rubinstein, 2001). In general, these processes are invoked to generate electric fields and density fluctuations necessary for the operation of the Biermann battery or similar mechanisms. The measurement of a primordially generated EGMF would provide insights into conditions in the early universe. Additionally, several researchers have suggested theoretical mechanisms that could amplify extragalactic "seed fields," explaining the formation of the observed galactic and cluster fields, and a primordial EGMF could provide these seed fields. One popular mechanism, the "α-ω dynamo," relies on the differential rotation of galaxies to stretch and enhance the field lines. The dynamo operates by stretching poloidal components of the field into toroidal components via differential rotation of matter in the galaxy, and also by converting toroidal components into poloidal components via helical disturbances in the flow of the plasma carrying the field lines. These two effects lead to an overall enhancement of the initial seed field, possibly by many orders of magnitude, into the observed field in the galaxy (Widrow, 2002). While dynamo models may be challenged by the detection of μG-scale fields in galaxies at redshifts $z \gtrsim 2$ (Bernet et al., 2008), the existence of fields in irregular galaxies with slower rotation than spiral galaxies (Kronberg, 1994), and the generation of cluster fields, it may be possible to find methods to enhance dynamo efficiency, for example through a careful treatment of effects due to turbulence (Ryu et al., 2008).

Alternatively, the EGMF could be produced by bulk magnetic outflows from starburst galaxies (Kronberg, 1994) or AGN (Kronberg et al., 2001). In this case, a measurement of the EGMF would constrain the efficiency of processes that transport magnetic energy from galaxies into the intergalactic medium (IGM) (Kronberg, 2001). This astrophysical origin hypothesis lacks an attractive explanation for the formation of galaxy and cluster fields, but this is not an insurmountable problem since there exist alternatives to the α-ω dynamo mechanism and for which a seed field is unnecessary (Kulsrud et al., 1997a,b). Whereas a primordially generated EGMF can trivially fill the entire volume of the observable universe, it remains unclear whether the astrophysical processes that have been proposed are sufficiently efficient to magnetize a substantial portion of the voids of the LSS (Kronberg et al., 2001; Zweibel, 2006).

1.2 Evolution of the EGMF

In the absence of dissipative effects and source terms, the EGMF strength evolves as

$$B(t) = B(t_0)\left(\frac{a(t_0)}{a(t)}\right)^2 = B(t_0)(1+z)^2, \tag{1.1}$$

where a is the scale factor, z is the redshift, t is the cosmic time, and t_0 refers to the present day (Grasso & Rubinstein, 2001). A simple derivation of Equation 1.1 can be made by noting that the energy density of the EGMF should behave like radiation during the universal expansion; that is, it should scale with $(1+z)^4$. Since the energy density is proportional to B^2, it follows that the field scales as $(1+z)^2$, as indicated by the equation.

Throughout the rest of this work, the EGMF strength B refers to the field strength at the present day, $B(t_0)$, and I assume that Equation 1.1 accurately describes the evolution of the field strength for $z \lesssim 0.5$. If the EGMF is of primordial origin, then Equation 1.1 must hold for very large redshifts as well. One possible effect that could modify Equation 1.1 is magnetic diffusion, which operates on time scales of $\tau \approx \mu\sigma L^2$ for a field uniform over a distance L in a medium of conductivity σ and magnetic permeability μ (Jackson, 1999). As long as the diffusion time scale τ is significantly longer than the age of the universe, it is reasonable to assume that the magnetic field could survive from the early universe until the present day. However, at sufficiently small length scales, below 10^{-5} pc or so, primordial

EGMFs will decay in less than a Hubble time (Neronov & Semikoz, 2009).

1.3 Limits on the EGMF

The primary properties of the EGMF that are of interest are its strength B and correlation length L, the distance at which the correlation between field directions drops to $1/e$ of its value at zero distance. Formally, the correlation length can be defined via the equation

$$\left\langle \int d\hat{n}\vec{B}(\vec{x}) \cdot \vec{B}(\vec{x} + L\hat{n}) \right\rangle = \frac{1}{e} \left\langle \vec{B}(\vec{x}) \cdot \vec{B}(\vec{x}) \right\rangle \int d\hat{n}, \tag{1.2}$$

where $\vec{x}$ is a position in space, $\hat{n}$ ranges over all possible directions, and the averages are taken over all space.

To quantify the strength of the EGMF, it is convenient to introduce the cumulative volume filling fraction $V(B)$, defined as the fraction of the volume of the universe that is filled by a magnetic field with a strength no greater than B[1]. Magnetohydrodynamic simulations of the generation of fields in the LSS (see, for example, the work of Sigl et al. (2004) or Dolag et al. (2005)) disagree on the precise shape of $V(B)$ but suggest that it rises rapidly from small values up to nearly unity around $B \approx 10^{-13}$ to $B \approx 10^{-11}$ G. However, the primary goal of these simulations is to reproduce the observed fields of the local structure, not to identify the fields in the voids, and the seed fields that lead to these shapes for $V(B)$ are tuned to give appropriate values in the LSS. Dolag et al. (2011) produce some simulations, for instance, that are consistent with EGMF strengths as low as 10^{-16} Gauss.

Figure 1.1 summarizes the limits on L and B as they were known in 2009. The dark gray exclusion regions apply for a general EGMF, while the light gray exclusion region applies for an EGMF of primordial origin. The correlation length is limited from above only by the particle horizon and from below by the time scale for magnetic diffusion becoming smaller than the age of the universe (Grasso & Rubinstein, 2001). Zeeman splitting measurements of absorption lines in the spectra of distant quasars constrain the EGMF to be no stronger than the Galactic magnetic field, independent of the correlation length (Neronov & Semikoz, 2009), while for correlation lengths above $L \approx 100$ pc, measurements of the wavelength-

---

[1] With this definition, obviously $V(B \leq 0) = 0$ and $V(B)$ increases monotonically to $V(B \to \infty) = 1$.

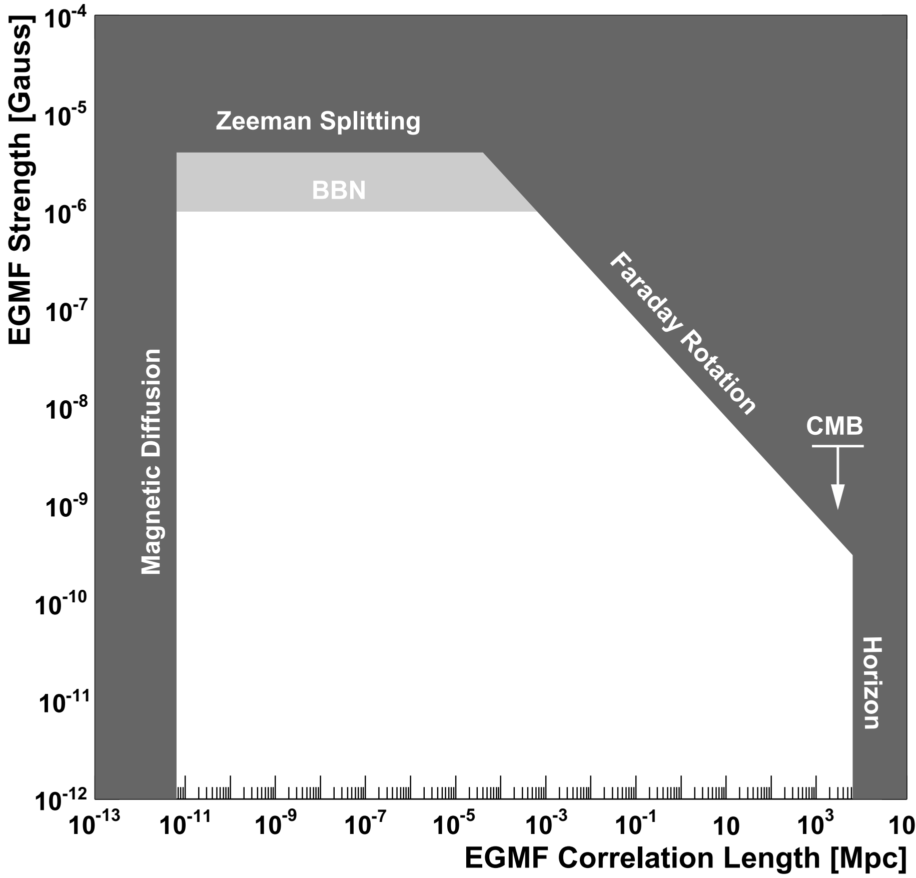

Figure 1.1: Existing limits on the EGMF strength and correlation length, adapted from Neronov & Semikoz (2009).

dependent Faraday rotation of left and right circularly polarized light provide a stronger constraint on B (Kronberg & Perry, 1982; Blasi et al., 1999).

It is possible to limit the present-day strength of a primordially generated EGMF due to the absence of an observed global anisotropy in measurements of the cosmic microwave background (CMB). This limit depends on the unknown power spectrum of the EGMF, so it is displayed in the figure as an upper limit on an EGMF uniform over all space. Additionally, the success of big bang nucleosynthesis limits the EGMF because a primordial magnetic field would accelerate the expansion of the universe, leading to the overproduction of helium and the underproduction of heavier elements (Grasso & Rubinstein, 2001; Widrow, 2002). This limit obviously applies only to a primordially generated field and appears as a light gray exclusion region in Figure 1.1.

1.4 Measuring the EGMF

Figure 1.1 lacks any lower bounds on the strength of the EGMF. The observations therefore permit a very wide range of acceptable values for B; logarithmically speaking, this range is unbounded from below. Until recently, no lower limits on the strength of the EGMF existed. However, the recent development of experimental gamma-ray astrophysics has opened up a new window on the universe, through which glimpses of the EGMF are beginning to appear. These glimpses arise through the influence of the EGMF on electromagnetic cascades that develop in extragalactic space due to the interaction of primary gamma rays with the isotropic populations of background photons. Aharonian et al. (1994) pointed out that these cascades would appear as a "halo" of extended emission around otherwise pointlike sources of gamma rays due to the action of the EGMF, and Plaga (1995) realized that time delays, or "echos" from flaring sources could probe very small EGMF strengths, possibly as low as 10^{-24} Gauss.

More recently, several studies have explored the dependence of the extended cascade emission on the EGMF, either through Monte Carlo simulations (Eungwanichayapant & Aharonian, 2009; Elyiv et al., 2009; Dolag et al., 2009) or analytic models with simplifying approximations (Neronov & Semikoz, 2007, 2009; Ahlers, 2011). Neronov & Semikoz (2009) also investigated the sensitivity of gamma-ray telescopes to the EGMF signature in the cascades by studying the pair production and inverse Compton interactions under several simplifying assumptions. In addition, several other researchers characterized the cascade time delays in the context of gamma-ray bursts (Ichiki et al., 2008; Murase et al., 2008).

Lower limits on the cascade flux due to gamma ray observations have lately begun to appear in the literature. Combined with the upper limits from Figure 1.1, these lower limits can be construed, with caveats, as a positive detection of the EGMF. Neronov & Vovk (2010) studied observations of the spectra from three extragalactic sources to derive these lower limits, and other authors have employed similar methods (Tavecchio et al., 2010b; Taylor et al., 2011; Huan et al., 2011). Dermer et al. (2011) pointed out that the period of activity of the sources should be taken into account in setting these limits, and Essey et al. (2011) considered the modification of the limits in the case that the gamma-ray sources are also sources of cosmic-ray nuclei. A claim of a positive detection of the EGMF by Ando & Kusenko (2010), however, turned out more likely to be an instrumental artifact (Neronov et al., 2011).

In this work, I aim to explore this new technique to access the properties of the EGMF. Specifically, I build upon previous research, which used only the spectral information available from models of the cascade to constrain the EGMF, by searching for the extended halo of secondary gamma rays expected around otherwise pointlike sources of gamma rays. Chapter 2 describes the background photon populations that initiate and sustain the cascades and summarizes the aspects of pair production and inverse Compton scattering that are relevant to the development of electromagnetic cascades in extragalactic space. A brief review of the sources and detectors used in this new method appears in Chapter 3, followed in Chapter 4 by a description of a semi-analytic model that presents a conceptually clear but statistically powerful method to characterize the spectra of the cascades. Chapters 5 and 6 are respectively dedicated to the description of a detailed Monte Carlo simulation of the cascade and the application of that simulation to search for the energy-dependent morphological imprint of the EGMF on the cascades. I conclude in Chapter 7 with a discussion of the relevance of a strong EGMF and opportunities for future work.

CHAPTER 2

EXTRAGALACTIC BACKGROUNDS AND INTERACTIONS

Electromagnetic cascades developing in extragalactic space suffer three primary interactions: pair production of gamma rays on the isotropic photon backgrounds, inverse Compton scattering of background photons by high-energy electrons and positrons, and Lorentz force interactions between the charged leptons and the EGMF. The development of an understanding of the characteristics of the cascade is critical for extracting information on the EGMF from gamma-ray observations. In this chapter, I summarize the relevant isotropic photon backgrounds and fundamental physics interactions that initiate and sustain the extragalactic electromagnetic cascades.

2.1 Isotropic Backgrounds

The dominant photon backgrounds influencing the cascade are the cosmic microwave background (CMB) and the extragalactic background light (EBL). As the remnant radiation from the early universe at the time of decoupling, the CMB is remarkably well measured and follows a nearly perfect blackbody spectrum (Mather et al., 1994). In contrast, attempts to measure the EBL are complicated by the presence of strong foreground contributions from the Galaxy and from zodiacal light due to dust in the solar system (Mazin & Raue, 2007).

Figure 2.1 summarizes recent measurements of the EBL based on the work of a variety of researchers. The high-energy peak of the EBL arises due to the integrated optical emission from galaxies throughout the star-forming history of the universe, while absorption and thermal re-radiation of that optical emission by dust generates the peak at lower energies (Mazin & Raue, 2007). In general, direct measurements of dark sky regions can be contaminated by the foreground emission and should be interpreted conservatively as upper limits on the EBL density. Similarly, measurements of galaxy counts must extrapolate those counts below the confusion limit and should therefore be considered conservatively as lower limits. As indicated in Figure 2.1, at some energies the range of allowed values for the EBL energy density can vary by nearly an order of magnitude between these lower and upper limits. In order to draw conservative conclusions based on the cascade flux generated from electromagnetic interactions with the EBL, I adopt the EBL model of Franceschini et al.

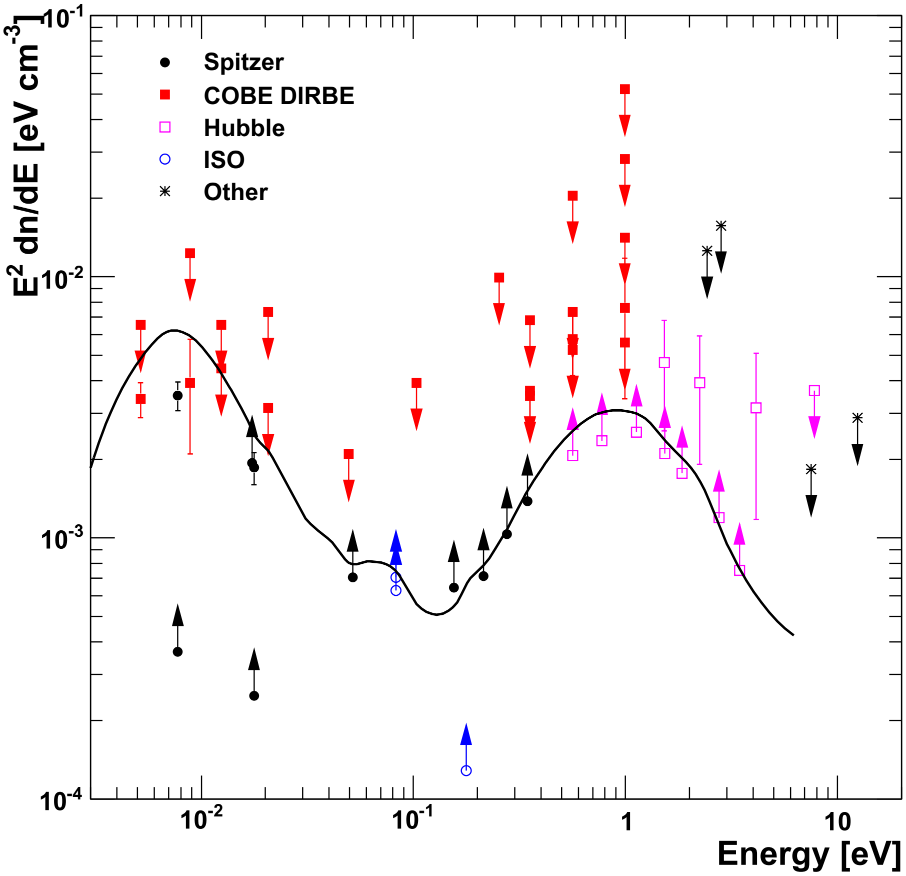

Figure 2.1: Measurements and constraints on the EBL at $z = 0$, adapted from Mazin & Raue (2007), along with the $z = 0$ EBL model from Franceschini et al. (2008). The data points are colored according to the instrument used to derive them.

(2008), which is shown in Figure 2.1 to follow the EBL lower limits reasonably well. The results from this model are conservative because the total amount of cascade emission, which carries the signal of the EGMF, is smaller than for a model with a higher density of EBL photons. Still lower models, such as that of Gilmore et al. (2009) exist, and Vovk et al. (2012) have shown that such models likely affect conclusions about the EGMF by a factor of at most a few.

When redshift due to the expansion of space is accounted for, the CMB energy density ρ_{CMB} evolves as a radiation energy density:

$$\rho_{\text{CMB}}(z) = (1+z)^4 \rho_{\text{CMB}}(0). \tag{2.1}$$

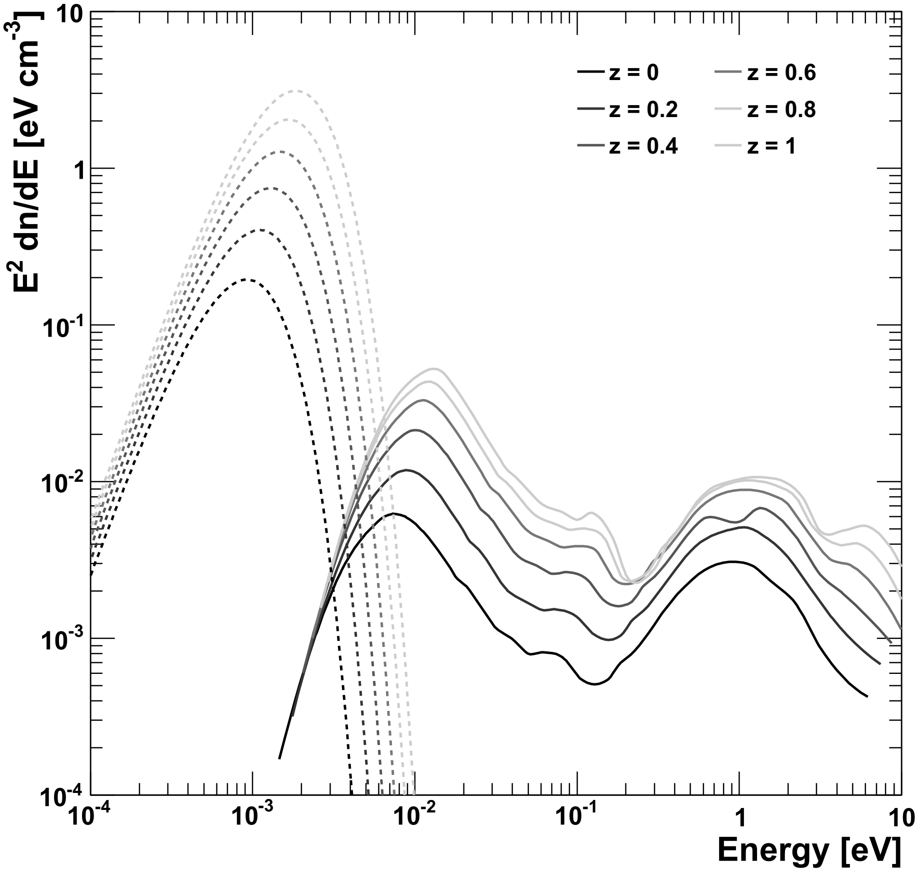

Figure 2.2: Recent history of the CMB and EBL from the model of Franceschini et al. (2008).

Because the EBL incorporates emission generated throughout the history of the universe, however, its evolution is more complicated since source terms must be accounted for. The recent history, out to $z = 1$, of both the CMB and the EBL from Franceschini et al. (2008) appears in Figure 2.2, in which the deviation of the EBL's evolution from the simple scaling of Equation 2.1 is evident.

Figure 2.2 shows only a restricted portion of the background photon spectrum. At lower energies, one expects to find an isotropic population of radio photons, while at higher energies an isotropic x-ray background appears. Due to its low number density compared to the CMB and even the EBL, the x-ray background is largely irrelevant to cascades initiated by gamma rays at the TeV scale (Gould & Schréder, 1967). The energies of photons in the radio background are generally far too low to provide pair production targets for gamma rays with energies below 10^5 TeV, and their influence on the energies and trajectories of the electrons and positrons in the cascades will be negligible for the same reason.

2.2 Pair Production

In the absence of pair production interactions, gamma rays from extragalactic sources would travel directly to Earth without attenuation, and while the benefit to gamma-ray observations of extragalactic objects would be undeniable, the influence of the EGMF on the cascades would be impossible to measure because there would be no cascades. This section summarizes the pair production interaction in the context of the development of the extragalactic cascades.

2.2.1 Kinematics

Diagrams depicting the relevant kinematics for the pair production interaction appear in Figure 2.3, with the situation in the lab frame prior to interaction being shown in the upper left. It is convenient to introduce the variable q, given by

$$\frac{1}{q} = \frac{1}{2}\frac{E\epsilon}{m^2c^4}(1-\cos\theta), \tag{2.2}$$

where E and ϵ are the energies of the primary gamma ray and target photon, respectively, and θ is the angle between their trajectories, as shown in Figure 2.3(a). Since q is related to the Mandelstam s via $q = 4m^2c^4/s$, the threshold condition for pair production $\sqrt{s} \geq 2mc^2$ can be expressed as $q \leq 1$. As q is positive by construction, its range of validity is therefore $m^2c^4/E\epsilon \leq q \leq 1$. This range makes it clear that it is possible to find combinations of E and ϵ for which pair production does not occur, namely $\sqrt{E\epsilon} \leq mc^2$.

Following a boost $\vec{\beta}$ to the center of momentum frame, the collision becomes head-on, as shown in Figure 2.3(b), with both photon energies given by E'. According to Protheroe (1986), the appropriate boost speed is

$$\beta = \frac{E\cos\phi + \epsilon\cos(\theta-\phi)}{E+\epsilon}, \tag{2.3}$$

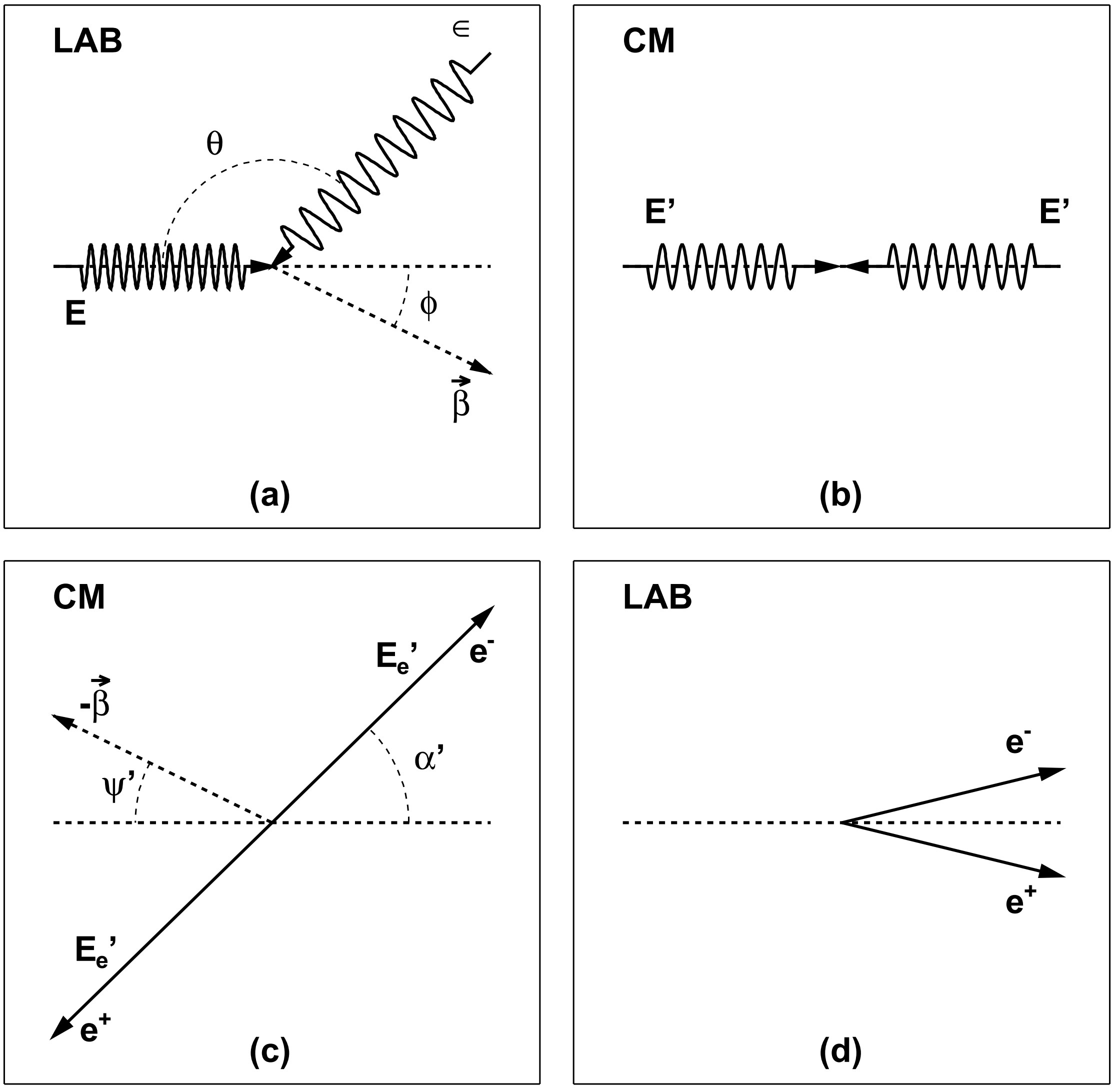

Figure 2.3: Kinematics of the pair production interaction. (a) Photons in the lab frame prior to interaction, with boost vector $\vec{\beta}$ to the center of momentum frame indicated. (b) After a boost into the center of momentum frame but still prior to interaction. (c) Electron and positron produced in the center of momentum frame, with boost vector -$\vec{\beta}$ back to the lab frame indicated. (d) The boost back to the lab frame results in the leptons propagating at small angles relative to the initial direction of the gamma ray.

with the boost angle ϕ relative to the primary gamma ray's direction specified by

$$\tan\phi = \frac{\epsilon\sin\theta}{E + \epsilon\cos\theta}. \tag{2.4}$$

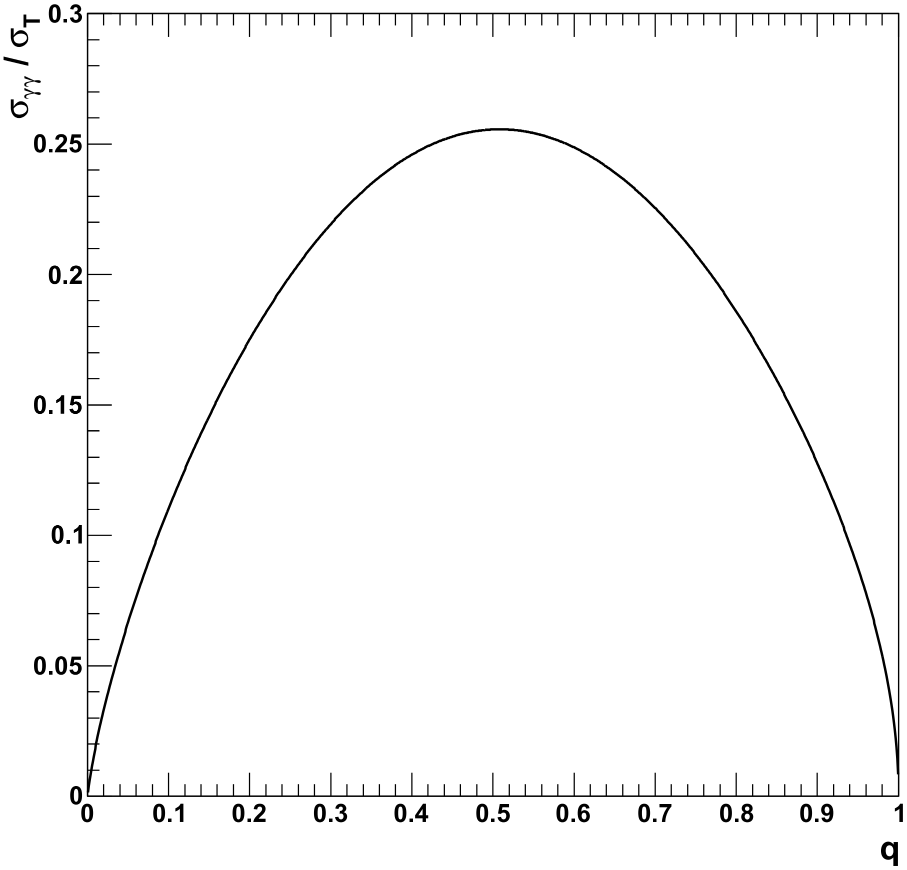

Figure 2.4: Total cross section for pair production as a function of q.

The appropriate boost factor for a head-on collision ($\cos\theta = -1$) in the lab frame between a high-energy gamma ray and a low-energy background photon ($E \gg \epsilon$) is therefore

$$\beta = \frac{E - \epsilon}{E + \epsilon} \approx 1 - 2\frac{\epsilon}{E}. \tag{2.5}$$

This corresponds to a Lorentz factor of $\gamma \approx \sqrt{E/4\epsilon}$. In general, via straightforward boost mechanics, the angle ψ' is given by

$$\tan\psi' = \frac{(E + \epsilon)\sin\theta}{\gamma(E - \epsilon)(1 - \cos\theta)}, \tag{2.6}$$

and this permits a return to the lab frame following the computation of the kinematics in the center of momentum frame.

Working in the center of momentum frame, Jauch & Rohrlich (1976) find that the spin-independent differential cross section for pair production is

$$\frac{d\sigma_{\gamma\gamma}}{dx_{\alpha'}} = \frac{3}{8}\sigma_T \frac{q\sqrt{1-q}}{2} \frac{1-(1-q)^2 x_{\alpha'}^4 + 2q(1-q)(1-x_{\alpha'}^2)}{\left[q-(1-q)x_{\alpha'}^2\right]^2}, \tag{2.7}$$

where $\sigma_T \approx 6.65 \times 10^{-25}$ cm^2 is the Thomson cross section and $x_{\alpha'} = -\cos\alpha'$, with α' the angle between the outgoing electron and the direction of the primary gamma ray, as shown in Figure 2.3(c). The total cross section for pair production can be found by integrating Equation 2.7 over $x_{\alpha'}$ to obtain

$$\sigma_{\gamma\gamma}(q) = \frac{3}{8}\sigma_T q \left[\left(1+q-\frac{1}{2}q^2\right)\ln\left(\frac{1+\sqrt{1-q}}{1-\sqrt{1-q}}\right) - (1+q)\sqrt{1-q}\right], \tag{2.8}$$

which is plotted in Figure 2.4. The function $\sigma_{\gamma\gamma}(q)$ has a peak at $q \approx 0.508$, which can be interpreted via Equation 2.2 either as a preferred target energy ϵ given the collision angle θ or a preferred collision angle given the target energy. For a head-on collision, the preferred target energy for a primary photon with energy E_{TeV} TeV is given by

$$\epsilon_{\mathrm{eV}} \approx \frac{1}{2E_{\mathrm{TeV}}}, \tag{2.9}$$

where ϵ_{eV} is the background photon energy in eV.

2.2.2 *Product Angles and Energies*

In the center of momentum frame, the electron and positron are each produced with energy $\sqrt{s}/2$ due to conservation of momentum. This translates to a speed of

$$c\beta_e' = c\sqrt{1-q}. \tag{2.10}$$

At the most likely value $q \approx 0.508$, $\beta_e' \approx 0.7$. Under the assumption of a primary gamma ray with very high energy interacting via head-on collision with a low-energy background photon, the approximation from Equation 2.5 can be used to compute the angle α that the electron's lab frame trajectory makes with respect to the direction of the primary gamma

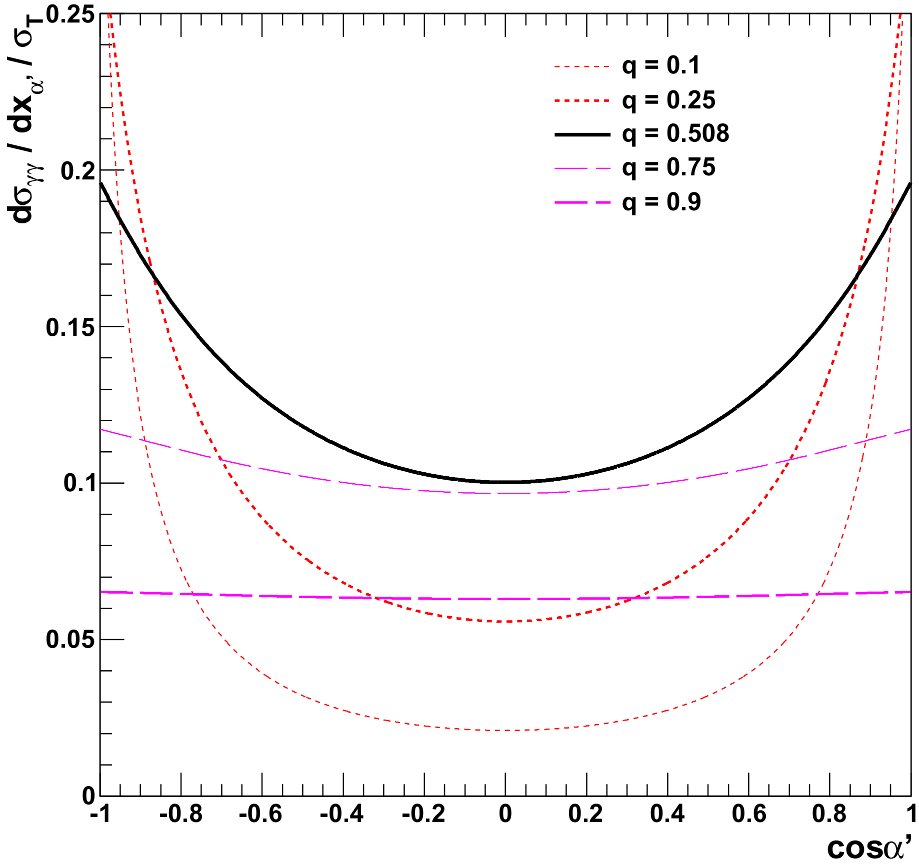

Figure 2.5: Pair production differential cross section, for select values of q, as a function of the electron emission angle in the center of momentum frame.

ray. A simple application of the Lorentz transformation yields

$$\tan\alpha \approx 2\sqrt{\frac{\epsilon}{E}}\frac{\beta'_e \sin\alpha'}{\beta'_e \cos\alpha' - 1}. \tag{2.11}$$

The angle α is thus suppressed by the factor $\sqrt{\epsilon/E}$, which is small, in the range of 10^{-6} according to Equation 2.9. This order-of-magnitude calculation suggests that the products of pair production interactions in the extragalactic cascade are generally collimated in the direction of the primary gamma ray, provided that background photons exist in sufficient numbers at the favored target energy.

Under the same approximation, the energy of the electron in the lab frame appears as

$$E_e = E_e'\gamma(1-\beta\beta_e'\cos\alpha') \approx \frac{1}{2}\sqrt{\frac{E}{\epsilon}}\frac{\sqrt{s}}{2}(1-\beta_e'\cos\alpha') = \frac{1}{2}E(1-\beta_e'\cos\alpha'). \qquad (2.12)$$

The specific value of the energy depends on β_e' (and thereby q through Equation 2.10), and the distribution of $\cos\alpha'$, which can be obtained from the differential cross section specified by Equation 2.7. Figure 2.5 shows the distribution of $\cos\alpha'$ for several values of q. Small values of q tend to favor extreme values for $\cos\alpha'$, while large values tend toward a flatter distribution. For modest values of β_e' and small values of $\cos\alpha'$, both of which are attained at large values of q, Equation 2.12 indicates that the primary gamma ray's energy is split evenly between the product electron and positron to a good approximation. As q decreases, β_e' approaches 1 while $\cos\alpha'$ approaches ±1, indicating that one of the leptons receives most of the energy of the primary gamma ray, while the other lepton becomes far less energetic. At the most likely value $q \approx 0.508$, $|\cos\alpha'|$ attains an average value of approximately 0.56, and the more energetic lepton receives approximately 0.7 of the primary gamma ray's energy. For comparison, at $q = 0.9$ the more energetic lepton has only 0.58 of the primary gamma ray's energy, and at $q = 0.1$ the fraction is 0.84.

While the calculations performed in this section apply strictly only to head-on collisions, they can be straightforwardly generalized to cases where $\cos\theta \neq -1$ via an appropriate adjustment of either E or ϵ given a value for q. In this sense, they should capture the essence of the physics at the order-of-magnitude level of accuracy. In general, the Monte Carlo simulation described in Chapter 5 employs the full distributions instead of the approximations made in this section.

2.3 Inverse Compton Scattering

The second part of the cascade involves the inverse Compton scattering process, which is the same as the Compton scattering process in the limit of large the electron energy in the lab frame.

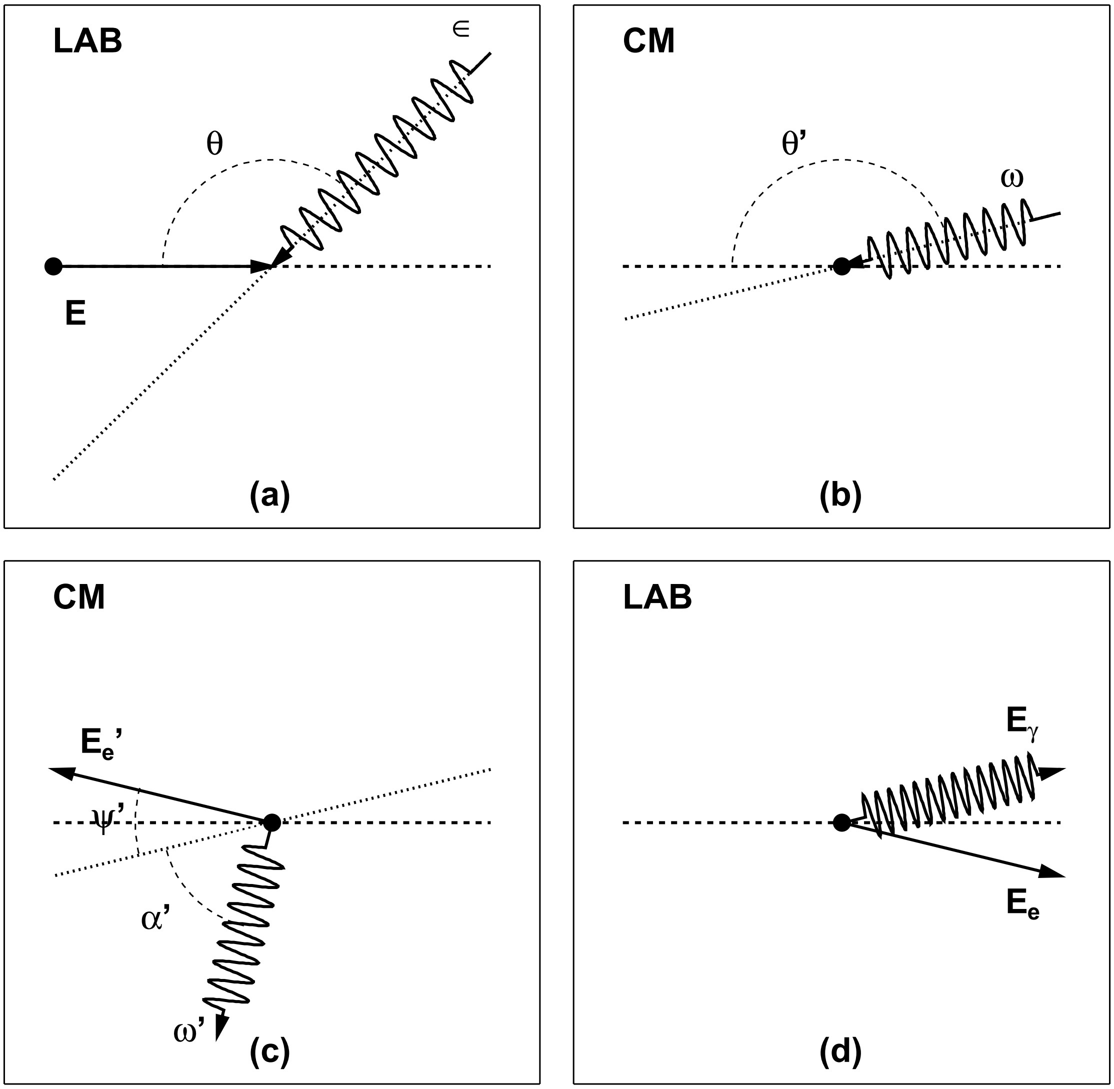

Figure 2.6: Kinematics of the inverse Compton scattering interaction. (a) An energetic electron in the lab frame interacts with a background photon. (b) After a boost into the center of mass frame, the electron is at rest with the photon incident prior to interaction. (c) Following interaction, the electron and photon scatter. (d) Similar to pair production, a boost back to the lab frame results in the collimation of the particles along the electron's initial trajectory.

2.3.1 Kinematics

The kinematics of inverse Compton scattering differs significantly from that of pair production. Figure 2.6 illustrates the relevant aspects of the process. It is convenient to introduce the variable x, given by

$$x = 2\frac{E\epsilon}{m^2c^4}(1 - \beta\cos\theta), \tag{2.13}$$

where E and ϵ are respectively the electron energy and photon energy in the lab frame, θ is the angle between the particles as indicated in Figure 2.6(a), and βc is the speed of the electron in the lab frame before the interaction. Compton scattering is well studied in the center of mass frame in which the electron is at rest, so the natural choice is to boost at speed βc along the electron's lab-frame trajectory. Following this boost, the background photon has energy ω[1], measured in terms of the electron mass mc^2, as shown in Figure 2.6(b). The interaction imparts some energy to the electron, after which the photon's new energy is ω' (Figure 2.6(c)). The angle α' specifies the angle of deflection of the background photon with respect to its initial trajectory in the center of mass frame. As with pair production, when the boost back to the lab frame is performed, the particles become collimated along the initial trajectory of the electron. This is depicted in Figure 2.6(d).

In contrast to the pair production interaction, inverse Compton scattering does not involve the creation of any new mass, so there is no threshold value for x as there was for q in the previous section. The differential cross section is straightforward to compute (see Jauch & Rohrlich (1976) or Peskin & Schroeder (1995) for details) and is given by

$$\frac{d\sigma_{e\gamma}}{dx_{\alpha'}} = \frac{3}{8}\sigma_T \left(\frac{\omega'}{\omega}\right)^2 \left[\frac{\omega'}{\omega} + \frac{\omega}{\omega'} - 1 + x_{\alpha'}^2\right], \tag{2.14}$$

where $x_{\alpha'} = -\cos\alpha'$ again, and the relation between ω and ω' is given by the famous formula for the change in wavelength of the Compton scattered photon:

$$\frac{\omega}{\omega'} = 1 + \omega(1 + x_{\alpha'}). \tag{2.15}$$

Integration of Equation 2.14 produces the total cross section for inverse Compton scattering,

$$\sigma_{e\gamma}(x) = \frac{3}{8}\sigma_T \frac{16x + 32x^2 + 18x^3 + x^4 - (16 + 40x + 30x^2 + 4x^3 - 2x^4)\ln(1+x)}{x^3(1+x)^2}, \tag{2.16}$$

which appears in Figure 2.7. For small values of x, the cross section approaches the Thomson

---

[1] It is straightforward to see that $x = 2\omega$.

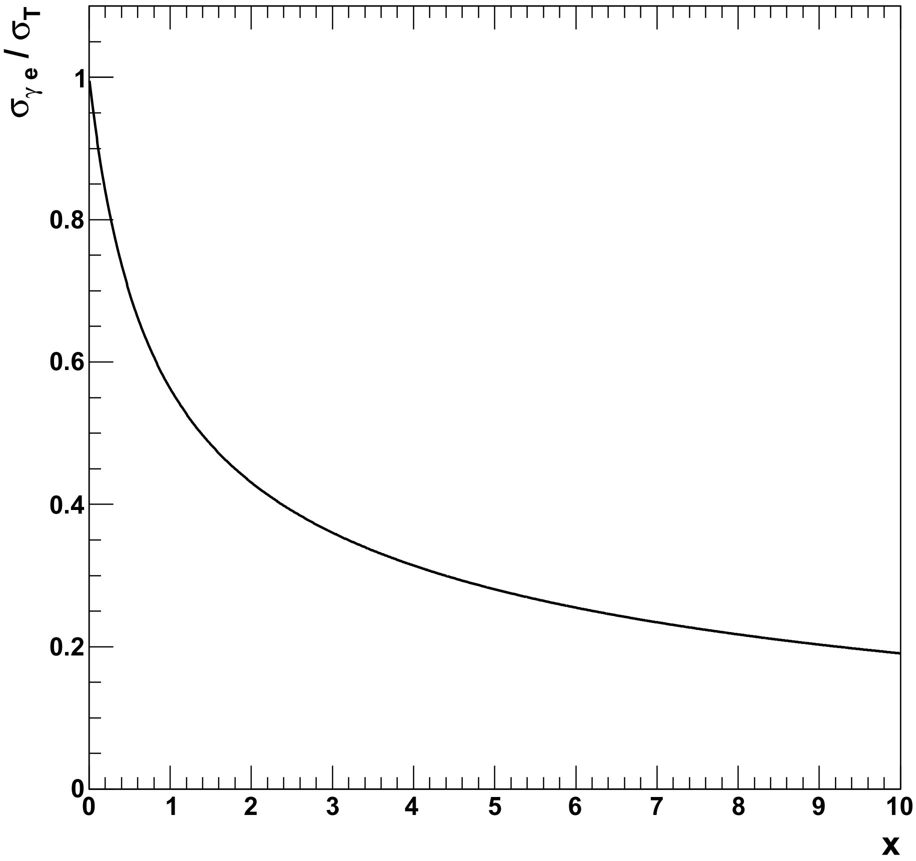

Figure 2.7: Total cross section for inverse Compton scattering.

cross section σ_T.

Figure 2.7 demonstrates that small values of x are favored in inverse Compton scattering. According to Equation 2.13, this translates to background photons with lower energies and, somewhat counterintuitively, trajectories in line with the electron's own trajectory. However, due to the inclusion of a factor proportional to the relative speed between the photon and electron when we compute the interaction rate, these photons will only be important in the scattering if the energy of the background photon becomes comparable to the energy of the electron and they can generally be disregarded (Blumenthal & Gould, 1970). The differential cross section from Equation 2.14 appears in Figure 2.8, which highlights the increased cross section for small values of ω (and therefore small values of x). As the target photon energy is increased, not only does the cross section decrease, but the distribution of the angle α' through which the photon is deflected away from its initial trajectory becomes strongly

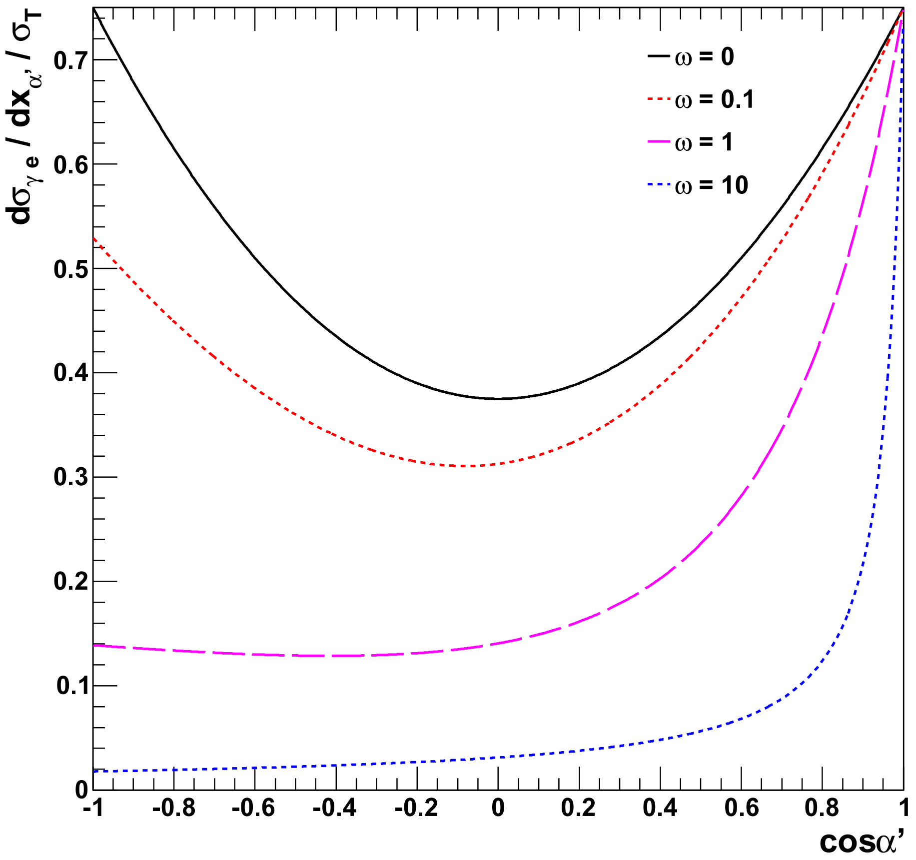

Figure 2.8: Differential cross section for inverse Compton scattering interactions at select values of ω.

peaked at $\alpha' = 0$.

2.3.2 Product Angles and Energies

From simple boost mechanics, the target photon energy in the center of mass frame is given by

$$\omega = \gamma\epsilon(1 - \beta\cos\theta), \tag{2.17}$$

with $\gamma = E/mc^2$ the Lorentz factor of the electron. For a head-on collision in the lab frame, $\theta = \pi$, which enforces $\theta' = \pi$, and the lab-frame energy of the photon after the interaction is

$$E_\gamma = \gamma^2\epsilon\frac{(1 + \beta\cos\alpha')(1 + \beta)}{1 + \gamma\frac{\epsilon}{mc^2}(1 + \beta)} \approx 4\gamma^2\epsilon, \tag{2.18}$$

where the approximation is valid in the limit of small scattering angles $\cos\alpha' \approx 1$ and subject to the Thomson limit $\sqrt{E\epsilon} \ll mc^2$. Equation 2.18 is a general upper bound on the produced gamma ray's energy in all regimes. A full treatment of all the incident angles for an isotropic distribution of background photons amends this approximation in the Thomson limit to (Blumenthal & Gould, 1970)

$$E_\gamma \approx \frac{4}{3}\gamma^2\epsilon. \tag{2.19}$$

Equation 2.19 inspires an approximation to the rate of change of the electron's energy as the product of the energy loss per interaction and the interaction rate for a highly relativistic electron, $c\sigma_T n_{\rm CMB}$,

$$mc^2\frac{d\gamma_e}{dt} \approx -\frac{4}{3}\gamma_e^2\epsilon_0 c\sigma_T n_{\rm CMB}, \tag{2.20}$$

where ϵ_0 is the energy of the peak of the CMB. In the Thomson limit, even though the increase in the photon's energy is enormous (by a factor of γ^2 from the relativistic electron), the fractional loss of energy of the electron is of order $E\epsilon/m^2c^4$ and therefore small. This is not the case in the Klein-Nishina regime, when the electron loses a substantial amount of its energy to the photon and the approximation of Equation 2.18 is no longer valid.

Equation 2.19 ensures that the secondary photons appear at gamma-ray energies. For example, an electron with energy 1 TeV (presumably generated by a pair production event from a primary gamma ray with energy 2 TeV) has a Lorentz factor of $\gamma \approx 2 \times 10^6$. Its interaction with the peak of the CMB at energy 0.6 meV produces a secondary gamma ray with approximate energy 3 GeV by Equation 2.19.

As with pair production, the inverse Compton scattered products are highly collimated along the initial electron trajectory. From simple boost mechanics, the final lab-frame angle θ_γ that the product gamma ray makes with the electron trajectory is given without approximation by

$$\cos\theta_\gamma = \frac{\beta + \cos(\theta' - \alpha')}{1 + \beta\cos(\theta' - \alpha')}. \tag{2.21}$$

For a head-on collision at high energy, the angle is suppressed by a factor of $1/\gamma$,

$$\theta_\gamma \approx \frac{1}{\gamma}\sqrt{\frac{\cos\alpha'}{1-\cos\alpha'}}, \tag{2.22}$$

provided that α' is not especially small.

2.4 The Mean Free Path for Interactions

The kinematics of both the pair production and inverse Compton processes determines the energy distributions of gamma rays in the extragalactic cascades. Naturally, the interaction lengths of these processes influence the cascade geometry. In this section, I consider the mean free paths of the two processes separately and then discuss their role in the cascade.

2.4.1 Pair Production

For an arbitrary density of isotropic background photons, $n_\epsilon(\epsilon)$, specified in units of photons per energy per volume, the mean free path for pair production $\lambda_{\gamma\gamma}$ appears as (Protheroe, 1986)

$$\frac{1}{\lambda_{\gamma\gamma}} = \int_0^\infty d\epsilon \frac{2n_\epsilon(\epsilon)m^4c^8}{E^2\epsilon^2} \int_{q_{\rm min}}^1 dq \frac{\sigma_{\gamma\gamma}(q)}{q^3} \equiv \int_0^\infty d\epsilon Q_{\gamma\gamma}(\epsilon). \tag{2.23}$$

The threshold value $q_{\rm min} = m^2c^4/E\epsilon$. Equation 2.23 is accurate for small redshifts but can be straightforwardly generalized to cases where $z \neq 0$. The integrand $Q_{\gamma\gamma}(\epsilon)$ is large for background energies ϵ that are likely to initiate a pair production interaction, so it may be crudely interpreted as the odds for a primary gamma ray with energy E to interact with a background photon of energy ϵ, given the isotropic density $n_\epsilon(\epsilon)$.

Figure 2.9 shows $Q_{\gamma\gamma}(\epsilon)$ as a function of background energy for several values of E. From the figure, it is evident due to the pair production threshold condition that primary gamma rays with energies under 100 TeV interact almost exclusively with the EBL. As the energy of the primary gamma ray decreases, the pair production threshold dictates that the interaction must occur with background photons of increasingly higher energy, so that primary gamma rays at 1 TeV interact primarily with the high-energy optical peak of the EBL. Additionally, it is apparent from the figure that the interaction length decreases with primary gamma-ray energy, at least in the range from 100 GeV to 100 TeV. The reason for this decrease is apparent in Figure 2.2. The energy densities in the infrared and optical peaks of the EBL are approximately the same, but the energy of an average photon in the two peaks differs by two orders of magnitude. Consequently, the preferred targets for 100-TeV primaries are about 100 times more numerous than those for 1-TeV primaries, and the mean free path is

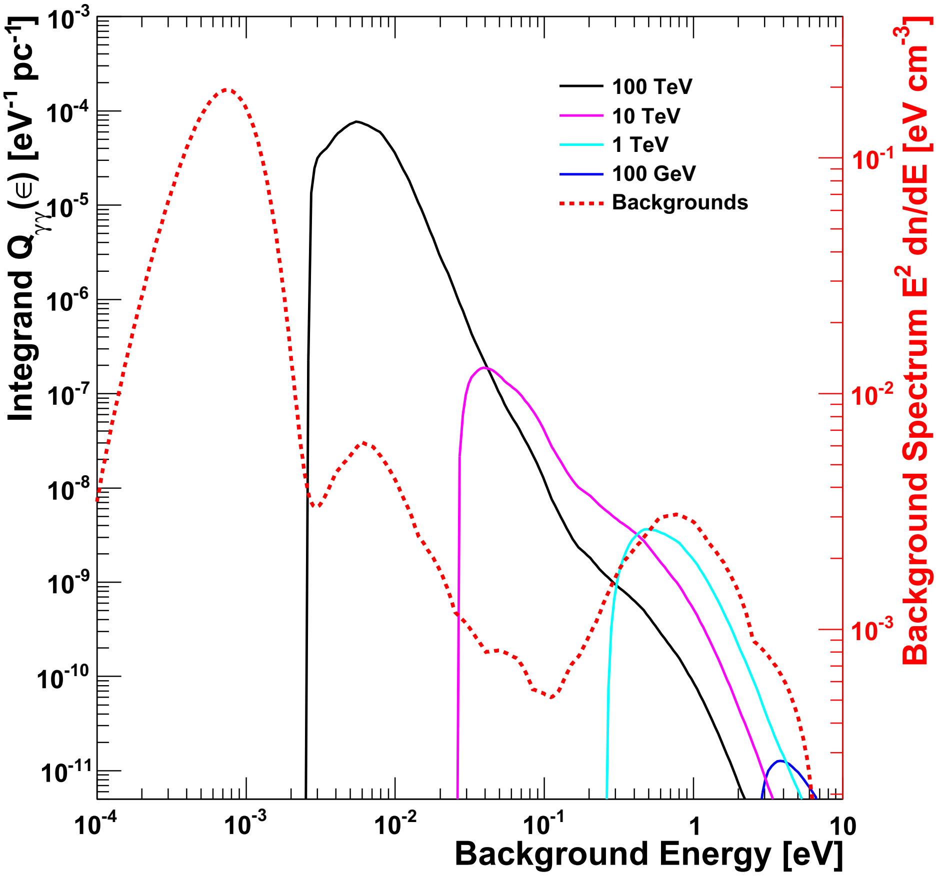

Figure 2.9: The integrand of Equation 2.23 as a function of background energy, along with the isotropic background photon distribution.

therefore about 100 times shorter.

2.4.2 Inverse Compton Scattering

Again referring to Protheroe (1986), I find the mean free path for inverse Compton scattering $\lambda_{e\gamma}$ to be

$$\frac{1}{\lambda_{e\gamma}} = \int_0^\infty d\epsilon \frac{n_\epsilon(\epsilon) m^4 c^8}{8\beta E^2 \epsilon^2} \int_{x_-}^{x_+} dx x \sigma_{e\gamma}(x) \equiv \int_0^\infty d\epsilon Q_{e\gamma}(\epsilon), \tag{2.24}$$

where the limits $x_\pm = 2E\epsilon(1 \pm \beta)/m^2c^4$ arise from setting $\cos\theta = \pm 1$ in Equation 2.13. Figure 2.10 plots the integrand $Q_{e\gamma}(\epsilon)$, again with the background energy densities. It is obvious from the figure that inverse Compton scattering proceeds primarily via interactions with the CMB, although some interactions with the infrared peak of the EBL may occur. The

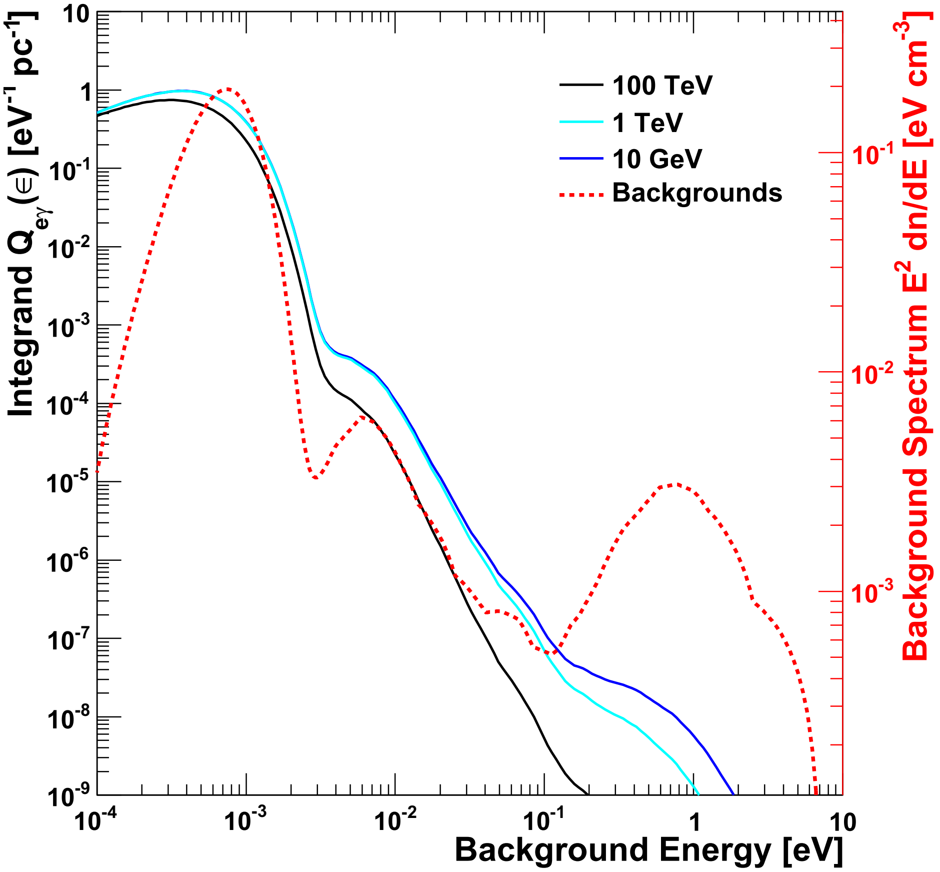

Figure 2.10: The integrand of Equation 2.24 as a function of background energy.

curves in Figure 2.10 more closely follow the background densities than those of Figure 2.9 due to the absence of a preferred interaction energy for this process. They are also remarkably similar over a very wide electron energy range from 10 GeV to 100 TeV, at which point the cross section of Equation 2.16 begins to diverge from the Thomson limit. Although interactions with the EBL occur far less frequently than with the CMB, the background energies, and consequently the product photon energies, are much higher and a single EBL interaction can be important to the development of the cascade. For example, for a 20-TeV electron, the transition to the Klein-Nishina regime occurs at a background photon energy of about 10 meV, well above the CMB but well within the infrared peak of the EBL.

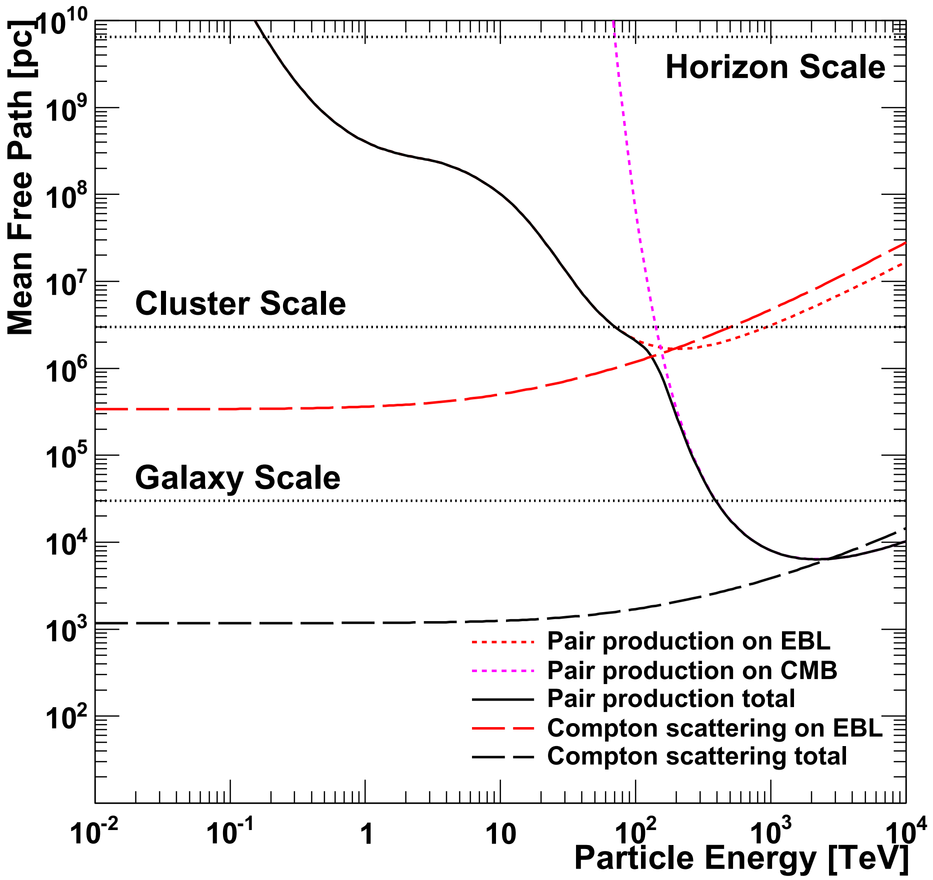

Figure 2.11: The mean free path λ as a function of primary energy for pair production and inverse Compton scattering. Average size scales for galaxies, clusters, and the universe horizon are also indicated.

2.4.3 Influence of the Cascades

Figure 2.11 plots the mean free path as a function of primary particle energy for both the pair production and inverse Compton scattering processes. As shown in the figure, primary gamma rays below about 200 GeV will stream freely through the universe with an interaction length greater than a Hubble radius. Above 100 TeV, the primary gamma rays will interact on cluster-scale distances, where the local cluster magnetic fields are strong and any pairs produced are quickly isotropized. Primary gamma rays between 200 GeV and 100 TeV will produce an extragalactic cascade of electrons that interact with the CMB on kpc-scale distances. Since the energy loss of the electrons is proportional to the square of their energy via Equation 2.20, however, the number of these interactions increases as the energy decreases, and the electrons may propagate much farther than 1 kpc.

The role of the extragalactic cascades is thus to convert gamma rays at the TeV-scale and above into gamma rays at the GeV scale, which can freely propagate throughout the universe. Depending on the distance between the source and the observer, secondary gamma rays with energies significantly in excess of 200 GeV can interact again and the cascade can go through multiple generations of particles. The deflections of the electrons and positrons over their trajectories create time delays, or "echos," and extended emission, or "halos," of secondary, cascaded gamma rays around otherwise pointlike sources. The spectral and spatial properties of these echos and halos can be used to extract information about the EGMF, which acts via the Lorentz force on the electrons and positrons in the cascade.

2.4.4 Redshift Generalizations

Chapter 5, which describes the development of a Monte Carlo simulation for characterizing the cascade, relies on the generalization Equations 2.23 and 2.24 to account for redshift. These generalizations appear as

$$\frac{1}{\lambda_{\gamma\gamma}} = \int_0^\infty d\epsilon_0 \frac{2c(1+z_i)^2 m^4 c^8}{H_0 E_i^2 \epsilon_0^2} \int_{z_f}^{z_i} dz \frac{n_\epsilon\left[(1+z)\epsilon_0; z\right]}{(1+z)^4 Q(z)} \int_{q_{\min}(z)}^{1} dq \frac{\sigma_{\gamma\gamma}(q)}{q^3}, \tag{2.25}$$

for pair production and

$$\frac{1}{\lambda_{e\gamma}} = \int_0^\infty d\epsilon_0 \frac{m^4 c^9}{8 H_0 \epsilon_0^2} \int_{z_f}^{z_i} dz \frac{n_\epsilon\left[(1+z)\epsilon_0; z\right]}{\beta(z)\left[E(z)\right]^2 (1+z)^2 Q(z)} \int_{x_-(z)}^{x_+(z)} dx x \sigma_{e\gamma}(x), \tag{2.26}$$

for inverse Compton scattering. In Equation 2.25, E_i is the energy of the gamma ray at its initial redshift z_i, z_f is the final redshift, ϵ_0 is the present-day energy of the background photon, $q_{\min}(z)$ generalizes to

$$q_{\min}(z) = \frac{(1+z_i) m^2 c^4}{(1+z)^2 \epsilon_0 E_i}, \tag{2.27}$$

$H_0 \approx 70$ km/s/Mpc is the Hubble parameter, and $Q(z)$ is the cosmological factor

$$Q(z) = \sqrt{(1+z)^4 \Omega_R + (1+z)^3 \Omega_M + \Omega_\Lambda + (1-\Omega_C)(1+z)^2}, \tag{2.28}$$

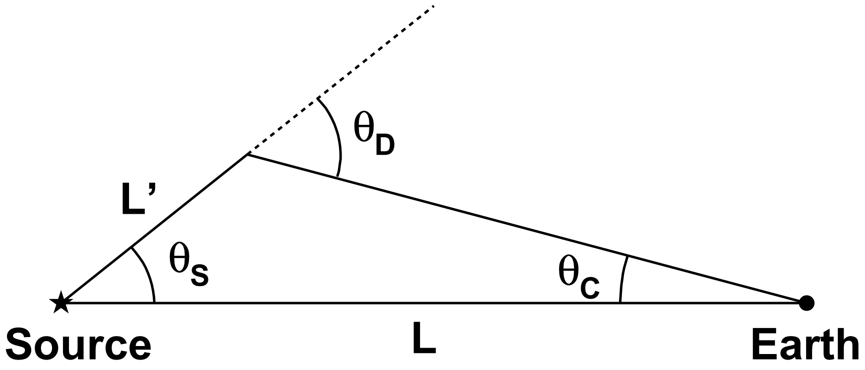

Figure 2.12: Geometry relevant to the extragalactic cascades, following Dermer et al. (2011).

with Ω_R, Ω_M, Ω_Λ, and Ω_C respectively the radiation, matter, cosmological constant, and curvature densities in units of the critical density ρ_C (Kolb & Turner, 1990). We adopt the standard ΛCDM cosmology with $\Omega_R = 0$, $\Omega_M = 0.3$, $\Omega_\Lambda = 0.7$, and $\Omega_C = 1$. In Equation 2.26, the redshift evolution of the electron's energy is given generally by $[E(z)]^2 = [p(z)]^2 \, c^2 - m^2 c^4$, where

$$p(z)c = \frac{1+z}{1+z_i}\sqrt{E_i^2 - m^2c^4}, \tag{2.29}$$

and $\beta(z) = cp(z)/E(z)$. The limits on the x integration are

$$x_{\pm}(z) = 2(1+z)\frac{E(z)\epsilon_0}{m^2c^4}\left[1 \pm \beta(z)\right]. \tag{2.30}$$

2.5 The Lorentz Force

The EGMF influences the cascade electrons and positrons directly through the Lorentz force. A relativistic electron with Lorentz factor γ in a constant magnetic field follows a spiral trajectory with Larmor radius

$$r_L = \frac{mc\sqrt{\gamma^2 - 1}}{eB} = \frac{p_e}{eB}, \tag{2.31}$$

where e is the charge of the positron and B is the component of the field strength perpendicular to the motion of the particle. The momentum of the electron is p_e. As the electron propagates through a distance D along this trajectory, then, its deflection θ_D is

$$\theta_D = \frac{D}{r_L} = \frac{eBD}{mc\sqrt{\gamma^2 - 1}}. \tag{2.32}$$

Equation 2.32 may be used to approximate the size of the cascade halo. The relevant geometry for an extragalactic source at a distance L is shown in Figure 2.12. In the figure, a primary gamma ray is emitted at an angle θ_S relative to the line of sight to the extragalactic source. The primary gamma ray travels a distance L' before interacting. After the electron is deflected through an angle θ_D, the secondary photon is emitted and arrives at the observer with an angle θ_C relative to the source. The angle θ_C is obviously $\theta_C = \theta_D - \theta_S$ and approximates the size of the halo.

For small angles, $L\theta_C \approx L'\theta_D$. According to Figure 2.11, a 1-TeV gamma ray will travel about 400 Mpc before interacting. For a source of 1-TeV gamma rays at a distance of 1000 Mpc, then, $\theta_C \approx 0.4\theta_D$. After interacting, the gamma ray produces an electron with energy of about 500 GeV, corresponding to $\gamma \approx 10^6$. On average, this electron will interact with the peak of the CMB at 0.6 meV, producing secondary photons with energy 800 MeV according to Equation 2.19. 300 such interactions occurring once approximately every kpc will reduce the electron's energy by half, so with $D \approx 300$ kpc, Equation 2.32 gives $\theta_C \approx 0.2^\circ B/(10^{-15}$ Gauss). This very rough estimate suggests that 0.2° is not an unreasonable size to expect for the halo due to the effects of the EGMF.

2.6 Other Processes

Our characterization of the cascades depends on the assumption that inverse Compton scattering and pair production are the dominant energy-loss channels available to the particles. In principle, processes such as bremsstrahlung or synchrotron radiation could have a significant impact on the electron and positron energies. It is the aim of this section to show that these processes are negligible.

Bremsstrahlung radiation is produced by charged-particle interactions with matter. The dominant component of matter in extragalactic space is the warm-hot intergalactic medium (WHIM), which is primarily ionized hydrogen (Cen & Ostriker, 1999; Bykov et al., 2008). According to Blumenthal & Gould (1970), bremsstrahlung radiation can be thought of as inverse Compton scattering by high-energy electrons on the virtual photons of the Coulomb field of the target proton, and in the high-energy limit, electrons and positrons behave the same, so I will treat only electrons in this section. The energy loss rate from propagation through fully ionized hydrogen can be written as

$$\frac{d\gamma_e}{dt} = 16\alpha r_0^2 c n_e \gamma_e \left[\ln(2\gamma_e) - \frac{1}{3}\right], \tag{2.33}$$

where $\alpha \approx 1/137$ is the fine-structure constant, n_e is the electron number density of the WHIM, and r_0 is the classical electron radius ($\sigma_T = 8\pi r_0^2/3$). Blumenthal & Gould (1970) stress that Equation 2.33 does not reflect a continuous loss rate because the dominant energy loss is due to photons that carry a significant fraction of the electron's energy, so it should not be integrated. Instead, we will compare it to the energy loss rate due to inverse Compton scattering on the CMB, given by Equation 2.20, to determine the importance of bremsstrahlung radiation. The Thomson limit is appropriate because the energy loss due to the CMB scales with γ_e^2, faster than Equation 2.33, and Klein-Nishina losses will occur even faster than losses in the Thomson limit. The ratio of the rates is then

$$R_{\text{brem}} \equiv \frac{\left(\frac{d\gamma_e}{dt}\right)_{\text{brem}}}{\left(\frac{d\gamma_e}{dt}\right)_{\text{CMB}}} = \frac{9\alpha m c^2 n_e \left[\ln(2\gamma_e) - \frac{1}{3}\right]}{2\pi \gamma_e \epsilon_0 n_{\text{CMB}}} \tag{2.34}$$

Restricting our interest to electrons that produce gamma rays above 100 MeV, we find a minimum $\gamma_e \approx 3 \times 10^5$ via Equation 2.19 for an average CMB photon energy $\epsilon_0 = 0.6$ meV, and writing $n_e = (1+\delta)n_b$ in terms of the baryon density $n_b \approx 0.045 n_C \approx 2 \times 10^{-7}$ cm^{-3} (Kolb & Turner, 1990), I get

$$R_{\text{brem}} \approx 5 \times 10^{-7}(1+\delta). \tag{2.35}$$

If all of the baryons are in the WHIM, $\delta = 0$ and even in this most optimistic case the bremsstrahlung losses are relevant for fewer than one in every million electrons. In reality, likely $-\delta$ is of order unity and bremsstrahlung losses are even more negligible.

Electrons can also lose energy due to synchrotron radiation. Again following Blumenthal & Gould (1970), we note that that the energy-loss rate for synchrotron radiation is analogous to the loss rate for inverse Compton interactions on the CMB, with the energy density

$n_{\mathrm{CMB}}\epsilon_0$ replaced by the field energy density $B^2/2\mu_0$, where μ_0 is the magnetic permeability of free space. The effects due to the magnetic field are equivalent to the CMB at a field strength B_{CMB} given by

$$B_{\mathrm{CMB}} = \sqrt{2\mu_0\epsilon_0 n_{\mathrm{CMB}}} \approx 1\ \mu\mathrm{Gauss}, \tag{2.36}$$

and the significance of synchrotron losses scales as B^2. Below 10^{-9} Gauss, then, the energy losses from synchrotron radiation are even worse than for bremsstrahlung, so we neglect them as well.

CHAPTER 3
GAMMA-RAY SOURCES AND DETECTION TECHNIQUES

Having discussed the phenomenology of the extragalactic cascades, I now turn briefly to their detection. Three things are necessary to observe the cascade: a gamma-ray detector, an electromagnetic cascade, and an extragalactic source. The source must be of a class that is well understood, it must have a sufficiently large flux of TeV-scale gamma rays to produce the cascade component, and it must be well measured in both the GeV and TeV energy bands. There are not many options. Starburst galaxies are too faint to produce any appreciable cascade flux, and blazars are the only remaining extragalactic candidate source class. Fortunately, select blazars meet all of the necessary conditions.

Gamma-ray observations of blazars are accomplished via two techniques. At lower energies, in the GeV band from 100 MeV to 100 GeV, space-based detectors such as the Large Area Telescope (LAT) on board the *Fermi* Gamma Ray Space Telescope (Atwood et al., 2009), hereafter referred to as *Fermi*, directly detect gamma rays passing through their instrumented volume. Since the spectrum of every gamma-ray source decreases with increasing energy, eventually such techniques become flux-limited. In the TeV band, roughly from 100 GeV to higher than 10 TeV, ground-based detectors image the Cherenkov radiation from charged particles in the air showers produced by the gamma rays' interactions with the atmosphere (Weekes, 1988). Known as Imaging Atmospheric Cherenkov Telescopes (IACTs), these detectors boast much larger effective areas that compensate for the decreasing flux, but only showers initiated by gamma rays with energies of 100 GeV and above are large enough to be imaged.

3.1 Blazars

Blazars are a subclass of active galactic nuclei (AGN). The conventional picture of the AGN system comprises a host galaxy with a supermassive black hole at its center and is described in detail by Urry & Padovani (1995). In the conventional picture, matter falling into the black hole forms an accretion disk from which jets of bulk material moving at relativistic speeds emerge. Electrons in the jets interact with the local magnetic field to produce synchrotron radiation, which is observed in the x-ray band and at lower energies.

The electrons can scatter either ambient photons from the host galaxy, CMB photons, or their own synchrotron emission via inverse Compton scattering. The resulting scattered photons acquire gamma-ray energies. If the bulk motion is characterized by a Lorentz factor Γ with a typical value around 10, a reasonable model for the high-energy emission $f(E, \theta)$ at the source is that of a boosted isotropic distribution with a power-law spectrum:

$$f(E, \theta) \equiv \frac{dF}{dE d\cos\theta} = F_0 (1 - \beta \cos\theta)^{-\alpha-1} E^{-\alpha} e^{-E/E_C}, \tag{3.1}$$

where F is the flux in units of particles per time per area, F_0 is a normalization factor, βc is the speed corresponding to Γ, $\beta = \sqrt{1 - 1/\Gamma^2}$, θ is the emission angle of a photon relative to the direction of the jet, and E_C is an exponential cutoff energy that will be discussed in a moment.

The characteristic opening angle θ_0 for the jet is approximated by $\theta_0 \approx 1/\Gamma$. If the line of sight to the AGN is significantly larger than θ_0, then most of the emission is beamed away from the observer and the AGN is difficult to detect in gamma rays. However, if the line of sight angle is smaller than θ_0, substantial gamma ray emission can be observed. In this case, the AGN is called a blazar because it is important to classify things based on how they appear.

At energies above 1 TeV, the shape of the intrinsic spectrum given by Equation 3.1 cannot be observed directly because it is attenuated by interactions with the EBL, as Figure 2.11 demonstrates. Instead, a “direct” component of gamma rays that survive the propagation process is observed. The degree of attenuation depends on the energy and the distance to the source. Most TeV-detected blazars inhabit a redshift range of $0.05 \lesssim z \lesssim 0.4$[1], corresponding to an approximate distance range (assuming a flat ΛCDM cosmology) of 200 to 1500 Mpc. For the nearer blazars, gamma rays above a few TeV will interact in the space between the blazar and Earth, while in the extreme case $z \approx 0.4$, gamma rays with energies above a few hundred GeV will interact as well.

Equation 3.1 includes an exponential cutoff energy E_C, which fulfills two purposes. First, when EBL attenuation is accounted for through a deabsorption process, many blazars are found to have an intrinsic TeV spectral index harder than 2, so there must be some term that cuts off the spectrum to avoid an infinite energy catastrophe. The second purpose is

---

[1] See for example http://tevcat.uchicago.edu.

that, according to Figure 2.11, gamma rays with energies around 50 TeV and higher are likely to interact within the galaxy cluster local to the host galaxy of the blazar. In that case, the electron-positron pairs sample the μGauss-scale cluster field instead of the EGMF, and they are rapidly isotropized in the field before they undergo significant inverse Compton scattering. At any rate, what little emission that does reach Earth from these pairs will be indistinguishable from intrinsic emission unless the knowledge of the blazar spectrum is perfect. This justifies a maximum cutoff energy of 50 TeV, which I assume throughout the rest of this work, unless otherwise stated. In the absence of other measurements of the blazar, I also assume a modest bulk Lorentz factor of $\Gamma = 10$ and a viewing angle of 0.

The BL Lacertae (BL Lac) objects are the most prominent subclass of blazars detected in the TeV. Initially named for their resemblance to the object BL Lac, these blazars are radio-loud AGN that lack strong emission or absorption features and are generally understood to be Fanaroff-Riley Class I galaxies (Urry & Padovani, 1995). BL Lacs are further classified based on the peak energy of their synchrotron emission into low-frequency-peaked BL Lacs (LBLs), intermediate-frequency-peaked BL Lacs (IBLs), and high-frequency-peaked BL Lacs (HBLs). A given BL Lac object can be classified according to this scheme roughly quantitatively by determining the ratio of its radio flux to its x-ray flux. For IBLs this ratio takes on a value near 0.75, while LBLs lie above this value and HBLs lie below it (Fossati et al., 1998). Of 41 BL Lac objects presently detected at TeV energies, 33 are of the HBL type.

In selecting a blazar for an EGMF study, one should be aware of the environment along its line of sight, which should be dominated by void regions. If instead the line of sight passes along a filament or through many clusters in the LSS, then there will be relatively high cluster and filament fields deflecting the leptons in the cascades and obscuring the signal from the EGMF. Due to the long interaction length of the gamma rays and the short (sub-galactic) interaction length of the pairs, it is not a problem to pass through some clusters because they will affect only a small subset of the pairs (Dolag et al., 2011); it is in the case when little of the line of sight traverses voids that problems arise. Fortunately, since the universe is dominated by voids (Pan et al., 2012), poor choices for the line of sight should be rare.

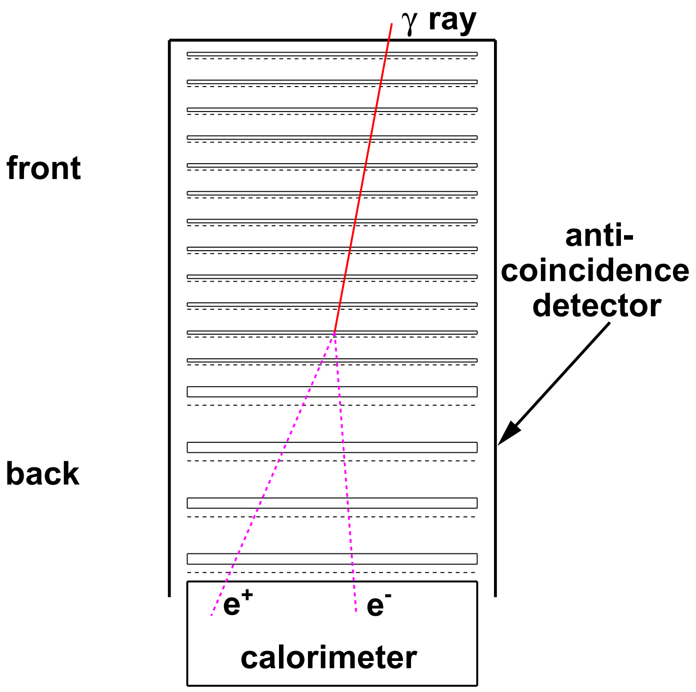

Figure 3.1: Schematic diagram of the principal components of the *Fermi* LAT.

3.2 The *Fermi* Instrument

Blazar gamma rays in the energy range from 100 MeV to 300 GeV, where the signature of the EGMF on the extragalactic cascades is strongest, can be measured by the *Fermi* LAT. The LAT is a pair-conversion telescope operating in survey mode with a field-of-view of 2.4 sr and an acceptance of more than 2.2 m^2 sr for energies above 1 GeV (Atwood et al., 2009). *Fermi* has been in operation since August 2008, so as of this writing more than three and a half years of data have been collected. These data are publicly available as soon as they are taken, and software for analyzing them is provided by the *Fermi* Science Support Center[2]. For the analysis presented in this work, I use version v9r23p1 of the science tools, updated on 1 November 2011, with the instrument response function (IRF) corrections P7SOURCE_V6, which include an updated on-orbit point-spread function (PSF) for the instrument.

Figure 3.1 provides a basic picture of gamma-ray detection in the LAT. Incoming gamma rays convert to electron-positron pairs in the tungsten foil of the converter, after which the electrons and positrons are tracked by means of silicon strip detectors in order to reconstruct

---

[2] http://fermi.gsfc.nasa.gov/ssc/

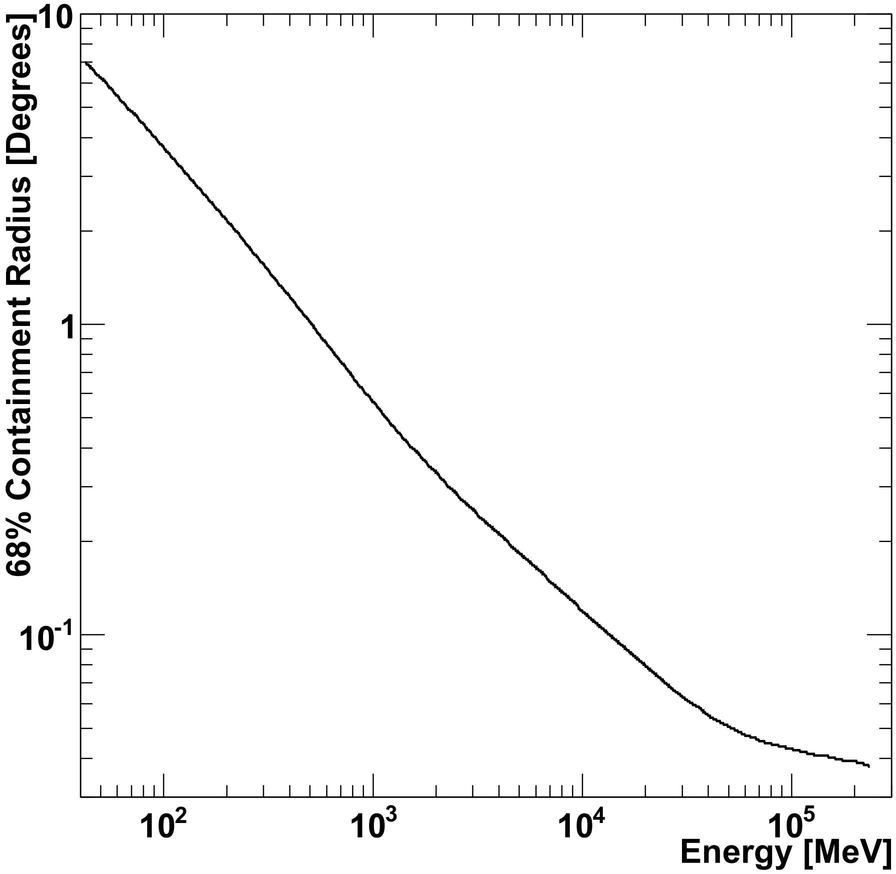

Figure 3.2: *Fermi* LAT point-spread function, adapted from Atwood et al. (2009). The curve is for gamma rays with normal incidence converting in the front part of the detector are included, so the total PSF is somewhat larger.

the gamma ray's direction. After exiting the tracker, the electrons and positrons deposit energy in an electromagnetic cascade in the calorimeter, which is made of CsI crystals and has a depth of 10 radiation lengths (Atwood et al., 2009), from which a measurement of the gamma ray's energy can be inferred. The calorimeter also provides some tracking information, especially for gamma rays at the high-energy end of *Fermi*'s sensitivity. The converter and tracker each exist in two stages, a "front" stage with higher-resolution tracking and a "back stage" with lower-resolution tracking. Gamma rays are roughly equally likely to convert in the front stage as in the back. The entire instrument is surrounded by an anti-coincidence detector that provides excellent rejection of the background cosmic-ray signal.

Section 2.4.3 argued that the EGMF may create cascade halos whose sizes are of order

0.1° or larger. It is therefore important to have sub-degree resolution in the reconstruction of the incoming gamma ray's direction, in order to resolve the features of the halo. The 68% containment radius of the LAT appears in Figure 3.2, demonstrating that this resoultion is attained for energies above several hundred MeV. The energy resolution of the LAT ranges from 8% to 18% over its sensitivity range, achieving the best resolution between 1 and 10 GeV (Atwood et al., 2009). More than 800 *Fermi* sources are associated with blazars, nearly 200 of which are BL Lacertae (BL Lac) objects with a synchrotron component peaking at a high frequency, above 10^{15} Hz (Ackermann et al., 2011). Due to their generally hard spectra and substantial population of synchrotron photons above a few eV, these high-frequency-peaked BL Lacs (HBLs) are prime candidates for EGMF study because the extrapolation of their spectra results in a high TeV-scale flux.

A catalog of existing sources determined via surveys conducted by the *Fermi* team serves as a starting point for additional likelihood analyses (The Fermi-LAT Collaboration, 2011). In addition to numerous point sources, the catalog includes 12 extended sources, as well as an isotropic diffuse component and a detailed map of the Galactic gamma-ray emission. Data analysis in *Fermi* proceeds by proposing a source model and assessing the likelihood of that model compared to the likelihood of its absence. This is accomplished by means of a test statistic T, defined by

$$T = -2\ln\left(\frac{L_0}{L_{\mathrm{GeV}}}\right), \tag{3.2}$$

where L_0 is the likelihood from the null hypothesis of the model without the source and L_{GeV} is the likelihood of the alternative hypothesis, in which a source present. This approach is necessary because of the limited angular resolution of the LAT and the low number of gamma rays collected. As long as the amount of data is sufficiently large, T is distributed in the absence of a source as a $\chi^2(n)$, a χ^2 distribution with n degrees of freedom, where n is the number of parameters characterizing the proposed source.

There are two standard methods for analyzing *Fermi* data, binned and unbinned. In the binned case, events are collected into energy bins, whereas in the unbinned case each event is treated separately. The two methods are expected to be equivalent in the limit of large statistics. Due to the faster processing time, in the rest of this work I use a binned method unless otherwise stated.

3.3 Imaging Atmospheric Cherenkov Telescopes

The measureable flux of a blazar in general follows a power law with a spectral index softer than 1 and is therefore rapidly dropping with increasing energy. Since *Fermi* is a direct detection instrument, it is unable to measure gamma rays at the TeV scale because it simply does not have a large enough area to intercept an appreciable number of them. Additionally, any TeV-scale gamma ray that did pass through the LAT would be likely to create a shower too large for the calorimeter to measure its energy accurately. However, it is exactly the TeV scale that must be measured in order to understand sufficiently the processes responsible for the generation of the cascade. Without this information, any observed halo in the *Fermi* energy band would be difficult to interpret in the context of an EGMF. To accomplish these TeV measurements, one must return to the ground.

The Imaging Atmospheric Cherenkov Telescopes (IACTs) are sensitive to gamma rays in the approximate energy range from 100 GeV to greater than 30 TeV. Instead of observing the gamma ray directly, these instruments image the Cherenkov radiation from electromagnetic showers of particles initiated by the gamma ray's interaction with the atmosphere. The current generation of IACTs includes three telescopes that are presently operating, VERITAS, HESS, and MAGIC. Because these three instruments are qualitatively similar, I will focus here on a brief description of VERITAS in order to illustrate the IACT technique.

In the atmosphere, charged particles moving faster than the local speed of light emit Cherenkov radiation. Atmospheric showers of particles generated by very energetic gamma rays produce brief flashes of Cherenkov radiation with durations on the time scales of a few nanoseconds (Weekes, 1988). This light can be collected by telescopes on the ground, which produce an image of the shower as it propagates through the atmosphere. The amount of light collected by the telescope traces the energy of the shower; more energetic gamma rays will produce more shower particles and therefore more Cherenkov radiation. If multiple telescopes observe the shower, a stereo technique improves the reconstruction of the initial gamma ray direction, as shown in Figure 3.3.

The primary challenge for the IACTs is to discriminate the gamma-ray signal from the overwhelming cosmic-ray background. This can be accomplished by means of image selection. Gamma-ray showers tend to be more compact than showers initiated by hadrons because, in contrast to hadronic showers, they proceed primarily via electromagnetic channels (Weekes,

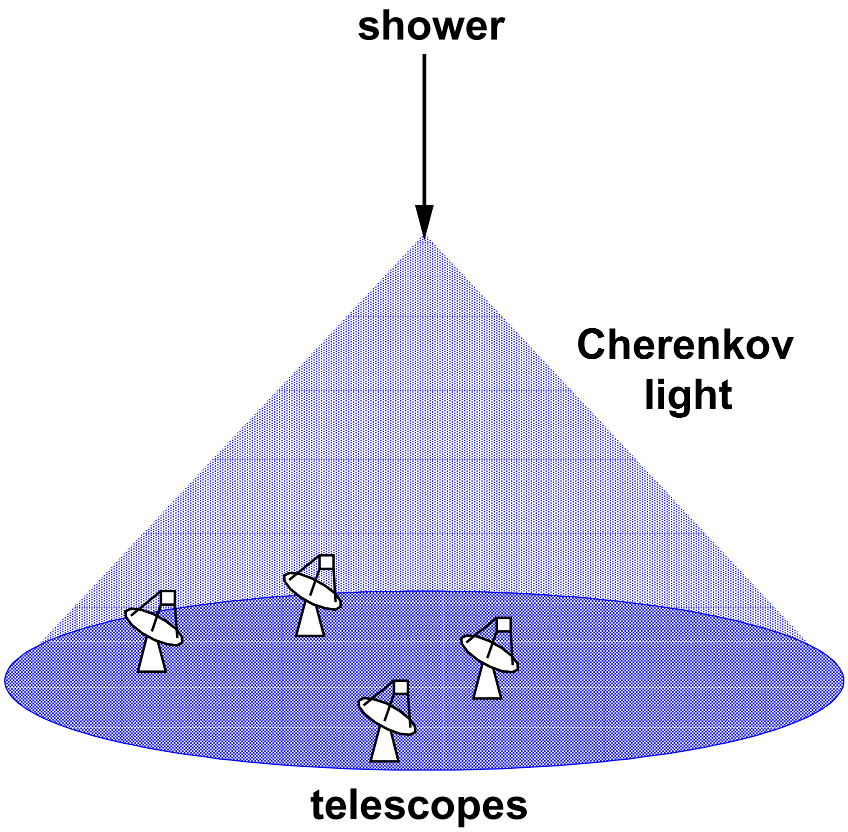

Figure 3.3: The stereo reconstruction technique employed by VERITAS, HESS, and MAGIC. Cherenkov light from atmospheric showers is imaged by individual telescopes. Combining the reconstructed directions from several telescopes greatly improves the overall reconstructed direction of the gamma ray.

1988). In general, gamma-ray showers tend to produce narrower images in the IACTs, which can be differentiated from the broader hadronic showers.

The increase in effective area granted by the Cherenkov imaging technique renders the IACTs more sensitive than *Fermi* to gamma rays when the primary energy is above ~100 GeV. VERITAS is sensitive to gamma rays in the energy range from 100 GeV to 30 TeV, with an effective area greater than 10^5 m^2, an energy resolution of 10% to 20%, and a 68% containment radius of better than 0.14° (Hanna et al., 2008). *Fermi* and the IACTs are therefore very complementary instruments, especially from the point of view of studying the EGMF cascades. While *Fermi* can measure the cascade directly in the critical GeV-scale energy range, the IACTs provide measurements of the direct emission, effectively constraining the total TeV-scale intrinsic emission that is responsible for the generation of the extragalactic cascade.

Although the shape of a typical cosmic-ray-induced shower is distinct from that of a typical gamma-ray-induced shower, the overwhelming majority of air showers are produced by cosmic rays. Some of these cosmic rays produce gamma-ray-like events, creating a background that must be subtracted (Hillas, 1996; Fegan, 1997). For this reason, IACTs infer the gamma-ray flux of the source by employing a background-subtraction method in which an "on" region around the source and an "off" region in which no source is expected are both observed, often in the same field of view. Data from the off region are then subtracted from data in the on region, and the significance of the result is determined (Li & Ma, 1983). The on region is typically defined by a cut on θ^2, where θ is the angle between the center of the "on" region and another point on the sky (Aharonian et al., 2006).

3.4 Other Detection Techniques

Gamma rays can also be detected by other techniques. At higher energies, the particles in the atmospheric shower may be sufficiently energetic to reach ground level, making direct observations of the shower particles possible. The Milagro experiment (MILAGRO Collaboration, 2006), which operated from 2000 to 2008 and the currently operational ARGO-YBJ experiment (Aielli et al., 2012) employed this method. Although the only extragalactic object detected so far by these experiments is the blazar Mrk 421 (Atkins et al., 2004), the successor to Milagro, HAWC, expected to become operational in the next few years (Deyoung & et al., 2010), promises to improve significantly the sensitivity of Milagro and will be able to perform monitoring observations of blazars at high energies.

CHAPTER 4

LIMITS ON THE EGMF FROM A SEMI-ANALYTIC MODEL

This chapter describes a method to characterize the extragalactic cascades using a semi-analytic model that was first presented by Huan et al. (2011). In addition to providing an illustrative and conceptually simple picture of the dominant physics processes in the cascade, the model can be evaluated relatively quickly with a modest investment of computing resources. In contrast to previous analytic models (Neronov & Semikoz, 2009; Tavecchio et al., 2010b; Dermer et al., 2011; Taylor et al., 2011), it accounts for the detailed geometry of the cascade and incorporates cuts on both the extent and duration of the cascade emission straightforwardly. This method of characterizing the cascade is complementary to models that include multiple generations of cascade but suffer certain other limitations, such as the assumption of an isotropic source made by Ahlers (2011).

4.1 Cascade Model

The geometry of the model is the same as that presented in Figure 2.12. For a blazar at a distance L from the observer, a gamma ray of energy E_γ emitted at an angle θ_S travels a distance L' before interacting. We employ the half-energy approximation inspired by Equation 2.12, so that the electron is created with energy $E_e = E_\gamma/2$. Assuming that the inverse Compton interactions proceed in the Thomson limit, the model uses Equation 2.20,

$$mc^2 \frac{d\gamma_e}{dt} \approx -\frac{4}{3}\gamma_e^2 \epsilon_0 c \sigma_T n_{\mathrm{CMB}}, \tag{4.1}$$

to approximate the rate of change of the electron's energy, while the rate of change of the angle θ_D, inspired from Equation 2.32, appears as

$$\frac{d\theta_D}{dt} = \frac{c}{r_L} = \frac{eBc}{mc\sqrt{\gamma_e^2 - 1}} \approx \frac{eB}{m\gamma_e}. \tag{4.2}$$

By combining Equations 2.20 and 4.2, we can solve for the angle through which an electron is deflected as it changes its Lorentz factor from γ_{e0} to γ_e. The solution is

$$\theta_{D0} = \frac{3eBc}{8\epsilon_0 n_{\mathrm{CMB}} \sigma_T}\left(\frac{1}{\gamma_e^2} - \frac{1}{\gamma_{e0}^2}\right). \tag{4.3}$$

Equation 4.3 assumes that B represents the magnetic field strength perpendicular to the direction of travel of the electron. To attain full generality, the model converts B into the total strength of the field by introducing the angle θ_F, which is the angle of the field relative to the electron's trajectory. Equation 4.3 then generalizes to

$$\theta_D = \cos^{-1}\left(\sin^2\theta_F \cos\theta_{D0} + \cos^2\theta_F\right). \tag{4.4}$$

Turning to the secondary gamma rays produced via inverse Compton scattering, we consider an electron that changes its Lorentz factor from $\gamma_e + d\gamma_e$ to γ_e. This electron will produce upscattered CMB photons with energies between E and $E + dE$ if the original energy ϵ_{CMB} of the CMB photons is between $3E/4\gamma_e^2$ and $3(E + dE)/4\gamma_e^2$, according to Equation 2.19. The differential number of secondary gamma rays dN is then the product of the rate of inverse Compton scattering interactions, the number of CMB photons within this energy range, and the time dt over which the interactions occur:

$$dN = c\sigma_T dt \frac{8\pi\epsilon_{\mathrm{CMB}}^2 d\epsilon_{\mathrm{CMB}}}{(hc)^3\left(e^{\epsilon_{\mathrm{CMB}}/kT} - 1\right)} = c\sigma_T dt \frac{27\pi E^2 dE}{8\gamma_e^6 (hc)^3\left(e^{3E/4\gamma_e^2 kT} - 1\right)}. \tag{4.5}$$

The temperature T of the CMB is assumed to be 2.73 K, k is the Boltzmann constant, and h is Planck's constant. For a mean free path $\lambda(E_\gamma)$, shown for example in Figure 2.11, the probability of interaction within a distance dl after a gamma ray travels a distance l is

$$P = e^{-l/\lambda(E)} \frac{dl}{\lambda(E)}, \tag{4.6}$$

where for the case of primary gamma rays, $l = L'$. Since the electrons travel only a few kpc before interacting while the mean free path for gamma rays below a few hundred TeV is much longer, the apex of the triangle in Figure 2.12 is pointlike, and the distance traveled by secondary gamma rays is

$$l' = \sqrt{L^2 + L'^2 - 2LL'\cos(\theta_D - \theta_C)}. \tag{4.7}$$

The probability of primary interaction followed by secondary survival can therefore be written as

$$dP = e^{-L'/\lambda(E_\gamma)} \frac{dL'}{\lambda(E_\gamma)} e^{-(\sqrt{L^2+L'^2-2LL'\cos(\theta_D-\theta_C)})/\lambda(E)} f(E_\gamma, \theta_S) g(\theta_F), \tag{4.8}$$

where we include the blazar flux $f(E_\gamma, \theta_S)$ from Equation 3.1 as a weighting factor, the angle $\theta_S = \theta_D - \theta_C$, and θ_D is given by Equation 4.4. The factor $g(\theta_F)$ permits the specification of a particular field geometry. If we assume no special knowledge about the field, then all field directions are equally likely and $g(\theta_F) = \sin\theta_F$, which is the assumption adopted in the model.

By combining Equations 4.8 and 4.5, and using Equation 2.20 to convert the time integral dt into an integral over γ_e, the model predicts the observed spectrum of secondary gamma rays from the source. This is given by

$$\begin{aligned} \frac{dN}{dE} = \int d\gamma_e \frac{81\pi E^2 m}{16h^3 c\gamma_e^8 \epsilon_0 n_{\mathrm{CMB}} \left(e^{3E/e\gamma_e^2 kT} - 1\right)} \int d\theta_F \sin(\theta_F) \int dE_\gamma \times \\ \times \int dL' e^{-L'/\lambda(E_\gamma)} \frac{dL'}{\lambda(E_\gamma)} e^{-(\sqrt{L^2+L'^2-2LL'\cos(\theta_D-\theta_C)})/\lambda(E)} f(E_\gamma, \theta_S), \end{aligned} \tag{4.9}$$

where an additional factor of 2 appears because each pair production interaction produces both an electron and a positron.

Before we can evaluate Equation 4.9, first we must determine the limits on the various integrals. The limits on θ_F are simply 0 to $\pi/2$. For the integral over primary gamma ray energies E_γ, the physical lower bound from the pair production threshold suggests a minimum of $2\gamma_e mc^2$. We select an upper limit on E_γ of 200 TeV to reduce the dependence of the model on interactions that occur too close to the blazar and thus sample the local cluster fields instead of the EGMF. In practice, models with cutoff energies larger than ~ 50 TeV do not fit the data well, so the precise value of this limit does not matter, except to provide an upper limit of 200 TeV$/2mc^2$ on γ_e, which arises because of our assumption that the electron is produced with half of the gamma ray's energy. To facilitate the computation, we also adopt a lower limit on γ_e of 10^5, which restricts the range of the model to secondary gamma rays with energies above 100 MeV, under the assumption that the CMB becomes negligible above 7.5 meV.

The integration over L' is the most complicated because it determines the physics of the cascade. Following Figure 2.12, we can write the angle θ_C as

$$\theta_C = \sin^{-1}\left(\frac{L'}{L}\sin\theta_D\right), \tag{4.10}$$

with θ_D given by Equation 4.4. Similarly, the time delay ΔT of a secondary gamma ray with respect to a primary gamma ray that travels from the source to Earth without interaction can be found from the difference in the path lengths:

$$c\Delta T = L' + \sqrt{L^2 + L'^2 - 2LL'\cos(\theta_D - \theta_C)} - L. \tag{4.11}$$

Equations 4.10 and 4.11 translate cuts on θ_C and ΔT into limits on the L' integration, so the model is able to account for limits on the angular extent and duration of observations in a natural way.

Although we assume no *a priori* knowledge about the field direction, we do make the assumption that the unknown field direction is constant over the entire trajectory of the electron, which means that the model represents a field coherent over the electron cooling length. A high-energy electron in the CMB cools to a Lorentz factor of 10^5 over a distance of $L_0 \approx 0.7$ Mpc. If the EGMF coherence length is smaller than this value, then the electron's propagation can be viewed as a random walk through regions of varying field direction (Neronov & Semikoz, 2009), and a stronger field would be necessary to deflect the electron by the same amount as a field coherent over L_0. This point of view suggests that we can scale the strength of the EGMF by

$$B(L) = B(L_0)\sqrt{\frac{L_0}{L}}, \tag{4.12}$$

for $L < L_0$, so that the effects of a field strength $B(L)$ with coherence length L are roughly similar to those of a weaker field $B(L_0)$ with coherence length $L_0 \geq L$. Equation 4.12 is of course an approximation because the cooling length of the electron depends on the Lorentz factor at which the electron is considered "cool," and therefore on the energy of the observed cascade photon.

Finally, the evaluation of Equation 4.9 relies on the calculation of the mean free path $\lambda(E)$, which in turn depends on EBL. We elect to use the EBL from Franceschini et al.

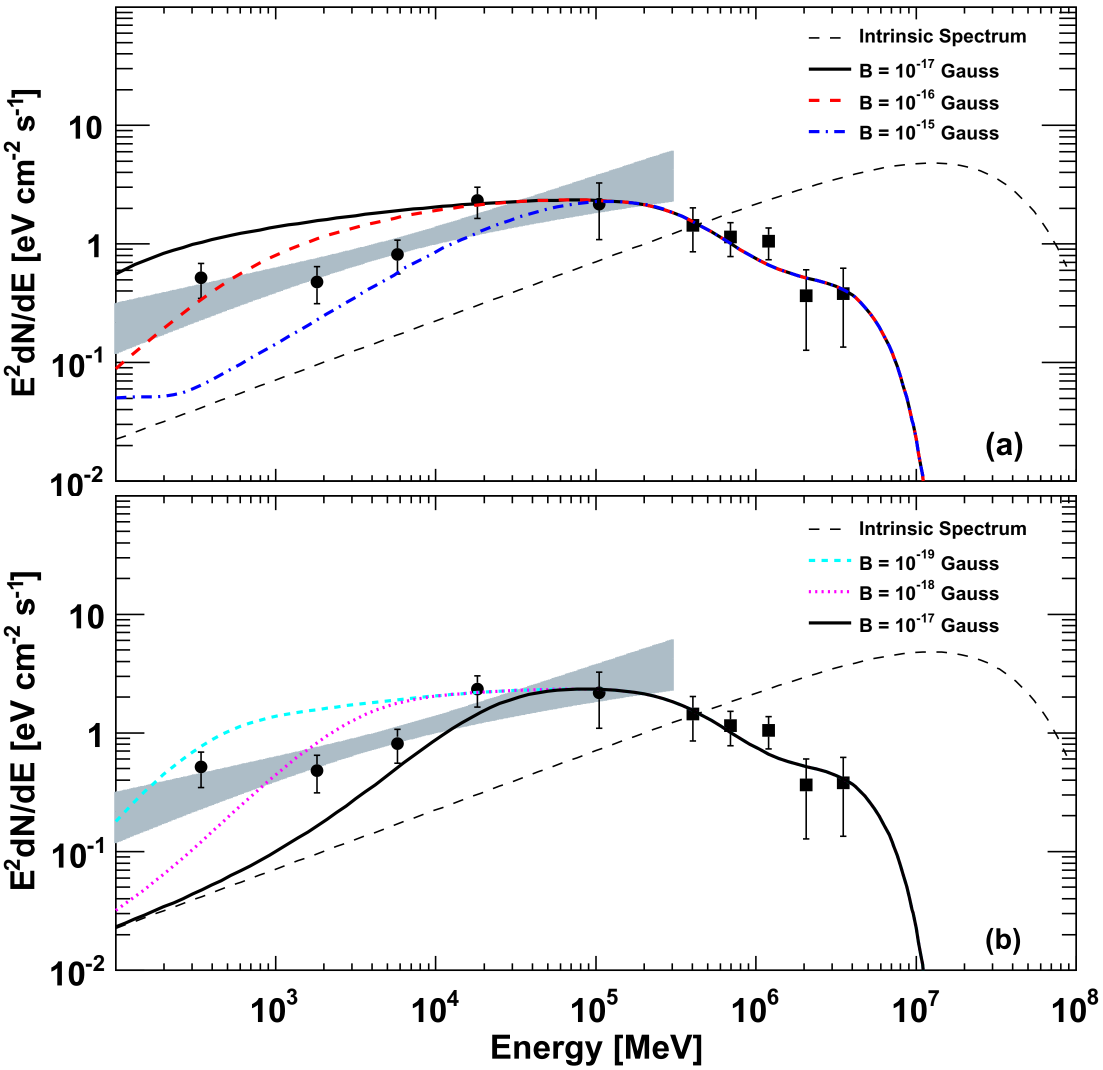

Figure 4.1: Example fits of the model's predictions for the spectrum to data, weighted by E^2, from Huan et al. (2011). The points are from VERITAS and *Fermi* observations of the blazar RGB J0710+591 over a three-year period. Panel (a) shows the results under the assumption that the blazar has been active long enough to average over all time delays in the cascade. Panel (b) conservatively assumes that the blazar has been active only for the three-year duration of the observations.

(2008) because, as shown in Figure 2.1, it is relatively low and therefore gives a lower flux for the cascade. With less sensitivity to the EGMF signal, our results are conservative.

4.2 EGMF Predictions and Limits

Figure 4.1 shows the predictions of Equation 4.9 for the blazar RGB J0710+591. In the figure, we have assumed a spectral index of $\alpha = 1.5$, a cutoff energy of $E_C = 25$ TeV, and a bulk Lorentz factor of $\Gamma = 10$. This intrinsic spectrum is indicated by the thin dashed line. Data from observations by both *Fermi* and VERITAS are included as spectral points, and the spectrum of observable emission is shown for a variety of field strengths. We select the θ^2 cut from Acciari et al. (2010) as the limiting value of θ_C^2 in the VERITAS energy range, while for θ_C in the *Fermi* energy range we use the 68% containment radius of the *Fermi* LAT, which we derive based on the actual pointing of the instrument over the course of the observations. We produce the *Fermi* data points by conducting an unbinned analysis using the *Fermi* tools as described in Section 3.2. Since these data points exhibit consistency with the confidence interval, shown as a light gray band in the figure, we are confident that they are representative of the observed spectrum in the *Fermi* energy range.

The top panel of Figure 4.1 presents predicted curves for an EGMF strength varying between 10^{-17} and 10^{-15} Gauss. The effects of the EGMF are clearly evident: as the field increases, more of the cascade is deflected away from the line of sight, reducing the total secondary emission in the *Fermi* energy range. Since the energy of the secondary gamma ray increases monotonically with the energy of the electron that created it, and electrons of higher energy interact sooner and are influenced less by the field than electrons of lower energy, the effect of the EGMF on the cascade is most pronounced at smaller gamma ray energies, and it gradually manifests in the upper ranges of the *Fermi* energy range as we continue to raise the field strength.

Because we are interested primarily in the EGMF, it is desirable to reduce the dependence of our results on the specific properties of the blazar. One unknown property is the duration of activity prior to the observations, which we call the lifetime of the blazar. In the most conservative case, we assume that the blazar has been active only for the three years during which *Fermi* and VERITAS have observed it. The bottom panel of Figure 4.1 demonstrates how the curves change if we make this most conservative assumption. Very roughly speaking, the magnetic field necessary to produce a given degree of deflection decreases by two orders of magnitude in the conservative case. I will elaborate on this point at the end of the section.

Another unknown property of the blazar is the detailed shape of the intrinsic spectrum.

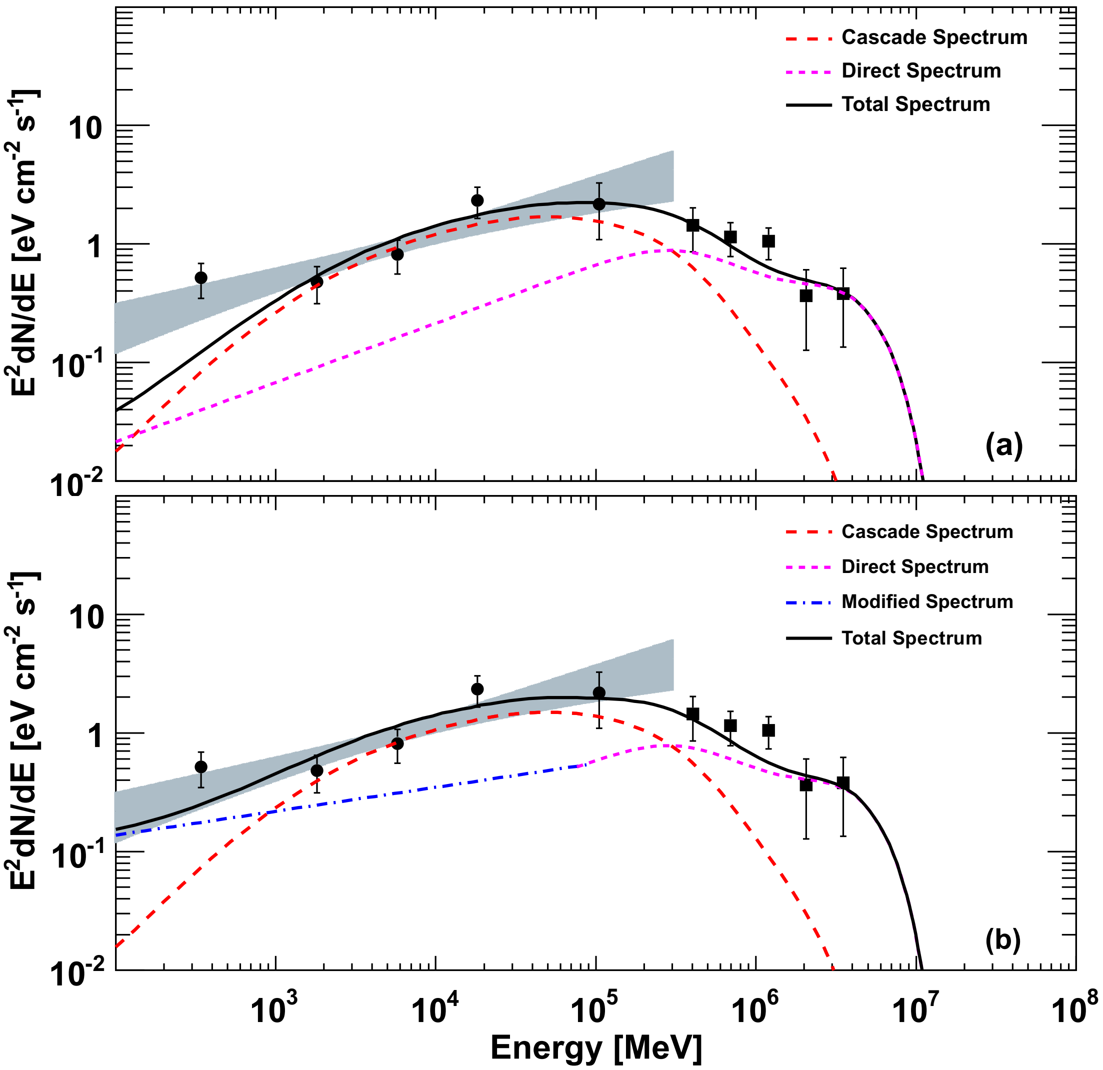

Figure 4.2: Example fit for $B = 3 \times 10^{-16}$ Gauss, from Huan et al. (2011). Panel (a) shows the fit without any additional component in the *Fermi* energy range. Panel (b) shows that the assumption of an additional component can improve the fit.

While we might expect to capture the essence of the spectrum with the model of Equation 3.1, it is always possible that there could be additional components contributing to the flux, as explored by Böttcher et al. (2008), for instance. If we account for the possibility of such components existing in the *Fermi* energy range, modifications to the curves for higher fields in Figure 4.1 could arise that would render them a better match to the data. Figure 4.2 shows an example of this procedure for a field strength of 3×10^{-16} Gauss, again for a spectral index of $\alpha = 1.5$, cutoff energy $E_C = 25$ TeV, and bulk Lorentz factor $\Gamma = 10$.

In the top panel, the total emission from cascade and direct contributions is well below the observed data points. By introducing a spectral break in the intrinsic power law below 80 GeV, where the photons are free streaming throughout a Hubble radius and therefore have no effect on the cascade emission, we find in the bottom panel that the data can be matched reasonably well. However, in the case of low fields that match the data poorly, nothing can be done to improve the fit because the total emission is above the observed data points and any additional components will serve to make the fit even worse.

Because the details of the intrinsic spectrum are unknown, for a given field strength B, we scan the parameter space of spectral index α and cutoff energy E_C in a search for the intrinsic spectrum that fits the data best, using the χ^2 value from the fit as our test statistic. Figure 4.3 shows the results of this scan for a field strength of $B = 0$ (top) and $B = 10^{-16}$ Gauss (bottom). The best-fit intrinsic spectrum, where the χ^2 value is minimized, is indicated by a white asterisk. Since the asterisk is far from the edges of the plots in both cases, this minimum is likely global. Additionally, the best-fit χ^2 value is somewhat lower in the $B = 10^{-16}$ Gauss case, indicating that it is generally a better fit.

When the test statistic from the scan is projected onto the field strength axis, we expect that the difference in χ^2 between the true field strength and the minimum of the test-statistic curve will be distributed as a χ^2 distribution with one degree of freedom (James, 2006). This allows us to reject values of the field at a given confidence level. Figure 4.4 exhibits this projection for a variety of values for the source lifetime. In the case where the lifetime is essentially unlimited, the cascades are fully developed in extragalactic space and the measured flux is averaged over all possible time delays. This case appears as the solid black line in Figure 4.4. The other curves of Figure 4.4 result from assuming an upper limit on the lifetime of the blazar, which translates into an upper limit on the time delay. In this case, the measured flux is an average over those gamma rays in the cascade that arrive within the time limit.

For each curve in Figure 4.4, we find the point on the curve that surpasses the minimum by the appropriate value for a confidence level determined from a $\chi^2(1)$ distribution. The value $\Delta\chi^2$ by which the curve must surpass the minimum for select confidence intervals appears in Table 4.2. Figure 4.4 indicates the limits for 90% and 95% confidence limits for the one-year and unlimited lifetime cases, but we omit the limits for the other lifetimes for the sake of clarity. In the unlimited lifetime case, we determine a lower limit of $B > 2 \times 10^{-16}$ Gauss on

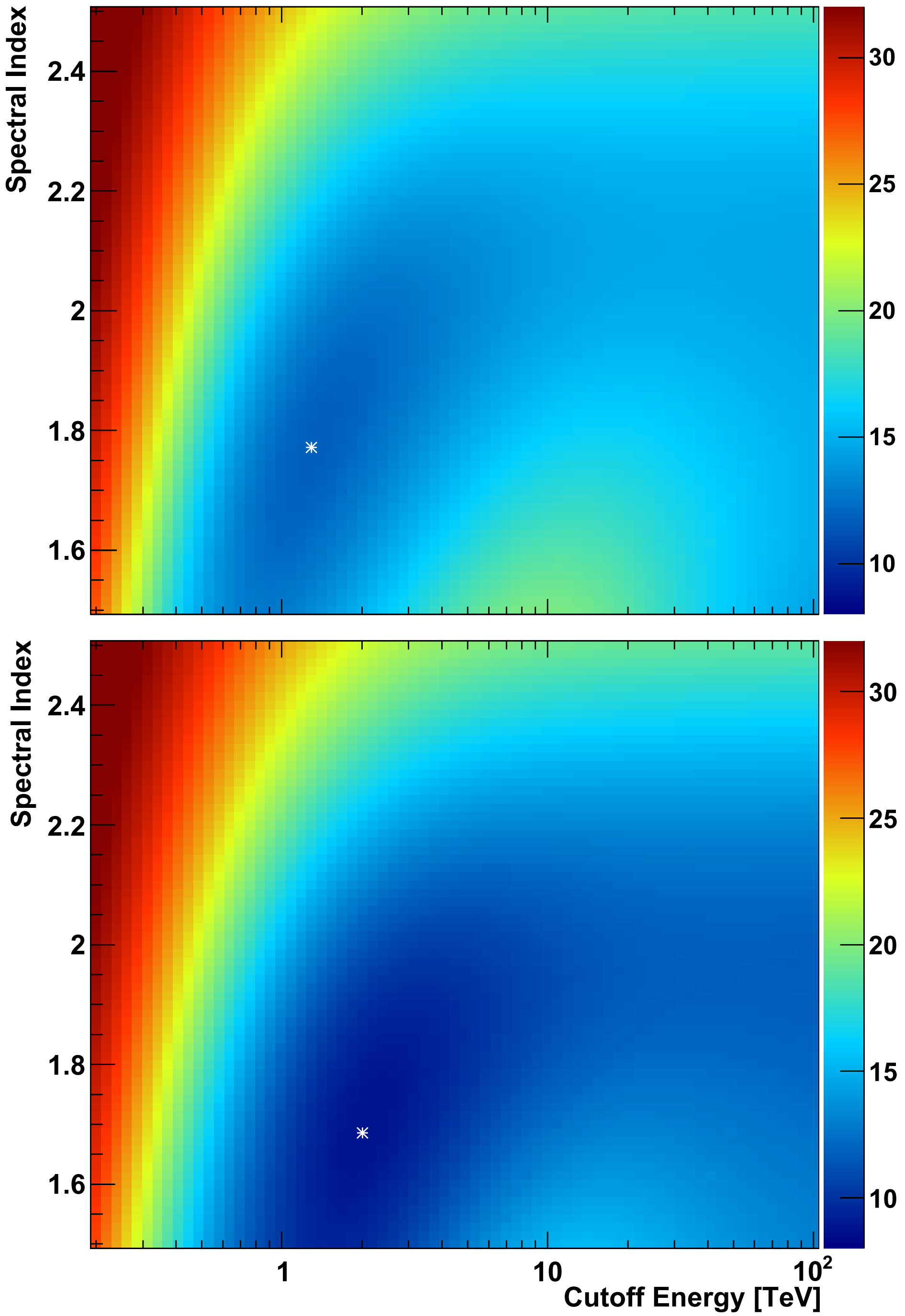

Figure 4.3: Maps of the χ^2 value from a fit to the RGB J0710+591 data, as a function of cutoff energy and spectral index. The top plot is for an EGMF strength of $B = 0$. The bottom plot is for $B = 10^{-16}$ Gauss.

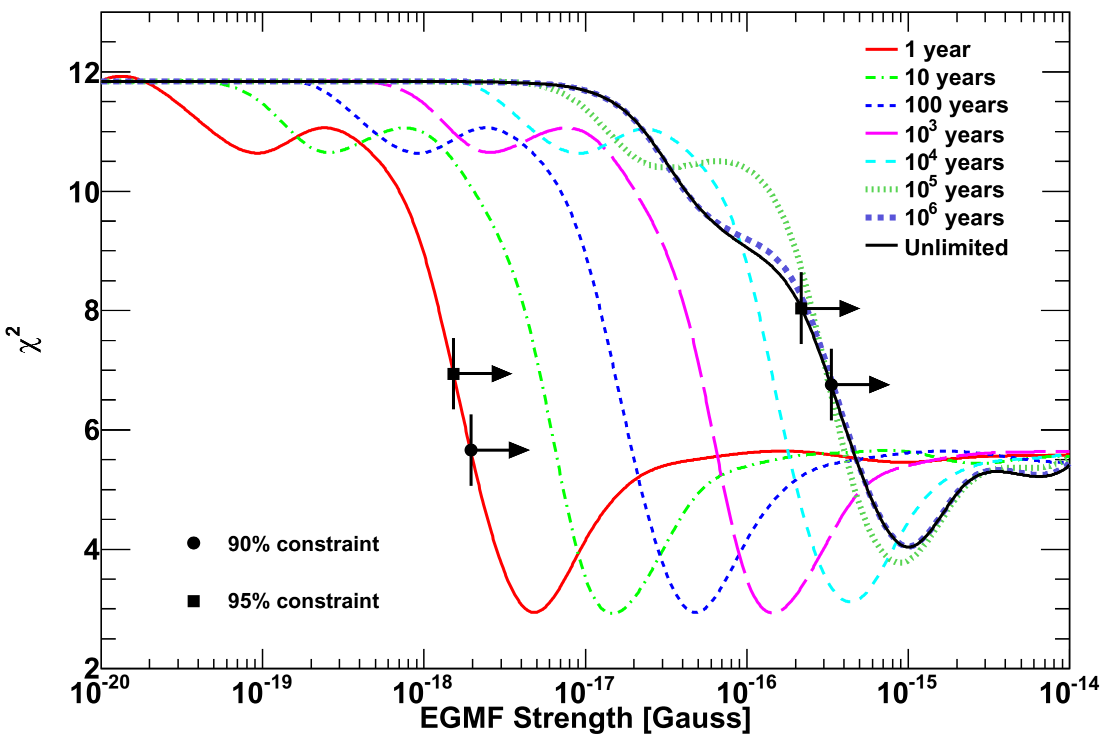

Figure 4.4: Test-statistic curves from the intrinsic-spectrum scan, projected onto the EGMF field strength axis, from Huan et al. (2011).

Confidence level	$\Delta\chi^2$
68.3%	1
90%	2.72
95%	3.84
99%	6.66

Table 4.1: Select confidence limits from a $\chi^2(1)$ distribution.

the EGMF strength along the line of sight to RGB J0710+591 at a confidence level of 95%. This limit relaxes by about two orders of magnitude to $B > 3 \times 10^{-18}$ Gauss if the lifetime is restricted to the most conservative case, corresponding to the ~ 3 years of observations. Due to the uncertainties in the EBL, the assumptions made in constructing the model, and the unknown detailed structure of the EGMF, these limits should be thought of as order-of-magnitude estimates, rather than firm lower limits. However, the statistical methods used to derive them are rigorous and represent the best estimate given the assumptions and the limited information available.

The curves in Figure 4.4 begin to converge to the unlimited-lifetime case at a time delay of $\sim 10^5$ years. In order to explain this, it is instructive to examine the relationship between the angular cut θ_C and the cut on the lifetime. Equations 4.10 and 4.11 can be combined, along with a small-angle approximation, to relate these two cuts:

$$\Delta T \approx \frac{L}{2c}\left[\frac{\left(1-\frac{L'}{L}\right)}{\frac{L'}{L}}\right]\theta_C^2. \tag{4.13}$$

Assuming the term in brackets is of order unity when we average over primary gamma-ray energies, we find for a blazar at a distance $L = 500$ Mpc that Equation 4.13 gives $\Delta T \approx 8 \times 10^8 \theta_C^2$ years. The *Fermi* PSF varies over the energy range of interest from 0.1 to a few degrees. Using these values for θ_C, I find that the time delay corresponding to the PSF is between 2×10^3 and 4×10^6 years, very much in line with the $\sim 10^5$ years implied by Figure 4.4. If the blazar lifetime is taken to be smaller than this value, then it is more constraining than the cut due to the PSF and the limit on the field varies with the lifetime. For longer lifetimes, the fixed PSF becomes more constraining than the lifetime cut, and the curves converge to the unlimited-lifetime case.

Under the small-angle approximation, θ_C is proportional to θ_D by Equation 4.10, and Equation 4.3 demonstrates that θ_D is proportional to the field strength B. Combining these results with Equation 4.13, we find that B scales with $\sqrt{\Delta T}$ for time delays below $\sim 10^5$ years. Figure 4.5 reinforces this estimate, demonstrating the expected scaling of B with the lifetime and showing the saturation at $\sim 10^5$ years. Since the duration of the observations is about four orders of magnitude below this value, we expect the limit on the field to be about two orders of magnitude smaller than the unlimited-lifetime case. This is indeed what is observed.

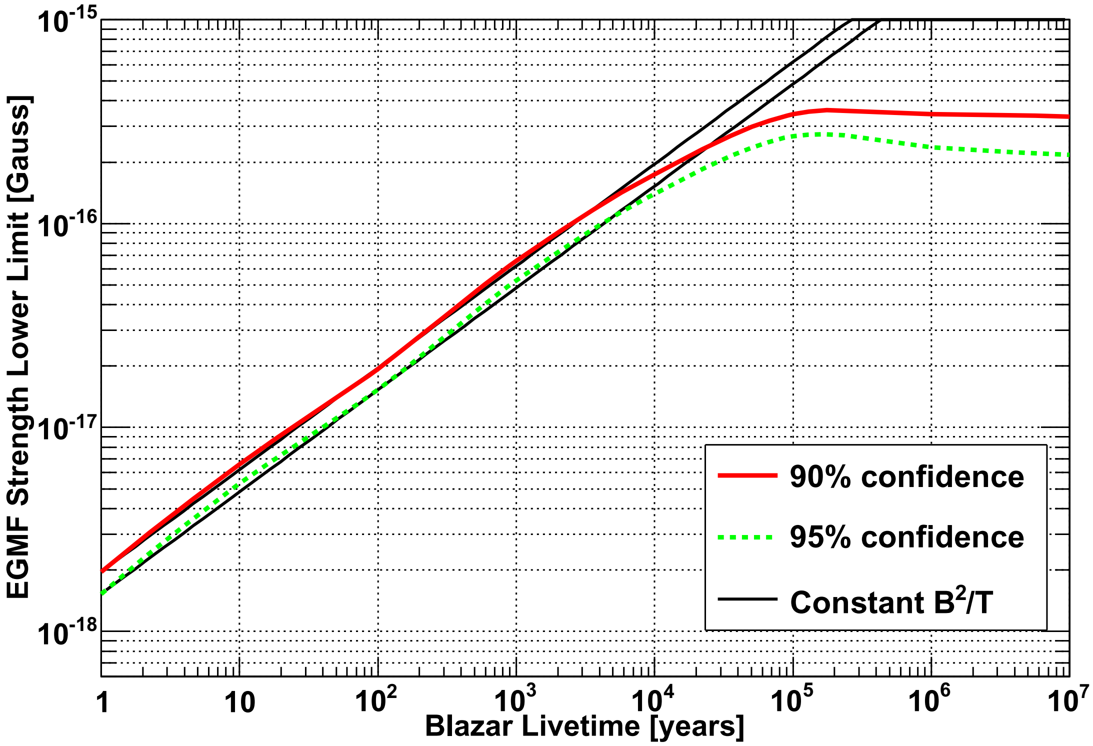

Figure 4.5: Limit on the EGMF as a function of blazar lifetime for 90% and 95% confidence intervals, from Huan et al. (2011). The solid black lines indicate the expected scaling of B with $\sqrt{\Delta T}$.

4.3 Accuracy and Domain of Validity

We have made a number of assumptions in the construction of the semi-analytic model. While some of these are justified on strong physical grounds when the system under study is considered, others restrict the domain of validity of the model. This section discusses the most important of these assumptions.

Instead of using the complete energy distributions for the product particles from pair production and inverse Compton scattering, the model adopts a half-energy approximation for the former and assumes that the latter proceeds in the Thomson limit. For interactions with CMB photons at 0.6 meV, the Thomson limit assumption demands that the primary energy be much smaller than 400 TeV if we are interested in secondary gamma rays above 100 MeV. Multigenerational cascades, which are also neglected by the model, become important when the primary energy exceeds ∼ 20 TeV. Even in this case, the total power due to second-generation gamma rays is expected to be modest (Tavecchio et al., 2010a).

The model ignores the effects of cosmic expansion except in the calculation of the mean free path $\lambda(E)$ of primary gamma rays propagating from the source redshift through the EBL. Since cosmic expansion, energy redshift, and the detailed evolution of the EBL and CMB are ignored, the model is applicable only to nearby sources at $z \lesssim 0.2$. We have also assumed that the EGMF is coherent over the entire trajectory of the electrons and positrons. As a result, our model is valid provided the EGMF coherence length is larger than 1 Mpc.

Another limitation of the model arises from the assumption that gamma rays falling outside the 68% containment radius of the *Fermi* LAT will not be detected. A more appropriate analysis would account fully for the effects of the PSF on the extended emission from the blazar. However, this would require a detailed model for the energy-dependent morphology of the cascade. In order to construct this, we would need to select sets of upper and lower θ_C cuts and perform an evaluation of Equation 4.9 for each set of cuts, substantially increasing the computation time.

All of the above limitations on the domain of validity of the model argue for a Monte Carlo simulation. This solution could employ the complete energy distributions of the fundamental processes, model the EGMF when the coherence length is smaller than the cooling length of the electrons, account for redshift and the expansion of space, and follow multiple generations of the cascade. I explore the development of such a simulation and its application to *Fermi* and IACT data in the next two chapters.

CHAPTER 5
MONTE CARLO SIMULATION

Monte Carlo methods employ pseudo-random numbers generated by computer simulation to model the behavior of physical systems. The extragalactic cascades depend on stochastic processes that are well suited to this type of solution. This chapter focuses on the development of a Monte Carlo simulation of gamma-ray propagation in extragalactic space and discusses methods to ensure that the statistical sample generated from running the simulation is adequate to characterize the cascades. Chapter 6 employs the simulation in a search for the EGMF.

The primary advantages of the Monte Carlo simulation over the semi-analytic model presented in Chapter 4 are the ability to model multigenerational cascades, the use of the full relativistic cross sections for the pair production and inverse Compton scattering processes, the inclusion of redshift effects, and the freedom to alter the EGMF model geometry. Its primary disadvantage is the relatively large processing time necessary for ensuring adequate statistics.

5.1 Capabilities and Accuracy

The reliability of the Monte Carlo simulation can be assessed based on a set of tests of simple cases that can be computed analytically. While no set can demonstrate exhaustively the accuracy of the Monte Carlo, I seek to determine, at least qualitatively, that the primary processes on which the cascade characterization relies are accurately modeled. These include the kinematics of the pair production and inverse Compton interactions, particle tracking through the EGMF, and proper accounting for redshift effects due to the expansion of space.

5.1.1 Modular Design

Our simulation is designed with the various physical effects modeled as individual modules that can be easily incorporated or excluded from the simulation. It is straightforward to remove modules systematically in order to determine which processes are responsible for different effects in the cascade. Additionally, the simulation serves as a framework in which new modules can be built and tested relatively rapidly to study other physical effects.

The main assumptions implicit in the Monte Carlo code are as follows:

- Both continuous and discrete processes can be modeled. Continuous processes alter the dynamic properties of the tracked particles as they propagate, while discrete interactions involving background particles occur at specific points in spacetime.
- We assume that the background particle populations are isotropic and homogeneous. Any type of background particles can be included; they need not be photons.
- Interactions occur between two particles but can produce an arbitrary number of secondary particles. The primary particle can survive the interaction, or it can be destroyed.

The particles of the cascade are tracked via comoving coordinates in a fully three-dimensional expanding space. Stepper routines, described in detail in Section 5.1.3, follow the evolution of the dynamic properties of each cascade particle with a predetermined level of accuracy. Each continuous process specifies its contribution to the rate of change of momentum for the tracked particle, while each discrete process requires a table of the mean free path of the tracked particle as a function of its energy and redshift. The construction of the tables proceeds by evaluating Equations 2.25 and 2.26. These tables can be computed either at simulation run-time or in advance, although the latter case saves a great deal of processing time if the simulation is run repeatedly.

5.1.2 Particle Kinematics

Our simulation employs the full relativistic cross sections for pair production and inverse Compton scattering as given by Equations 2.8 and 2.16, respectively. The code samples the target photon energies from the mean free path tables and other kinematic variables from the results of Protheroe (1986) for pair production or Jones (1968) and Blumenthal & Gould (1970) for inverse Compton scattering. The properties of the product particles from the interaction are then determined based on the relativistic kinematics as discussed in Sections 2.2.1 and 2.3.1. In this section, I summarize the kinematics of both relevant interactions and demonstrate the code's ability to reproduce simple results. Although I make simplifying assumptions in determining the analytic results, of course the code employs the general solution in each case.

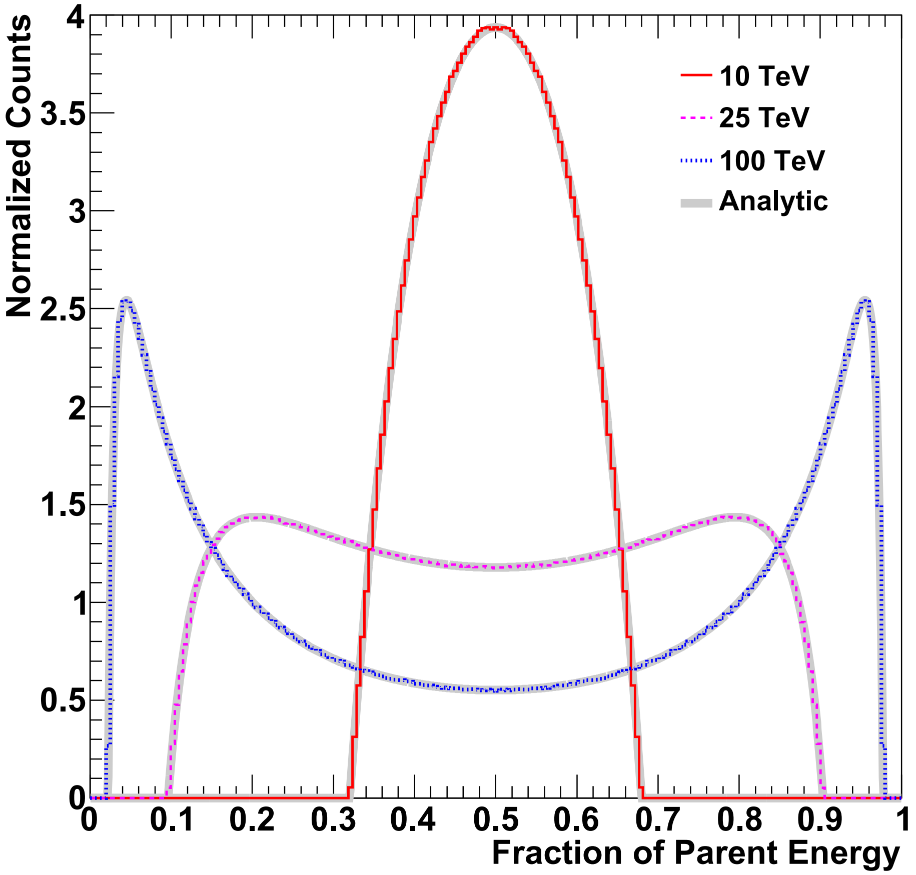

Figure 5.1: Distribution of product electron and positron energies from gamma rays undergoing pair production on a 30-meV monoenergetic background. Primary gamma rays are injected at 10, 25, and 100 TeV. The histograms are from the Monte Carlo simulation, while the gray lines are from the analytic calculation of Zdziarski (1988).

Zdziarski (1988) has computed the distribution of product photon energies for pair production interactions on an isotropic background with an arbitrary spectrum. Figure 5.1 shows the simulated results from our code when the background consists of monoenergetic photons of energy $\epsilon = 30$ meV. This energy is at the high-energy edge of the infrared peak in the EBL. Analytic predictions from Zdziarski (1988) also appear in the figure. The code clearly matches the predicted values very well. Figure 5.1 highlights the inadequacy of the half-energy approximation when the gamma-ray energy is large; as one of the product leptons acquires most of the primary's energy, the distribution of particle energies in the cascade may change significantly.

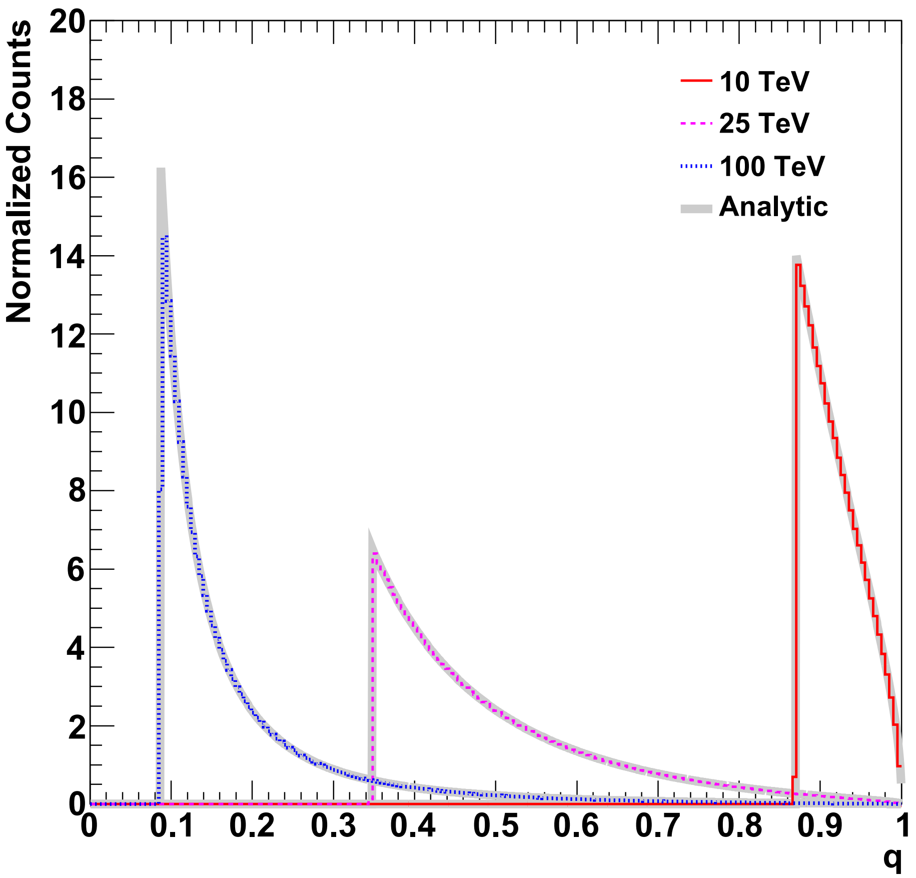

Figure 5.2: Distribution of q for pair production targets when the background is monoenergetic at 30 meV, along with analytic predictions.

Due to relativistic and geometric effects, the distribution of directions of target photons that interact is not isotropic, despite the isotropic nature of the background population. By inspection of Equation 2.25, it is clear that the appropriate distribution is $\sigma_{\gamma\gamma}(q)/q^3$. When q is sampled from this distribution, Equation 2.2 determines the angle of the target photon. Figure 5.2 demonstrates that the sampling of q from the code[1] is in line with our expectations from Equation 2.25.

The final kinematic variable that must be sampled for pair production is the angle of emission of the electron with respect to the gamma ray's direction. This angle is labeled as α' in Figure 2.3 and its distribution is given by Jauch & Rohrlich (1976). In the center of

---

[1] In practice, the code samples from the distribution in terms of the Mandelstam variable s; however, this is a matter of semantics.

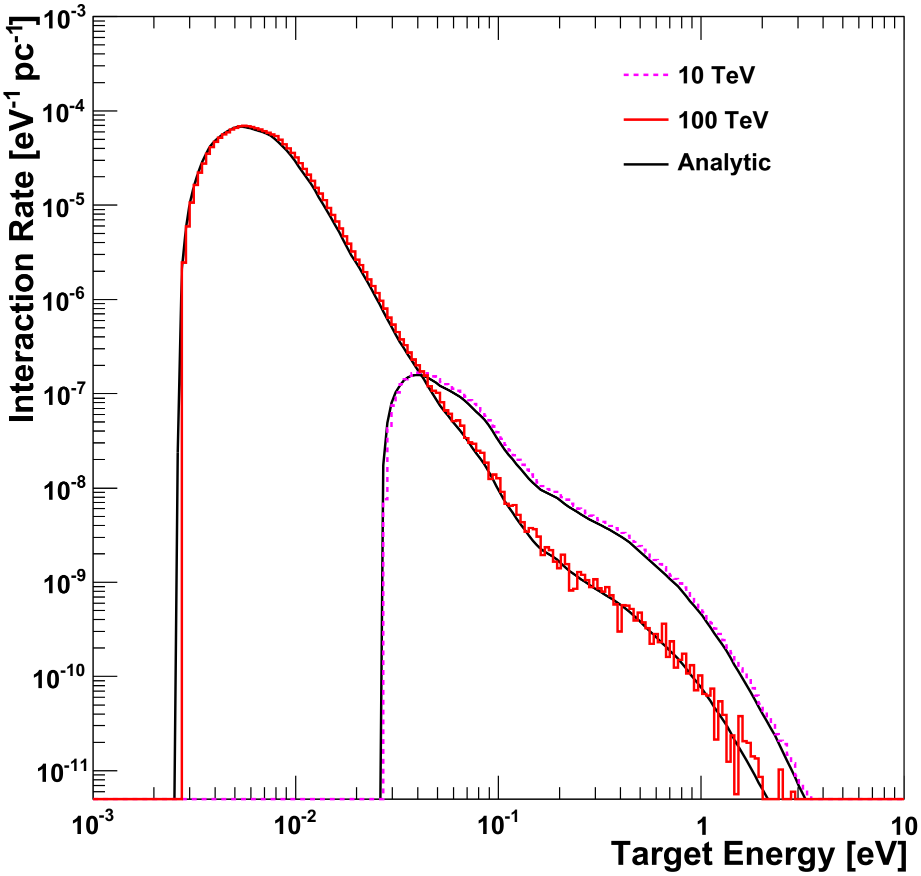

Figure 5.3: Distribution of target energies for pair production on the EBL of Franceschini et al. (2008), at a redshift of $z = 0.1$. The black curves indicate the expected distributions of target energies from Equation 2.25.

momentum frame, the azimuthal angle of the outgoing electron is sampled from a uniform distribution. This procedure is necessary because the physics in the center of momentum frame exhibits azimuthal symmetry with respect to the direction of the primary photon, and not with respect to the boost direction, making the azimuthal angle important in the return boost. The code calculates the momenta of the leptons in the center of momentum frame according to the discussion in Section 2.2.1. A boost back into the lab frame then produces the trajectories of the electron and positron, which are added to the tracked particles in the cascade.

Figure 5.3 displays the distributions of target energies for pair production interactions on the full EBL as given by Franceschini et al. (2008), along with the expected distribution of

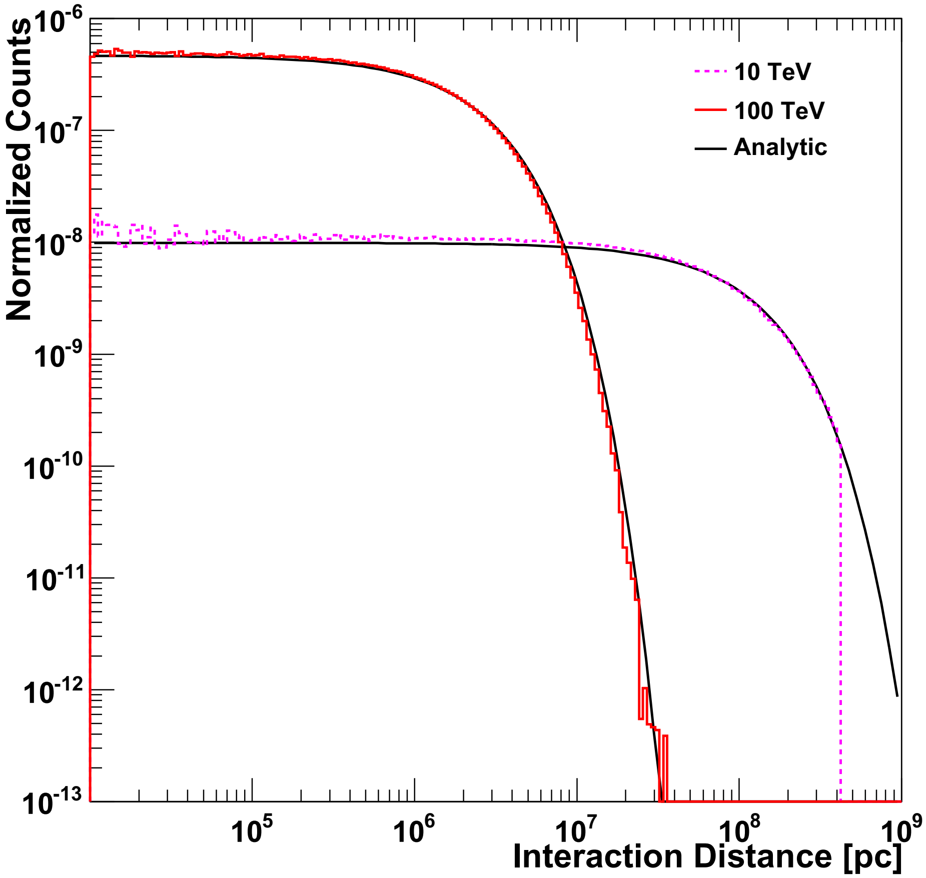

Figure 5.4: Distribution of interaction lengths for pair production on the EBL of Franceschini et al. (2008), at a redshift of $z = 0.1$. The black curves indicate the evaluation of Equation 2.25.

target energies from Equation 2.25. In the figure, the primary gamma rays are injected at a redshift of $z = 0.1$. The distributions of their interaction lengths appear in Figure 5.4, along with the predictions from integrating Equation 2.25, again showing good agreement. The cutoff in the distribution of 10-TeV gamma-ray interaction lengths at 420 Mpc is expected because this is the distance to a source at $z = 0.1$ and the gamma rays are not tracked beyond a distance equal to the comoving distance between the source and the observer. That is, 10-TeV gamma rays that survive the propagation from the source to Earth are not included in the histograms in Figure 5.4. Obviously no such cutoff is manifest in the distribution of 100-TeV gamma rays because their mean free path is much smaller and all of them interact.

We adopt a similar approach in testing the accuracy of inverse Compton scattering in

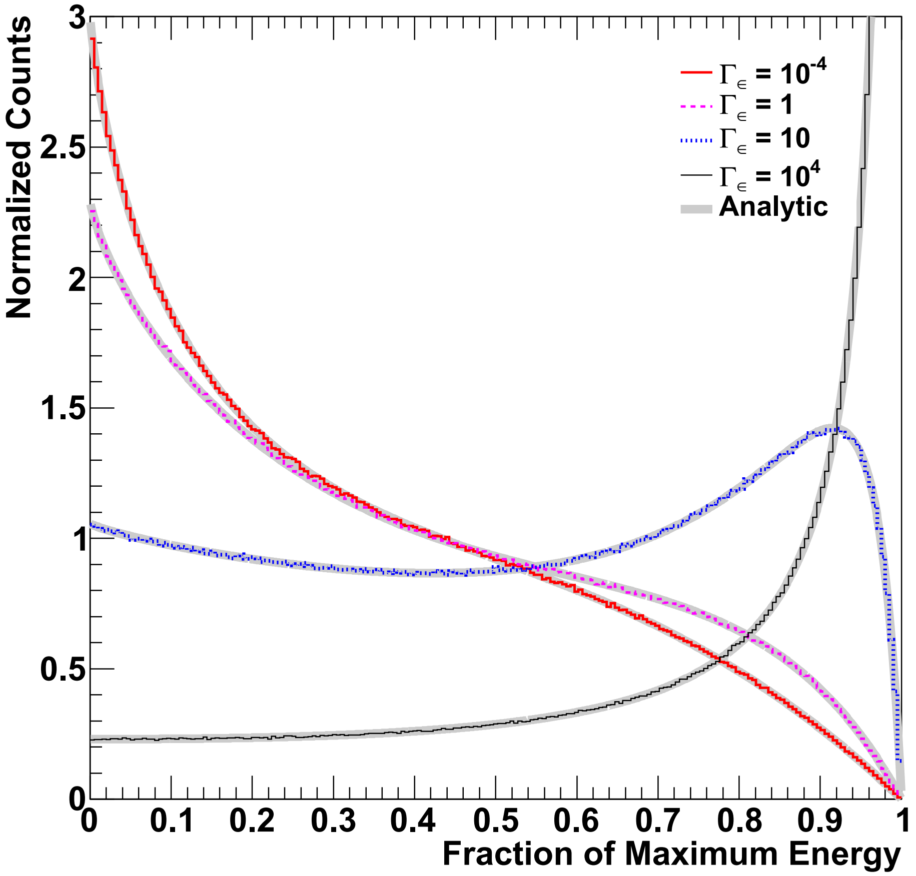

Figure 5.5: Distribution of product gamma-ray energies from inverse Compton scattering as a fraction of maximum possible energy, with predictions from Jones (1968).

the code. Following Blumenthal & Gould (1970), we use the parameter

$$\Gamma_\epsilon = \frac{4E_e\epsilon}{(mc^2)^2}, \tag{5.1}$$

where E_e and ϵ are the electron and target photon energies, respectively, to characterize the domain of the scattering[2]. The maximum possible energy of the upscattered gamma ray in terms of the electron energy E_e is then

$$E_{\max} = \frac{\Gamma_\epsilon}{1+\Gamma_\epsilon} E_e. \tag{5.2}$$

---

[2] Thomson scattering corresponds to $\Gamma_\epsilon \ll 1$.

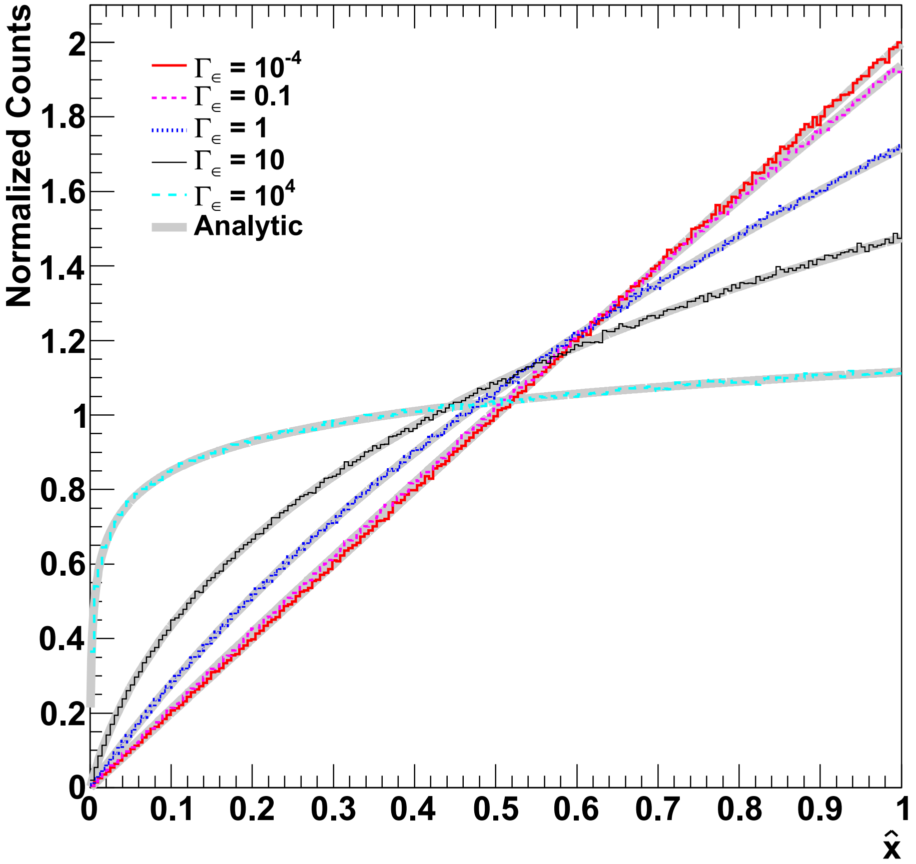

Figure 5.6: Distribution of $\hat{x}$ from inverse Compton scattering.

Jones (1968) gives the distribution of E_{max} as a function of Γ_ϵ, which appears along with the distributions from the code in Figure 5.5, again showing good agreement between the code and the analytic calculation. In the figure, electrons at 10 TeV interact with an appropriate monoenergetic background to fulfill the requested Γ_ϵ, with the case $\Gamma_\epsilon = 1$ representing interactions with the peak of the CMB.

The parameter x from Equation 2.13 is bounded by the values x_- and x_+ from Equation 2.30. We construct a value $\hat{x}$ bounded by 0 and 1 via the transformation

$$\hat{x} = \frac{x - x_-}{x_+ - x_-}. \tag{5.3}$$

Figure 5.6 shows the distribution of $\hat{x}$ from Equation 2.13 for the same simulation runs used to construct Figure 5.5. This distribution is sampled from $x\sigma_{e\gamma}(x)$, a procedure inspired by inspection of Equation 2.24. The accuracy of the distributions in $\hat{x}$ apparent in Figure 5.6 implies via Equation 2.13 that the code samples the proper distribution of angles between the electron and target photon.

In a manner similar to its treatment of the pair production interaction, after the energy and angle of the target photon are sampled, the code performs a boost to the center of mass frame in which the electron is at rest, as shown in Figure 2.6(b). The deflection angle of the photon is then sampled from Equation 2.14, the code computes the kinematics of the interaction as described in Section 2.3.1, and the resulting particles are boosted back to the lab frame. In contrast to the case of pair production, because the electron is initially at rest in the center of mass frame, azimuthal symmetry exists along the boost direction, so the azimuthal angle is unaffected by the boost and can be computed upon the return boost to the lab frame.

The distribution of target energies for a 10-TeV electron injected at a distance of 400 kpc appears in Figure 5.7, together with the expected distribution specified by the integrand of the integral over the background energy from Equation 2.24. Since the mean free path of the electrons is about 1 kpc, well below the galactic scale, the electrons are virtually guaranteed to interact. It is clear in the figure that the distributions produced by the code match our expectations very well for energies above 4×10^{-6} eV. Below this energy, the small CMB density contributes less than 0.01% of the interaction rate above 4×10^{-6} eV, so we elect to truncate the CMB distribution at this energy. Furthermore, Figure 5.8 demonstrates that the distribution of interaction lengths for the 10-TeV electrons is consistent with our estimate of 1 kpc. The analytic curve in Figure 5.8 is a decaying exponential with a characteristic length scale determined by integration of the analytic curve in Figure 5.7.

One important point evident in Figure 5.7 is that the EBL plays a role in the electrons' interactions. For 10-TeV electrons, interactions with the peak of the CMB occur at a factor $\Gamma_\epsilon \approx 1$. In this case, Equation 5.1 informs us that the maximum fraction $f_{\max}$ of the electron's energy that can be lost is $f_{\max} = 1/2$, and according to Figure 5.5 the electron is likely to lose only a small fraction of this maximum. In contrast, for interactions with the infrared peak of the EBL, occurring at $\Gamma_\epsilon \approx 10$, the electrons are likely to lose a large fraction of the maximum fraction $f_{\max} = 10/11$. Despite their rarity, interactions with the EBL can therefore limit the number of lower-energy gamma rays in the cascade, while at the same time enhancing the flux of higher-energy gamma rays. As I describe in detail in Section 5.3,

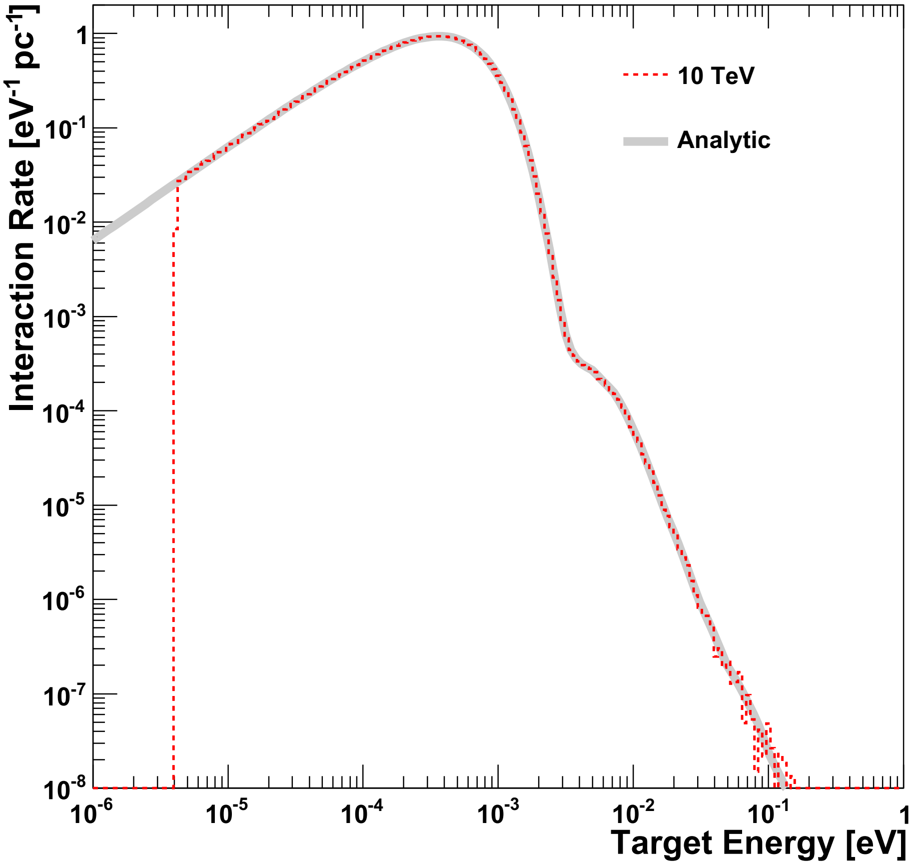

Figure 5.7: Distribution of target photon energies for inverse Compton scattering by 10-TeV electrons at nearby redshift, with analytic predictions from the inner integral of Equation 2.24. The cutoff at low energies is due to the truncated CMB model used in the code.

our code fully accounts for this effect while maintaining a relatively low processing time.

Figure 5.9 summarizes the accuracy of the Monte Carlo simulation's treatment of pair production and inverse Compton scattering. In the figure, the relative error between the total momentum before and after the interaction is plotted as a function of primary energy. Pair production events (for which the primaries are gamma rays) appear as red crosses, while inverse Compton scattering events (with electron primaries) are shown as magenta dots. We choose a range of primary energies from 1 GeV to 100 TeV for this test, injecting all of the primaries at a redshift of $z = 0.1$. The absence of pair production primaries below ~ 200 GeV arises due to the large mean free paths for gamma rays at low energies. In the case of inverse Compton scattering, the relative error is near the limit of the precision of the double

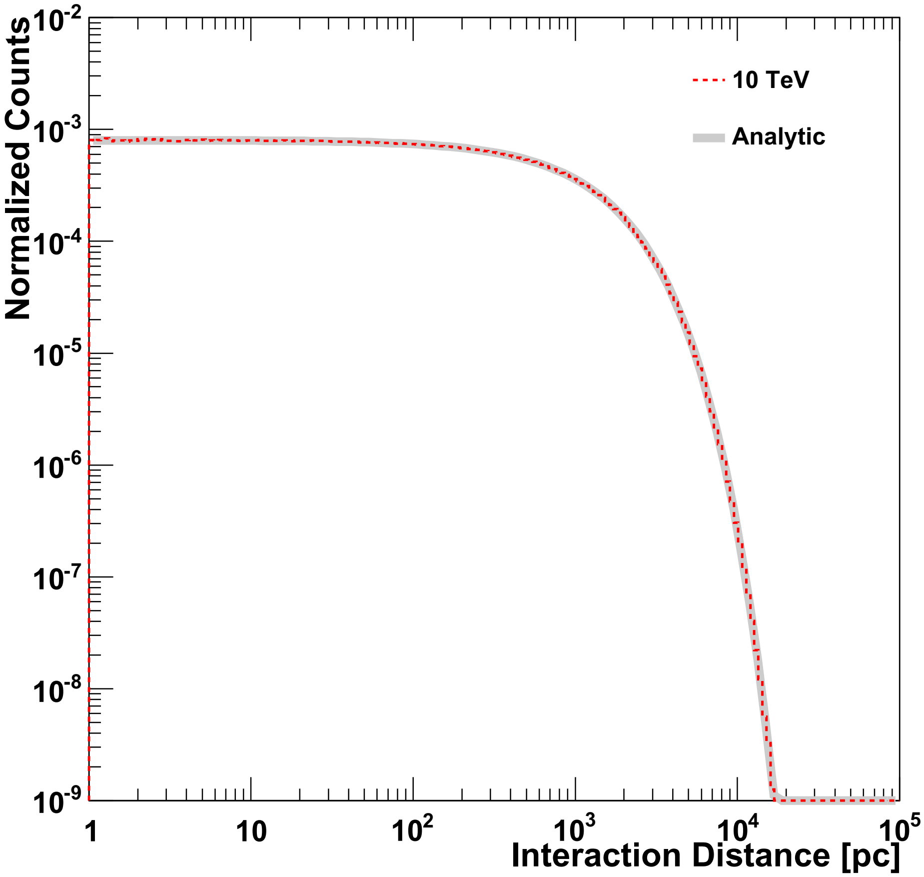

Figure 5.8: Distribution of 10-TeV electrons' interaction lengths for inverse Compton scattering.

data type of $\sim 10^{-16}$, and this causes the structure observed in the figure. The relative errors below this value are due to "accidental" cancellations in machine rounding. For pair production, the relative error is somewhat higher but still less than 10^{-10}, which is more than acceptable.

The kinematics of the cascade involves large boosts along or nearly along the direction of the primary particle. For this reason, it is important to check conservation of momentum perpendicular to the direction of the primary, in addition to total conservation of energy. Figure 5.10 shows that the code conserves this transverse momentum at an accuracy of better than 10^{-6}.

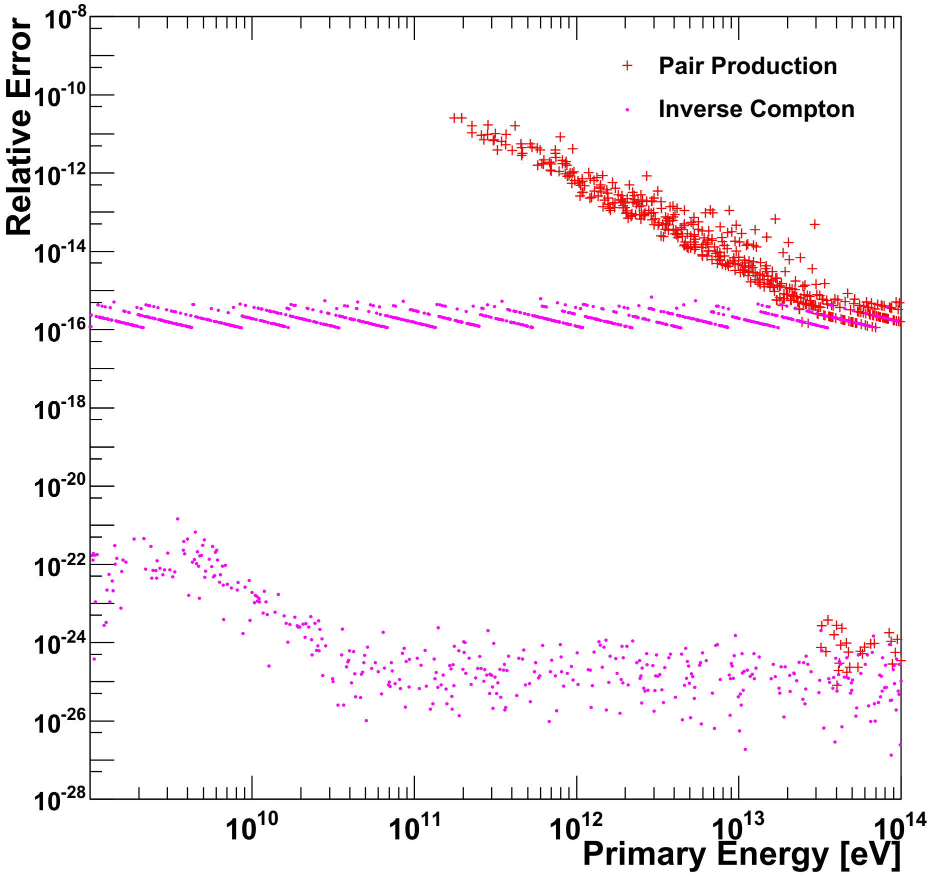

Figure 5.9: Accuracy of total momentum conservation for both pair production (red crosses) and inverse Compton (magenta dots) interactions.

5.1.3 Particle Tracking

The Monte Carlo simulation implements particle tracking by numerically integrating the equations of motion for the individual particles in an expanding three-dimensional space. We employ comoving coordinates in the particle tracking, for which physical distances can be determined by multiplying the comoving separation by the scale factor at a given redshift (Kolb & Turner, 1990). This makes the equations of motion more complicated to solve but is conceptually simpler.

A detailed derivation of the equations of motion appears in Appendix A. For a particle moving in a spatially uniform magnetic field with evolution given by Equation 1.1, the

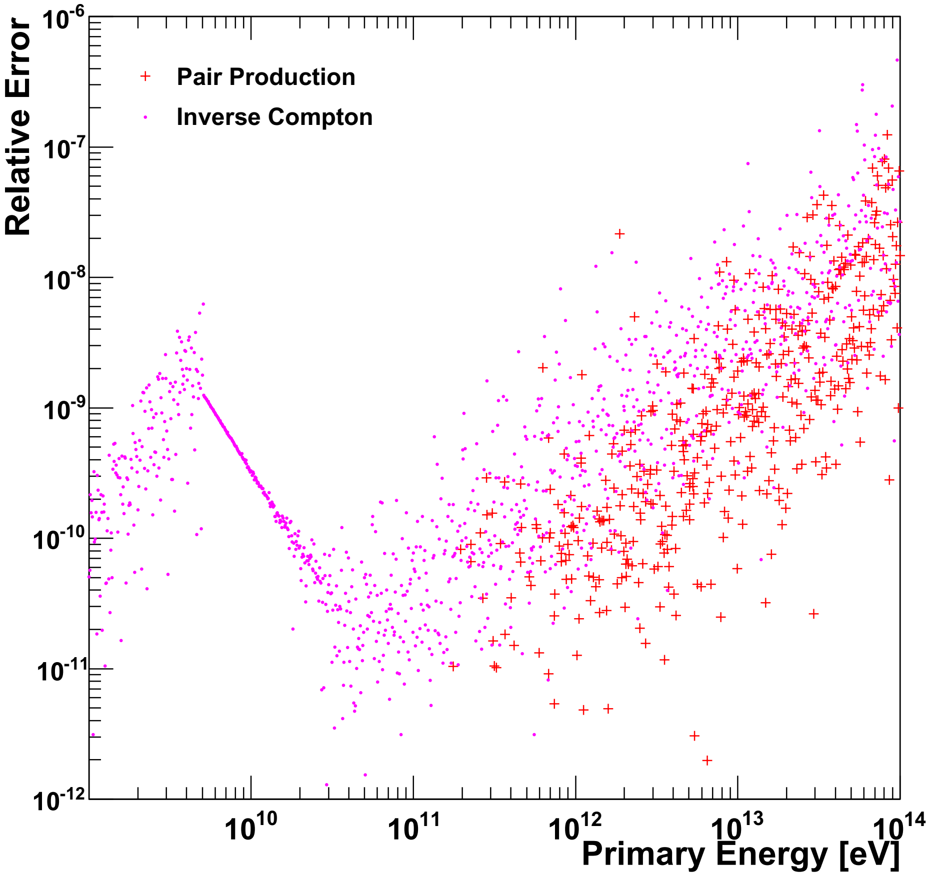

Figure 5.10: Accuracy of momentum conservation transverse to the direction of the primary, for pair production (red crosses) and inverse Compton (magenta dots) interactions. The transition in the inverse Compton error distribution at $\sim$ 5 GeV is due to the approximation of the electron speed $\beta \approx 1 - 1/2\gamma^2$.

equations of motion become

$$\frac{d}{dt}\vec{p} = -H(z)\vec{p} + \frac{q}{m\gamma}\vec{p} \times \vec{B}(z), \tag{5.4}$$

where q is the particle's charge and the second term on the right hand side vanishes for gamma rays because they do not couple to the magnetic field, at least to first order.

In the code, we implement a fourth-order Runge-Kutta method, referred to as a "stepper" in the rest of this section, to solve the differential equations of motion. The order of the stepper indicates the highest power of the step size in the expansion of the equations of motion, and the fourth-order Runge-Kutta method is particularly attractive due to the serendipitous cancellation of fourth-order terms that renders it effectively fifth-order (Butcher, 2008). We additionally employ an adaptive Richardson error correction technique, in which the error on the solution is controlled by taking two steps at step size $h/2$ for every step at step size h. While this at first appears to triple the processing time, it is actually the smaller step size that is propagated, and it has the additional benefit of automatically ensuring that the stepper runs at the optimum step size. Electrons, for instance, require a smaller step size than gamma rays, which are unaffected by the EGMF.

The code decides how far to propagate a given tracked particle by sampling the distance to its next interaction point from the mean free path. It is therefore natural to expand the equations of motion in terms of a small distance Δd instead of a small time Δt. The solution of Equation 5.4 then proceeds by stepping in small comoving distances while ensuring that the desired level of accuracy is attained.

All dynamical quantities of interest for the tracked particle, including the position, momentum, redshift, and time delay relative to a radially propagating gamma ray, are used as inputs to the Richardson error correction algorithm. If the error on any of these values is too large, then the step size is reduced and the step is repeated at the smaller step size. On the other hand, if the error on the step size is significantly smaller than the user-specified precision, the step is kept but the step size of future steps is increased in order to reduce the processing time.

We assess the accuracy of the stepper by turning off all interactions, assuming that the redshift is accurately tracked, and verifying that the position, momentum, and time delay have the expected redshift dependence. Figure 5.11 shows the evolution of the error on the momentum of electrons and gamma rays of various energies as they propagate from $z = 1$. Since the expression for the particle momentum as a function of redshift given by Equation A.15 is relatively simple, we subject the injected particles of Figure 5.11 to the code's default FLRW cosmology given by Equation A.5, for which the calculation of the momentum is analytically tractable. It is apparent in the figure that the momentum error due to propagation is very small over modest redshifts. Furthermore, because the particles are cut when they reach a specific comoving distance from the source and not when they reach a specific redshift, we see in Figure 5.11 that the nonrelativistic electrons propagate far into the future $z < 0$.

The comoving particle positions are given by Equation A.18, which is more difficult to

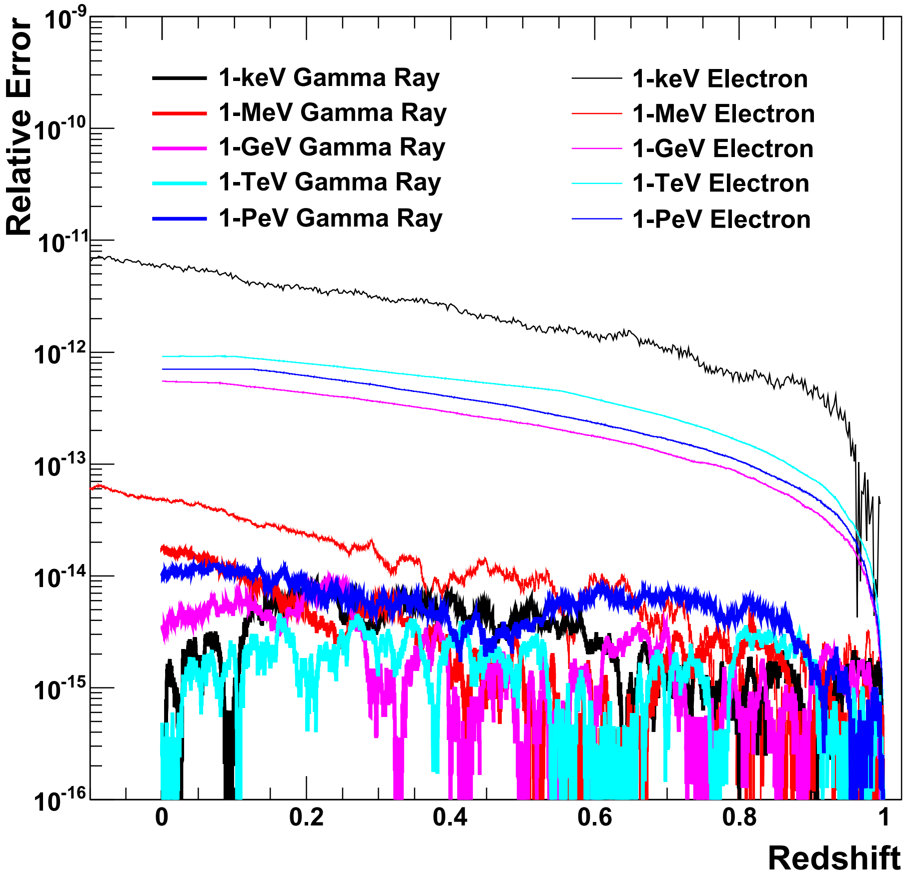

Figure 5.11: Redshift dependence of the relative error on the momentum of electrons (thin lines) and gamma rays (thick lines) of various energies injected at $z = 1$. Little variation appears in the error curves of the massless gamma rays. The electrons' curves exhibit greater variation because their mass complicates the propagation.

solve due to the $H(z)$ term. For this reason, we assume a constant-dominated cosmology for which $\Omega_\Lambda = 1$ while all other densities are zero, allowing us to use the simpler result of Equation A.19. The solution for the position as a function of redshift is then

$$x_{\mathrm{NR}}(z) = \frac{p_0 c}{2H_0 mc^2}\left[(1+z_i)^2 - (1+z)^2\right] \tag{5.5}$$

in the nonrelativistic limit $p_0/mc^2 \ll 1$ or

$$x_{\mathrm{HR}}(z) = \frac{c}{H_0}\left[(z_i - z) - \frac{(mc^2)^2}{2q{p_0}^2}\left(\frac{1}{1+z_i} - \frac{1}{1+z}\right)\right] \tag{5.6}$$

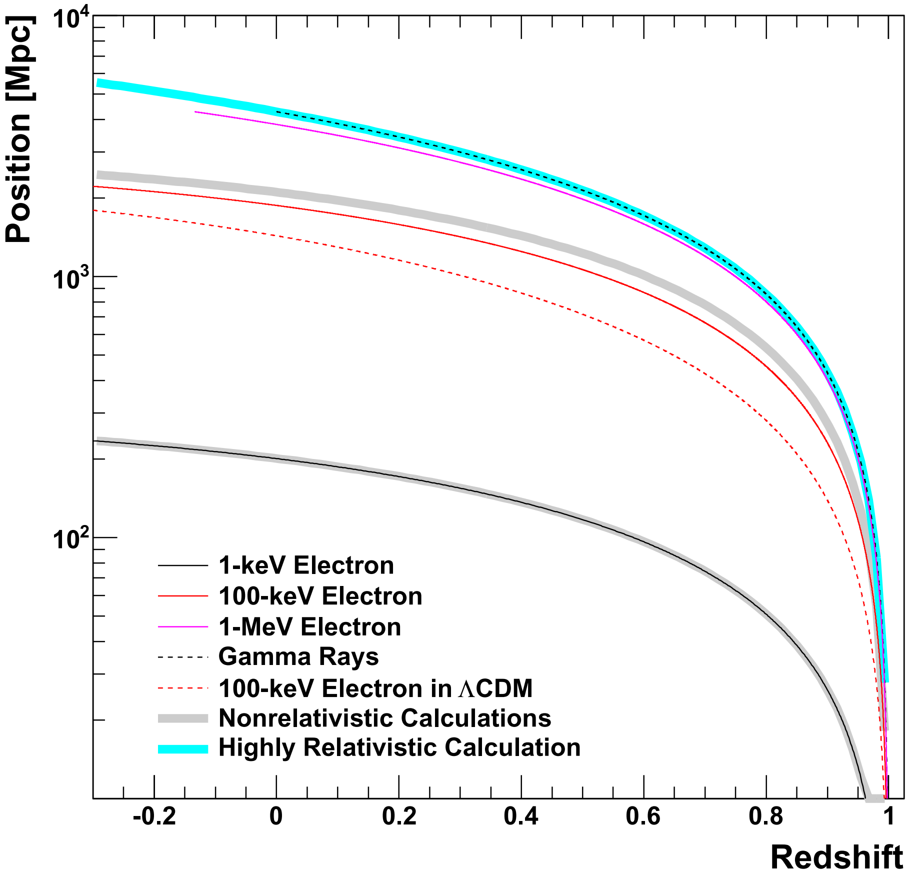

Figure 5.12: Comoving distance as a function of redshift for particles of various energies in a constant-dominated cosmology. A 100-keV electron in a ΛCDM cosmology is also shown for comparison.

in the highly relativistic limit $p_0/mc^2 \gg 1$. In these equations, the momentum of the particle at the present day is p_0, and z_i is the initial redshift of the particle. Figure 5.12 shows the redshift evolution of the comoving distance for various particles. At 1 keV, the predictions from the nonrelativistic approximation of Equation 5.5 agree well with the propagated particles in the code, while at 100 keV there is evident divergence. Also as expected, the propagation of gamma rays matches the highly relativistic prediction of Equation 5.6, and the marginally relativistic electrons at 1 MeV follow nearly the same evolution as the gamma rays.

Figure 5.13 shows the error on the time delay of electrons with kinetic energies from 5 keV to 28 GeV propagating a distance of 4283 Mpc. The nonrelativistic approximation from

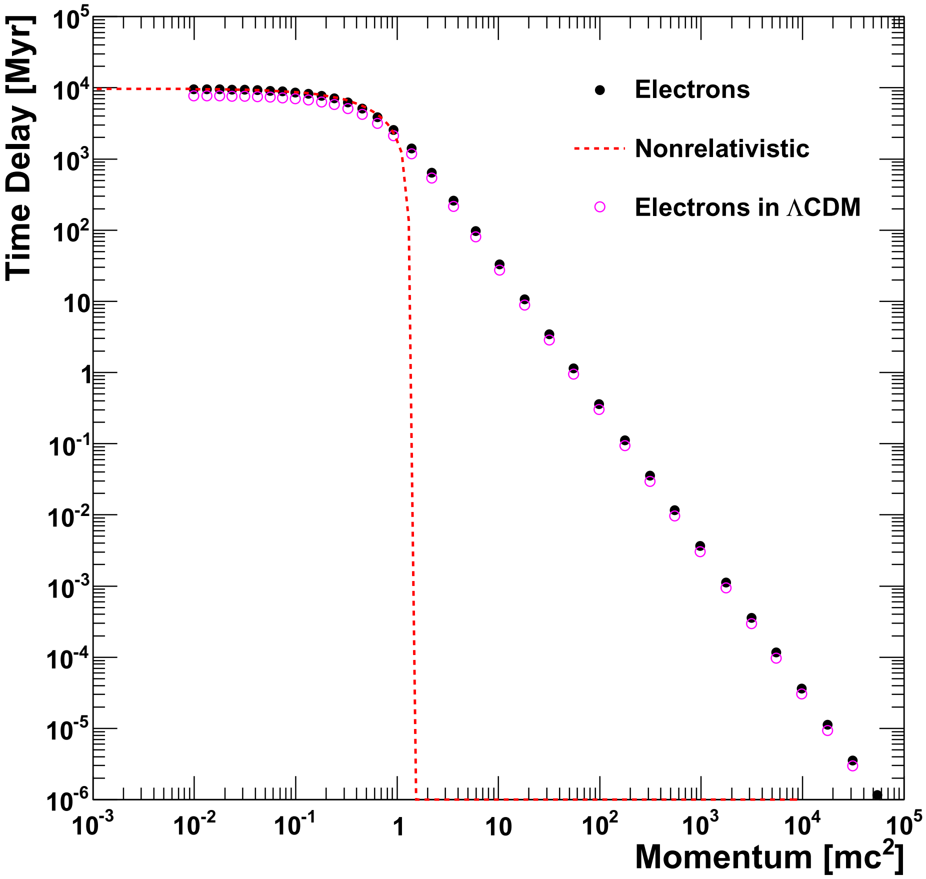

Figure 5.13: Time delay of electrons of various energies propagating from $z = 1$ to $z = 0$, with respect to the propagation time of a gamma ray.

Equation A.31 matches the simulation results for low energies.

5.1.4 Energy Losses

Particles continuously lose energy due to redshift during their propagation. To facilitate computation, the code can also enter a mode of propagation in which the interactions of electrons and positrons with the CMB are modeled as a continuous energy loss process. This mode is triggered in the extreme Thomson limit when it is impossible for electrons to produce observable secondary gamma rays from CMB interactions but the production of observable secondaries from the EBL is still possible. I discuss this mode in greater detail in Section 5.3.1. In both cases, energy losses affect the mean free path of the particle in a continuous manner throughout its propagation, and simple sampling of the interaction

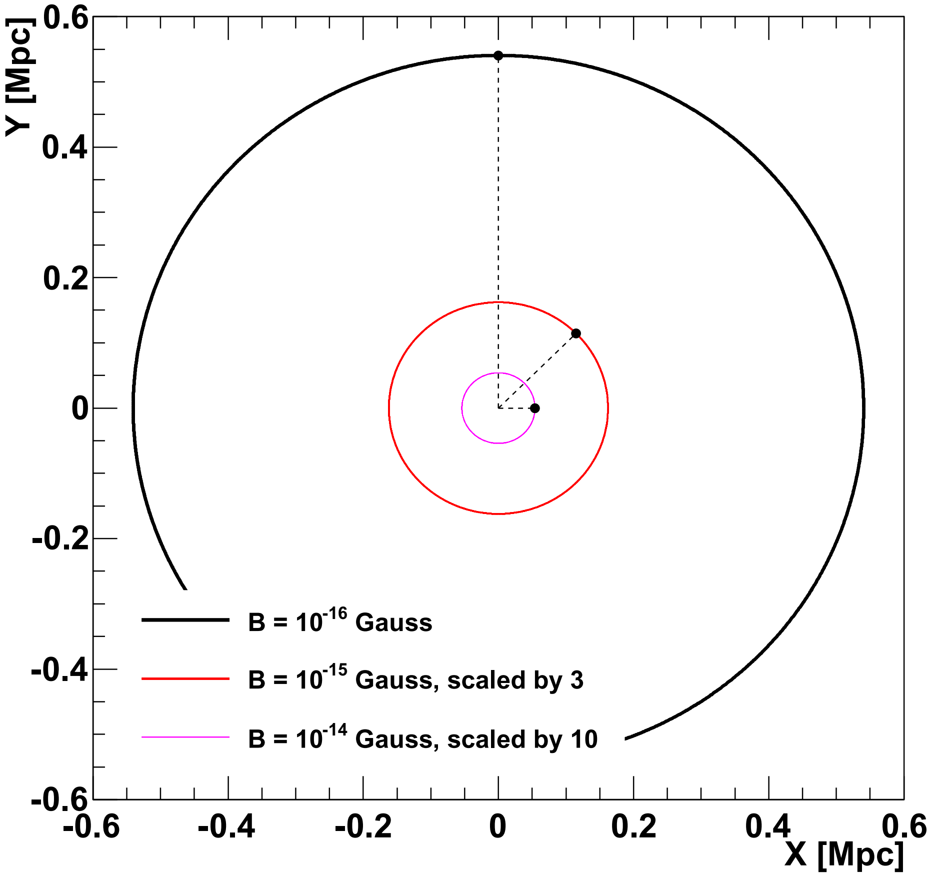

Figure 5.14: Paths of 100-GeV electrons in comoving coordinates. A constant, uniform field exists perpendicular to the circular trajectories. The radii for the stronger field strengths are scaled by 3 and 10 to better fit on the plot. Dashed lines ending in filled circles indicate the expected radius from Equation 5.4.

length from the mean free path is no longer valid.

Our solution is to sample the interaction length not from the mean free path of the particle at its initial energy, but rather from the minimum mean free path along its entire potential trajectory. After propagating the particle this sampled distance, we accept the interaction with a probability $\lambda_0/\lambda(L+L_1)$, where λ_0 is the minimum mean free path, $\lambda(L)$ is the mean free path as a function of the length along the trajectory, and the particle is propagating from distance L_1 to L. The justification for this procedure appears in Appendix B.

5.1.5 Magnetic Fields

In Euclidean space, in the presence of a magnetic field, an electron of constant energy follows a spiral trajectory with Larmor radius given by Equation 2.31. In an expanding space, the electron's trajectory remains spiral with the same radius in comoving coordinates. This is apparent from Equation 5.4 and can be thought of as follows: the field strength evolves as $(1+z)^2$ according to Equation 1.1, while the electron's momentum evolves as $(1+z)$. Equation 2.31 then tells us that the Larmor radius in real coordinates evolves as $(1+z)^{-1}$, at the same rate as the expansion, implying that the radius of the spiral trajectory in comoving coordinates does not change. Figure 5.14 demonstrates that the code reproduces our expectations from these calculations.

Stronger magnetic field strengths cause greater deflections of the electrons and positrons, resulting in a smaller required step size to maintain the desired level of accuracy. The processing time due to the smaller step size for EGMF strengths above $\sim 10^{-15}$ Gauss can become prohibitively expensive. To combat this, we implement a cut that removes electrons once their trajectories have been deflected by an angle of more than $\pi/2$ from the direction of the primary gamma ray. Such electrons are equally likely to produce a secondary gamma ray in any direction, so their contribution to the cascade is indistinguishable from the isotropic diffuse gamma-ray flux and can be safely ignored.

5.1.6 Multigenerational Cascades

The presence of significant gamma-ray flux above 10 TeV in the intrinsic spectrum can lead to multigenerational cascades, in which the secondary gamma rays can themselves undergo pair production interactions and produce upscattering electrons and positrons. These multigenerational cascades are ignored in the semi-analytic model described in Chapter 4. While it is possible to include the effects of multigenerational cascades in certain models, such as the model of Ahlers (2011), such models have their own limitations that a Monte Carlo simulation can straightforwardly overcome[3]. Figure 5.15 demonstrates the ability of the code to model multigenerational cascades. It is clear that at least second-generation gamma rays can be important in the 1-GeV to 10-GeV energy range if the intrinsic spectrum has substantial flux at 20 TeV.

---

[3] For instance, Ahlers (2011) makes the assumption that the gamma-ray source emits isotropically.

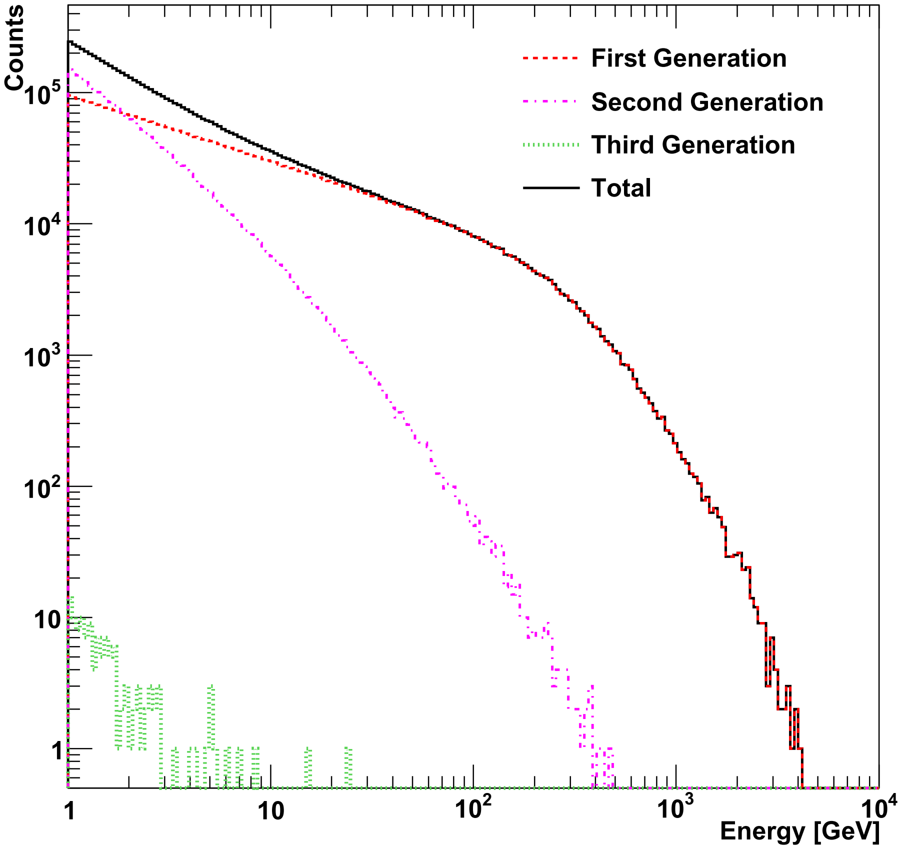

Figure 5.15: Distribution of secondary gamma rays from 5000 20-TeV primaries injected at $z = 0.13$, separated by generation in the cascade.

5.2 Analysis and Interpretation

With the accuracy of the simulation in terms of fundamental physics processes and particle tracking reasonably verified, we move on to the interpretation of the results.

5.2.1 Geometry

In a standard run of the simulation, a primary gamma ray with a known energy is injected at a given redshift. The code tracks the resulting cascade and records the properties of all gamma rays that arrive on the surface of a sphere centered on the injection point and whose radius in comoving coordinates is equal to the distance between Earth and the source.

If we assume Earth to be at a fixed location in the comoving propagation space, the

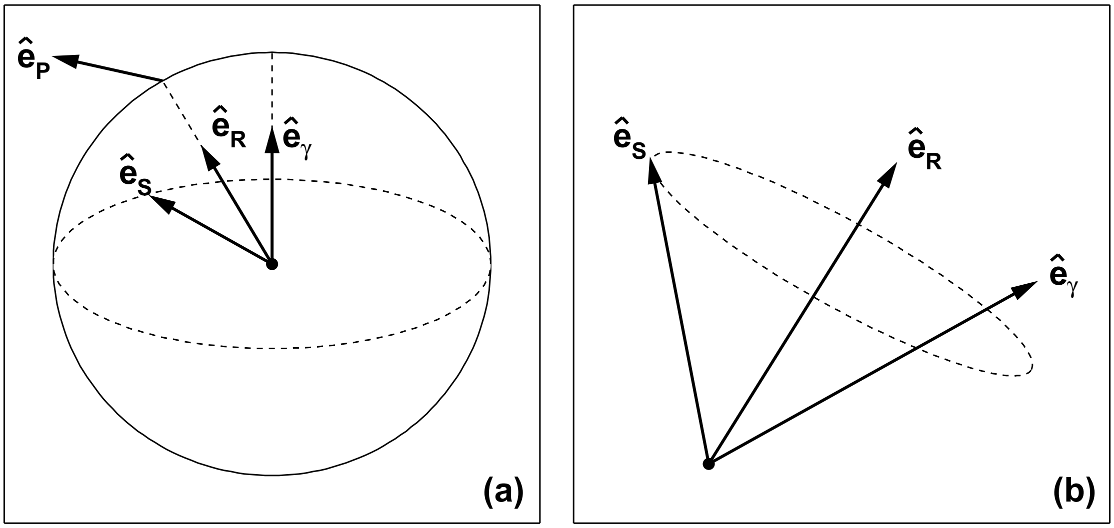

Figure 5.16: Geometry relevant to the interpretation of the cascade. Panel (a) shows the four vectors discussed in the text, while Panel (b) demonstrates that the freedom to rotate the source axis of symmetry $\hat{e}_S$ around the line of sight $\hat{e}_R$ changes the angle θ_S between the primary gamma ray's direction and the source axis.

chances that any particular gamma ray would intercept it are vanishingly small. Instead, we treat each gamma ray's arrival as a separate event, assuming that Earth is located at the exact crossing point of the gamma ray on the sphere. An appropriate rotation of the space around the direction from the source to Earth fixes the geometry. There are four directional vectors relevant to this geometry, and they appear in Figure 5.16(a), in which $\hat{e}_R$ is the line of sight from the source to the observer, $\hat{e}_\gamma$ is the emission direction of the primary gamma ray, $\hat{e}_P$ is the direction of the observed secondary gamma ray, and $\hat{e}_S$ is the source axis of symmetry, the axis of the blazar jet.

We can fix the positions of the source and observer by fixing the vector $\hat{e}_R$, which is the vector normal to the point on the sphere at which the gamma ray is observed. The physics of the cascade gives us the arrival direction $\hat{e}_P$, and from these two vectors we deduce the arrival angle θ_A, which is given by

$$\hat{e}_R \cdot \hat{e}_P = \cos\theta_A. \tag{5.7}$$

The angle between $\hat{e}_\gamma$ and $\hat{e}_R$ is also set by the physics of the cascade, while the angle between $\hat{e}_S$ and $\hat{e}_R$ is set by the orientation of the blazar in real space. However, in principle, any angle θ_S between the jet axis $\hat{e}_S$ and the momentum of the primary $\hat{e}_\gamma$ is admissible, so we have the freedom to rotate $\hat{e}_S$ around $\hat{e}_R$, as shown in Figure 5.16(b). This operation obviously changes the value of θ_S and consequently changes the weight from the intrinsic blazar spectrum as given by Equation 3.1. Denoting the azimuthal angle by which the vector $\hat{e}_S$ is rotated out of the $\hat{e}_\gamma$-$\hat{e}_R$ plane as ϕ_R, we see from straightforward geometry that

$$\cos\theta_S = \cos\theta\cos\theta_V + \sin\theta\sin\theta_V\cos\phi_R, \tag{5.8}$$

where θ_V is the viewing angle of the blazar (the angle between $\hat{e}_R$ and $\hat{e}_S$), and θ is the deflection angle of the secondary gamma ray relative to the primary (the angle between $\hat{e}_R$ and $\hat{e}_\gamma$). This geometry is of course important only for a blazar whose jet axis is not aligned with the line of sight. In this general case, we sample ϕ_R uniformly on $[-\pi, \pi)$ for each secondary gamma ray to construct the observed flux. We then employ Equation 3.1 to get the weight factor for the gamma ray.

5.2.2 The Cascade Flux

The computation of the flux from the cascade proceeds in two stages. In the first, the secondary photons are collected and weighted by the flux from Equation 3.1 based on the energy of the primary gamma ray that created their cascade and the randomly sampled angle ϕ_R as discussed in the previous section. The weights are normalized such that the total flux

$$F_{\text{tot}} \equiv F_0 \frac{dN}{d\Omega dt dE} \tag{5.9}$$

fulfills the equation

$$\int d\Omega \int dt \int dE F_{\text{tot}} = 1, \tag{5.10}$$

where Ω is the solid angle, E is the energy, and t is the time of arrival. The variable t can be written in terms of the time delay ΔT accrued during propagation and the time of primary emission at the source τ as

$$t = \Delta T + (1+z)\tau, \tag{5.11}$$

in which the redshift of the source appears because time differences at the source are magnified by the expansion of space during the time interval. Any generic time profile for the

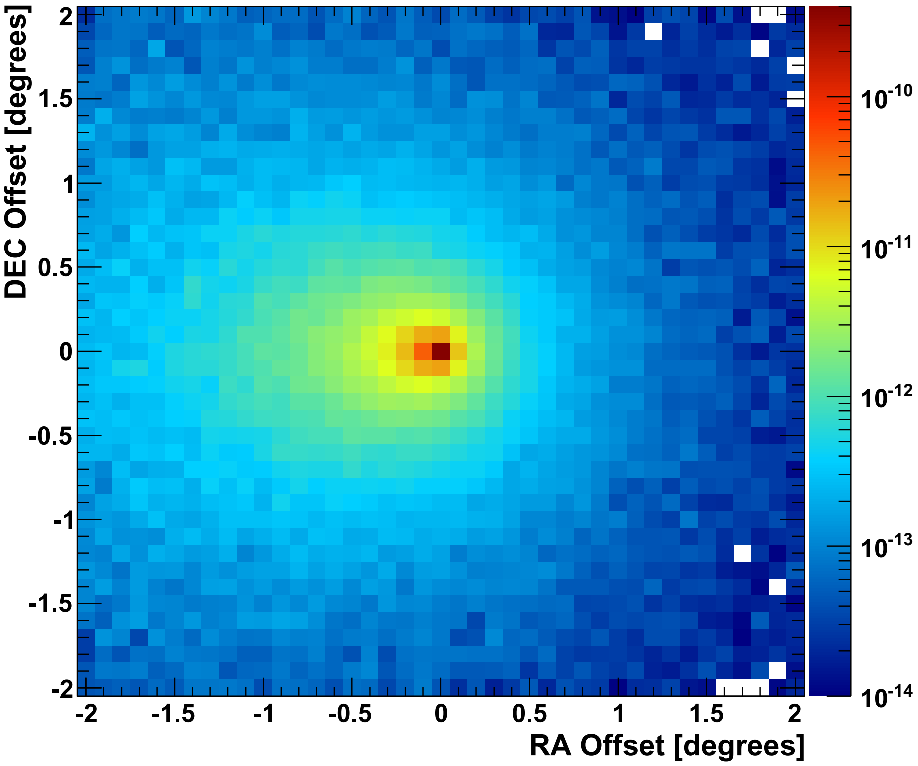

Figure 5.17: Simulated sky map in units of gamma rays cm^{-2} s^{-1} sr^{-1} for the cascade emission from a blazar with an intrinsic spectral index 1.5, cutoff energy 10 TeV, redshift 0.13, and misalignment angle of 5°, with an EGMF strength of 10^{-15} Gauss. The misalignment angle is chosen to lie along the right ascension (RA) axis, in the negative direction, as is evident in the map.

source can be specified, though the analyses presented in this work assume a constant flux independent of time. There is also an option to include an instrument PSF at this stage, which allows us to investigate instrumental effects.

The second stage of the analysis involves generating distributions subject to certain cuts. In general, the distributions to be constructed depend on the specific physics goals of the analysis. For example, the spectrum of gamma rays within a certain angular separation from the source may be of interest, or a sky map of the cascade within a certain energy band may be constructed. These distributions are weighted based on the weights calculated in the first stage. A sample sky map of the cascade constructed from the simulation of a blazar with a misalignment angle of $\theta_V = 5°$ appears in Figure 5.17. I plot the spectrum of the various flux components in Figure 5.18. The "direct" emission in Figure 5.18 is the

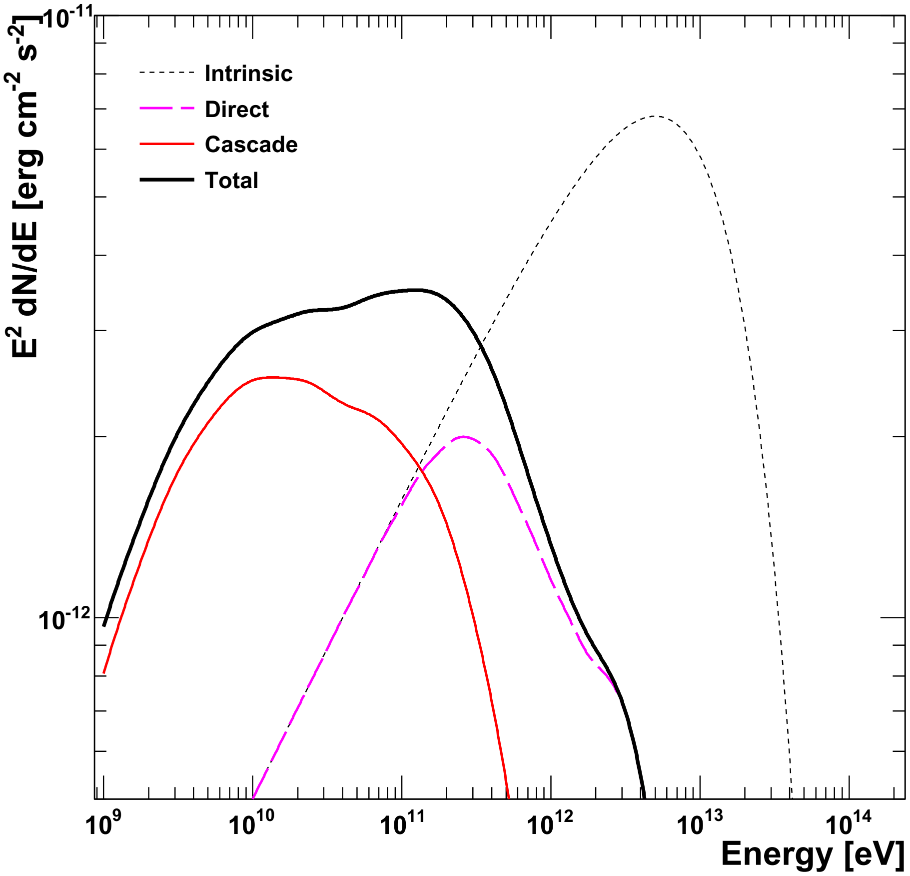

Figure 5.18: Simulated spectrum of the cascade emission from Figure 5.17. The energy lost due to attenuation of the intrinsic spectrum produces the flux in the cascade, highlighting the role of the photon backgrounds in converting TeV-scale gamma rays into GeV-scale gamma rays.

remaining pointlike flux from the blazar after the intrinsic emission has interacted with the EBL. The "cascade" emission in the figure results from the reprocessed intrinsic flux that forms the extended halo of Figure 5.17. Observations of the "total" flux, which is the sum of the cascade and direct, may reveal information about the cascade if the field is sufficiently strong. If the field is weak, then for this particular intrinsic spectrum the observed total flux in the the GeV energy band will be dominated by the cascade gamma rays.

Injection Energy	No Transition Energy	300-GeV Transition Energy
1 TeV	156 s	1.85 s
10 TeV	351 s	61.4 s
100 TeV	5050 s	572 s

Table 5.1: Processing times with and without a transition energy of 300 GeV for cascades of various energies. The energy cut is 8.66 GeV.

5.3 Adequate Statistics

One must find a balance between the processing time for a set of simulations and the accuracy resulting from that set. We have devised a generic procedure to ensure the accuracy of our results. In this section, I present the specific realization of this procedure used in the analyses of Chapter 6, but the details such as the energy binning and the desired accuracy can easily be modified for a particular application.

We restrict our attention in this section and throughout the following chapter to gamma rays with energies greater than 866 MeV, which we define to be "observable." This energy is selected because it is the low edge of an energy bin centered at 1 GeV when the energy is binned with eight bins per decade and spaced evenly in logarithmic space. I present the reasoning behind this selection in Section 5.3.2.

5.3.1 The Transition Energy

As shown in Section 2.4.2, the dominant interaction channel for the inverse Compton process is via interactions with the CMB. As the electrons cool, the upscattered gamma rays tend to be produced with smaller energies until the maximum possible energy from Equation 2.18 is less than our "observable" energy of 866 MeV. At this point, CMB interactions are irrelevant, but it is still possible for EBL interactions to produce observable secondaries. Terminating the electron tracking at this stage could therefore lead to an inaccurately low prediction for the observable flux.

However, when the CMB interactions are treated as a discrete process, the code spends a significant portion of its time propagating the electrons between the interaction points. A better method would be to include the CMB losses as a continuous process and allow the stepper to optimize the propagation between EBL interactions, which according to Figure 2.11 occur at distances 300 times larger than the CMB interactions. We therefore select a transition energy E_T at which the treatment of the CMB interactions is converted from a discrete to a continuous process. Table 5.3.1 shows the simulation processing times for cascades initiated by primary gamma rays with energies between 1 TeV and 100 TeV at a redshift of 0.13, for the case of no transition energy and again for the case of $E_T = 300$ GeV. Obviously, to reduce the processing time as much as possible, we should select the highest possible transition energy consistent with a given desired accuracy.

Two concerns arise in setting the transition energy. First, the distribution of energies along the electron's trajectory should be the same, independent of the transition energy. Otherwise, the distribution of upscattered EBL photons would be different between the "correct" case of no transition energy and the "simplified" case in which a transition energy is used. If the transition energy is within the Thomson limit for CMB interactions, we expect that the continuous energy losses will accurately reflect the losses due to discrete interactions. However, once the Thomson limit assumption is violated, then the continuous energy loss process will lose energy too rapidly in comparison to the true Klein-Nishina rate, which is due to discrete events, and the distribution of energies along the electron's trajectory will change. Figure 5.19 shows the relative error, compared to simulation runs with no transition energy, as a function of energy for four different values of the transition energy. In the figure, the dips at the transition energy are due to the sampling of the trajectories at discrete step sizes and do not represent a true deviation from the distribution without a transition energy. However, at energies above 600 TeV, significant real deviations appear below the transition energy. We therefore assume that transition energies below ~ 600 TeV accurately model the distribution of upscattered EBL energies.

The second concern in setting the transition energy is that interactions with the CMB should be negligible below E_T. That is, CMB interactions below the transition energy should not be able to produce observable gamma rays. In the most conservative case, if the maximum CMB photon energy is ϵ_{max}, then by Equation 2.18 we can set a transition energy of

$$E_T = \sqrt{\frac{E_{\text{obs}}}{4\epsilon_{\text{max}}}} mc^2, \tag{5.12}$$

where E_{obs} is the energy above which secondary photons are defined to be observable. Below

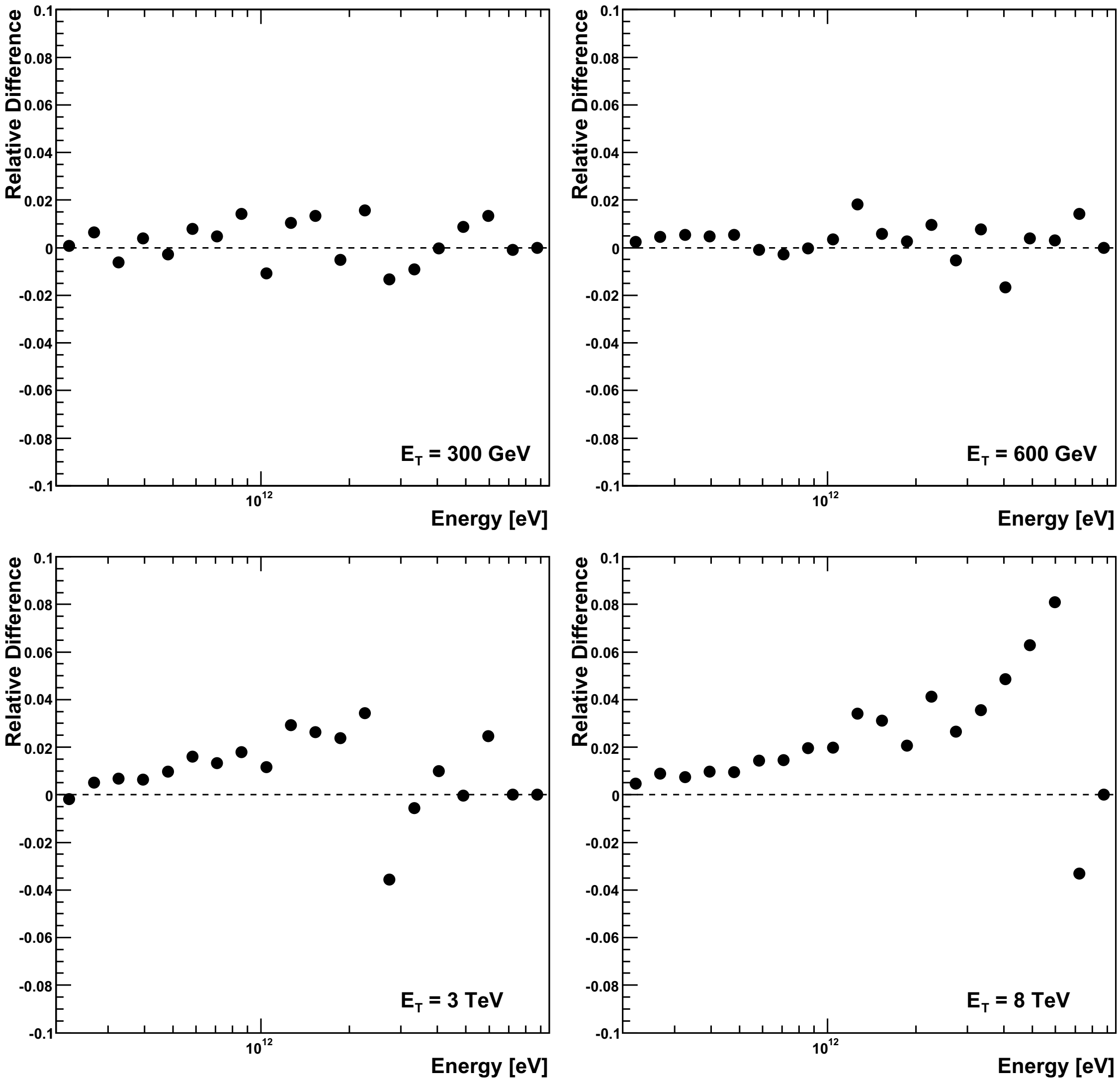

Figure 5.19: Errors on the electron energy distributions for various transition energies. The source redshift is 0.13.

this value of E_T, it is impossible for the electron to upscatter the CMB photon to an energy greater than E_{obs}.

We can be slightly less conservative by lowering the value of ϵ_{max} until the CMB density is some fraction of the total EBL density. Since we have assumed the Thomson limit, in which the cross section is independent of the target photon energy, only the total number density matters in the computation of the interaction rate. Defining a 1% loss of secondary photons as acceptable, we can find an expression for ϵ_{max}, and thereby E_T via Equation 5.12,

Redshift	**EBL Density**	**CMB Density**	ϵ_{max}
0	1.5 cm^{-3}	411 cm^{-3}	3.5 meV
0.2	2.3 cm^{-3}	715 cm^{-3}	2.9 meV
0.4	3.5 cm^{-3}	1140 cm^{-3}	2.5 meV
0.6	4.9 cm^{-3}	1690 cm^{-3}	2.2 meV
0.8	5.9 cm^{-3}	2410 cm^{-3}	2.0 meV
1	6.8 cm^{-3}	3310 cm^{-3}	2.0 meV

Table 5.2: CMB and EBL densities, along with ϵ_{max} as defined by Equation 5.13, at specific redshifts. The energy ϵ_{max} decreases with increasing redshift because the CMB evolves more rapidly than the EBL.

by demanding that

$$\int_{\epsilon_{\mathrm{max}}}^{\infty} dE \frac{dn_{\mathrm{CMB}}}{dE} = \frac{n_{\mathrm{EBL}}}{100}, \tag{5.13}$$

where n is a number density. Table 5.3.1 shows some values of the CMB and EBL densities at specific redshifts, along with the corresponding value of ϵ_{max}. It is clear from the table that, out to a redshift of $z \approx 1$, a value of $\epsilon_{\mathrm{max}} = 3.5$ meV yields an acceptable level of accuracy. According to Table 5.3.1, this procedure can speed up the code by as much as two orders of magnitude, depending on the energy of the primary gamma ray.

5.3.2 The Transfer Function

In practice, we simulate primary gamma rays at a number of discrete energies with equal logarithmic spacing from 1 GeV to 133 TeV. We then define a number of energy bins for the observed cascade photons, typically logarithmic with the same spacing as the primary gamma rays, centered on the primary gamma-ray energies. If we denote the primary energies by E_i and the cascade bin centered on E_i by b_i, then we seek the function $T_{i,j}$ representing the effect of the cascade in converting an individual primary at energy E_j into a number $T_{i,j}$ of cascade gamma rays in bin b_i. We refer to $T_{i,j}$ as the transfer function and note in general that $T_{i>j,j} = 0$ (primary gamma rays do not produce secondaries with energies greater than their own) and

$$\sum_i T_{i,j} \geq 0. \tag{5.14}$$

That is, particle number is not necessarily conserved in the cascade process. The only restriction on the number of cascade particles that a given primary can produce arises due to conservation of energy. For the trivial case in which the primary gamma ray survives propagation from the source to the observer, $T_{i,j} = \delta_{ij}$.

If $T_{i,j}$ is measured extremely well, we can apply it to any intrinsic source spectrum to determine the observable cascade. The task, then, is to determine $T_{i,j}$ to a given accuracy, after which it can be applied to any intrinsic spectrum that we wish to model. We expect the number of particles in a bin to follow Poisson statistics, so that if a relative accuracy of p is desired, then we can simply run the simulation until

$$(N_j T_{i,j})^{-1/2} \leq p, \tag{5.15}$$

where N_j is the total number of primary gamma rays injected at energy E_j. In this optimal case, the cascade resulting from any intrinsic spectrum that changes slowly over the width of a bin will be modeled at an accuracy of at least p, and in most cases the overall accuracy will be much better because multiple primary energy bins will contribute to a single cascade energy bin. In practice, however, the transfer function can be quite small for bins that are near the energy of the primary gamma ray and a prohibitive number of injections N_j may be required. For these cases, we assume that if $T_{i,j} < 10^{-2}$ at greater than 99.9% confidence then it is close enough to zero to be irrelevant. The confidence level can be evaluated by treating the appearance of a gamma ray in the bin as a binomial process since, by assumption, the probability for it to occur is very small.

One other assumption is required to reduce the simulation processing time to acceptable levels. If E_j is the lowest primary energy for which we cannot assume that $T_{i,j} < 10^{-2}$ at greater than 99.9% confidence for bin b_i, then for this bin we run the simulation not until Equation 5.15 is fulfilled, but rather until

$$\left[T_{i,j}\left(\frac{N_j + N_{j+1} + N_{j+2}}{3}\right)\right]^{-1/2} \leq p. \tag{5.16}$$

This procedure increases the size of the region of the intrinsic spectrum responsible for the contents of bin b_i exactly at the energy where the transfer function "turns on." It is accurate as long as the intrinsic spectrum does not change dramatically over three bins. Motivated by this, we select a bin size such that there are eight bins per decade in energy, acknowledging that any features on sub-decade energy scales in the intrinsic spectrum will not be resolvable with our method. In effect, we are trading accuracy for speed in an acceptably small region of our intrinsic spectrum.

Finally, it is possible in some bins for a single cascade to fulfill the requirement given by Equation 5.15. In order to reduce our dependence on the properties of individual cascades, we demand that at least 32 separate primary injections are run for the determination of each $T_{i,j}$.

5.3.3 Overall Accuracy

Although the procedure for constructing the transfer function focuses on the accuracy of the spectrum of the cascade, the simulation produces additional information, for example on the angular extent and time delay of the cascade. We do not verify the accuracy of this information directly. However, we expect both the angular extent and time delay to be related to the energy spectrum because higher energy gamma rays tend to be produced by higher energy electrons that have interacted less with the EGMF, resulting in smaller angular extents and time delays. Thus, our procedure of establishing a certain level of accuracy on the spectrum will translate directly into a similar level of accuracy on other properties of the cascade. Furthermore, the current generation of gamma ray telescopes can measure fluxes to roughly 20% accuracy (Aharonian et al., 2006). By demanding an accuracy of $p = 0.02$ for the simulation's predictions, we ensure that we are well below the experimental uncertainties.

5.4 General Predictions

In this last section, I turn to a few general predictions from the Monte Carlo simulation. I choose a fiducial blazar at a redshift of $z = 0.13$ with a bulk Lorentz boost factor of $\Gamma = 10$ and a lifetime at least as long as the time taken by the cascade to reach a steady state. To normalize the simulation results presented in this section, I have fit them to the VERITAS data on the blazar RGB J0710+591.

5.4.1 Spectra

Figure 5.20, which shows the intrinsic, direct, cascade, and total spectra for three different intrinsic source spectrum models, highlights the role of the cascade in reprocessing gamma rays at the TeV scale into flux at the GeV scale. In the figure, I fit the VERITAS data for RGB J0710+591 to the total observed spectrum when the intrinsic spectrum is a power law with a spectral index of 1.5. The three panels show the results for intrinsic cutoff energies of 3, 10, and 30 TeV. Although the VERITAS data can be made to fit these three models reasonably well through an appropriate choice of the total luminosity, they produce very different amounts of cascade in the energy range accessible to the *Fermi* LAT.

The general trend of increasing cascade emission with enhanced flux above 1 TeV is evident in Figure 5.20. This effect can be accomplished under the assumption of an intrinsic power-law spectrum with an exponential cutoff either by increasing the cutoff energy or by hardening the spectral index. It is therefore essential to seek blazar targets that are well detected at multi-TeV energies. Unlike previous studies focusing exclusively on the spectral information, searching for the halo emission does not require the blazar to be weakly detected in the GeV energy range. Rather, an abundance of photons in the *Fermi* observations will better constrain the existence and extension of the halo, improving the detection of or limit on the EGMF.

Finally, Figure 5.20 predicts a spectral softening of the *Fermi* observations relative to the measurements by the IACTs. The degree of softening and the energy at which it begins depend on the flux of the cascade, and therefore depend indirectly on the EGMF. However, to use this softening as a signature of the EGMF is difficult because the blazar may have additional components that are not well modeled by a power law. I neglect this possibility in this chapter and the next.

5.4.2 Energy-Dependent Morphology

In Chapter 4, I focused on accessing primarily the spectral information available in the cascade, using the halo extent only to determine the flux of gamma rays within the 68% containment radius of the *Fermi* LAT. Using the simulation, we can investigate the additional information available in the energy-dependent morphology of the cascade. Figure 5.21 shows how the appearance of the halo changes, for instance, as the EGMF strength increases from

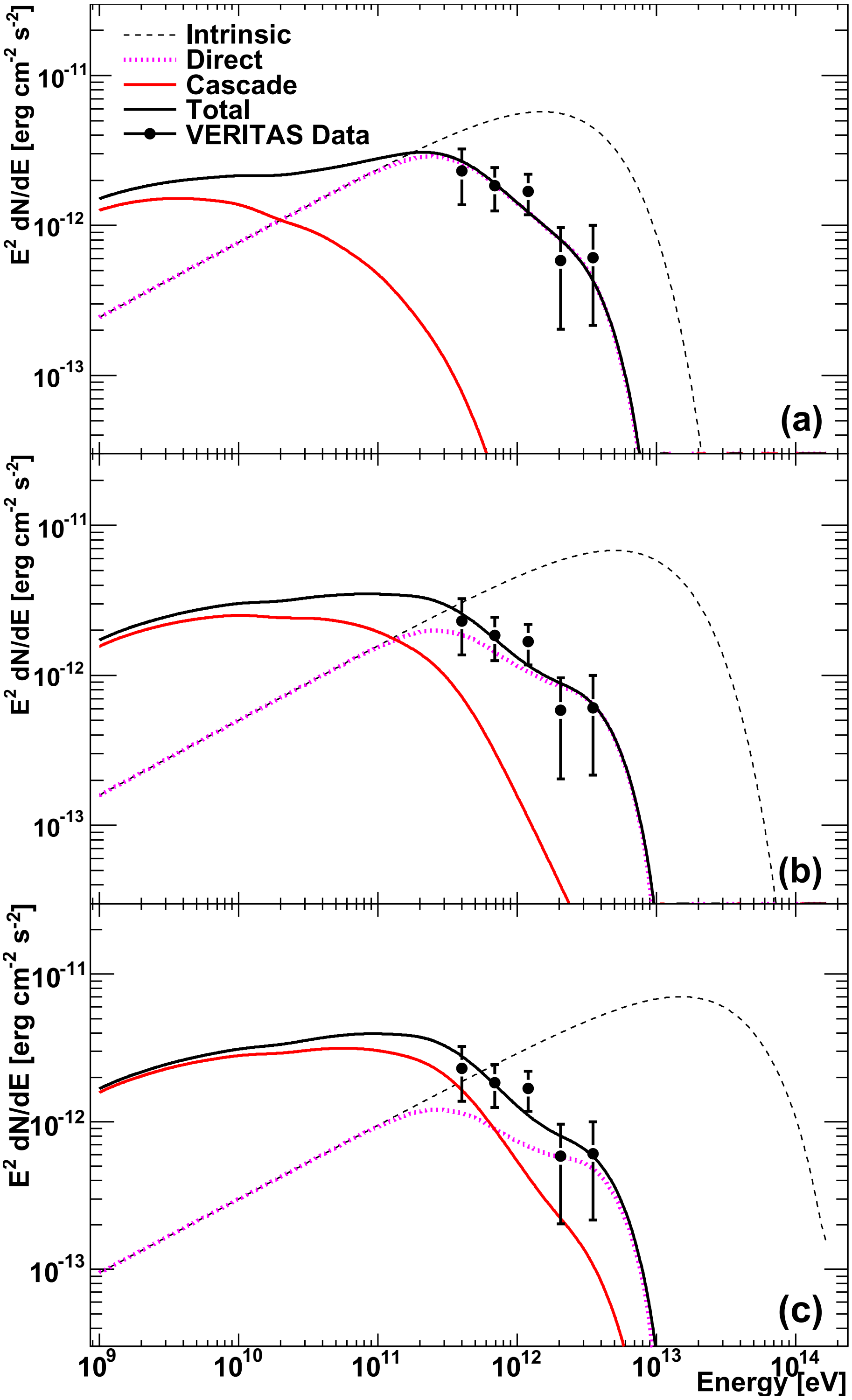

Figure 5.20: Spectra for a source at $z = 0.13$ with an intrinsic spectral index of 1.5. The cutoff energy is (a) 3 TeV, (b) 10 TeV, and (c) 30 TeV.

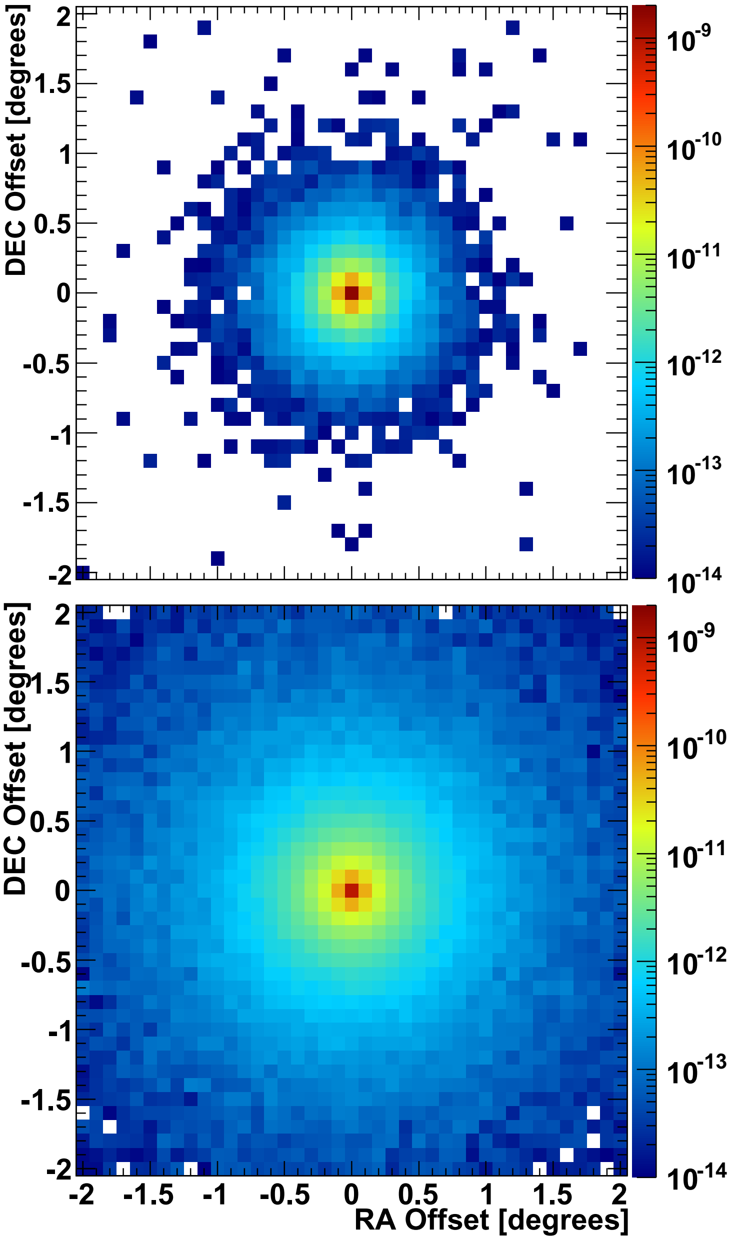

Figure 5.21: Extended halo emission for an EGMF strength of $B = 10^{-17}$ Gauss (top) and $B = 10^{-16}$ Gauss (bottom).

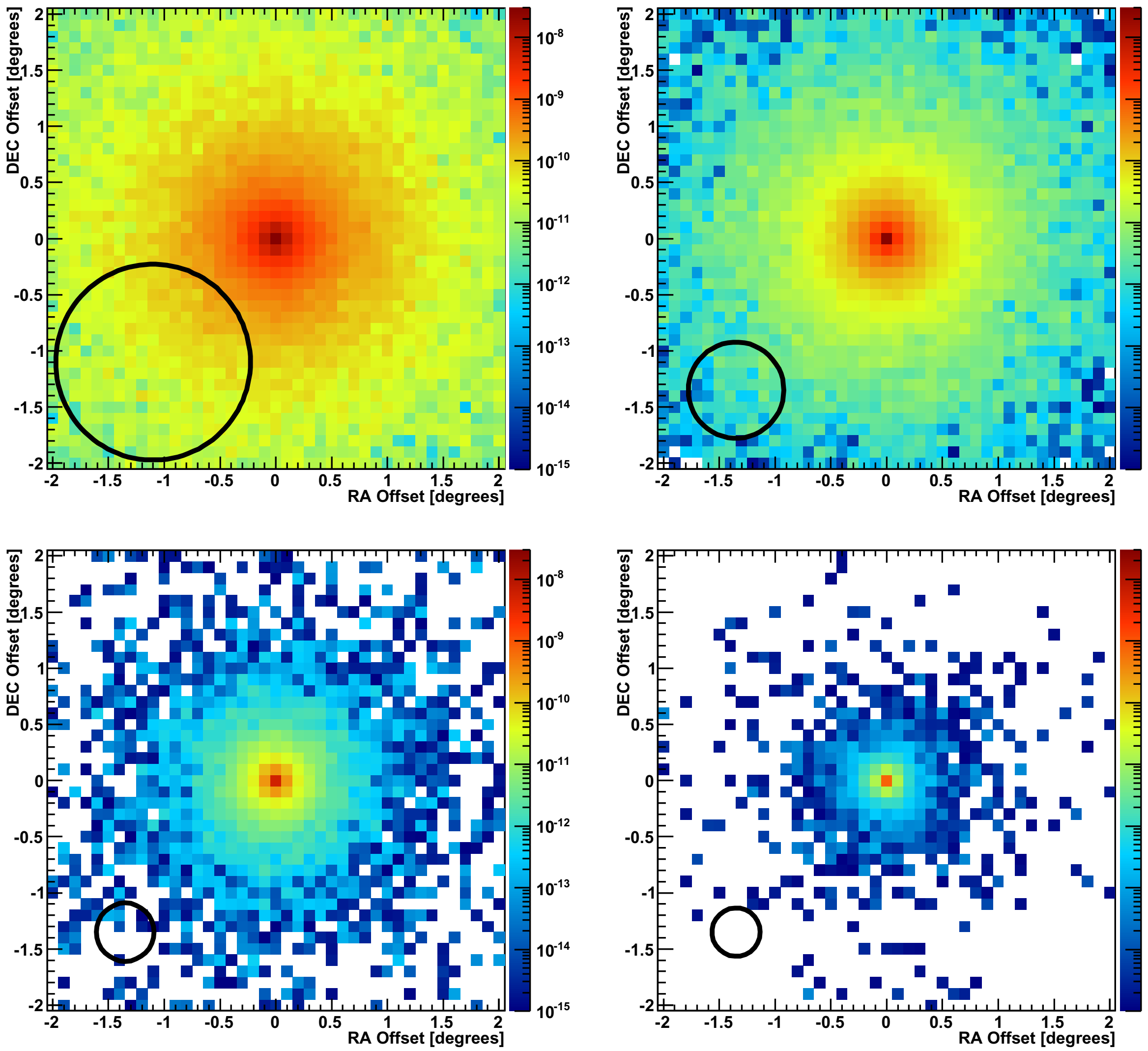

Figure 5.22: Extended halo emission for an EGMF strength of $B = 10^{-16}$ Gauss at four different energies: 1 GeV (top left), 2.7 GeV (top right), 8.6 GeV (bottom left), and 27 GeV (bottom right). The circle in the lower left of each plot shows the 68% containment radius of the *Fermi* LAT derived from the actual spacecraft pointing for RGB J0710+591.

10^{-17} Gauss to 10^{-16} Gauss for our fiducial blazar. The increasing size of the halo due to the spreading out of the cascade is readily apparent.

In addition to decreasing with the field strength, the extent of the halo also depends on the energy of the secondary gamma rays. Since gamma rays of higher energy tend to be produced by electrons of higher energy, which are present earlier in the development of the cascade and are less affected by the field strength, we expect the extent of the halo to decrease

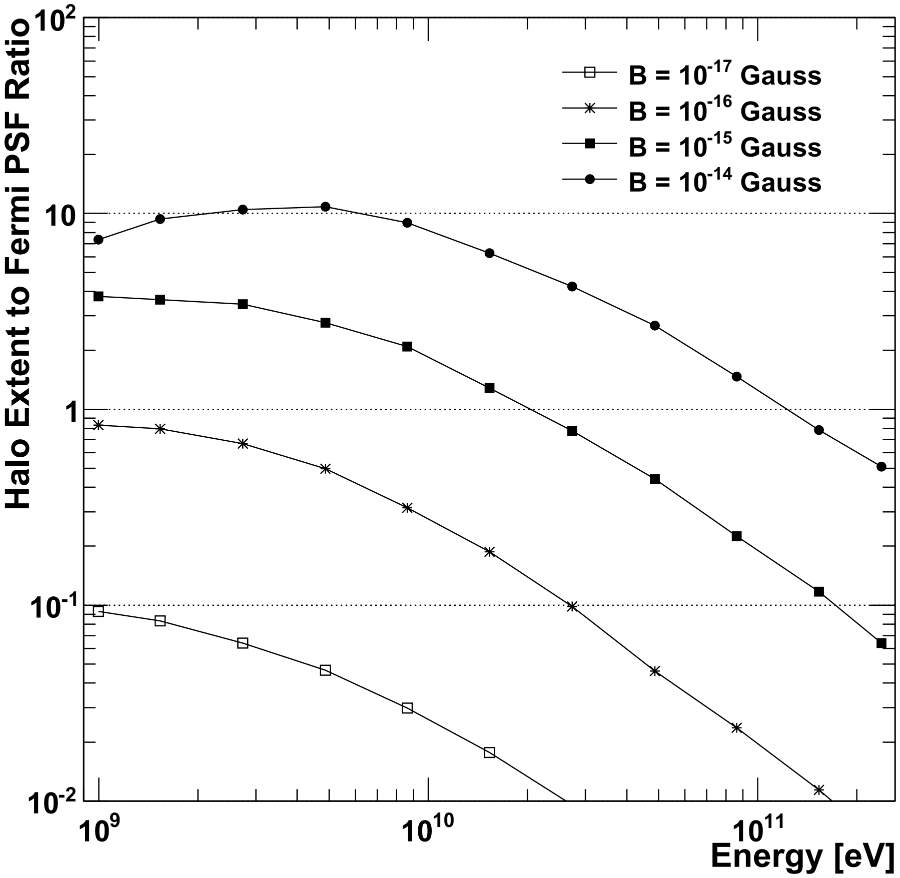

Figure 5.23: Ratio of the 68% containment radius of gamma rays in the halo with respect to that of the *Fermi* LAT for field strengths from 10^{-17} to 10^{-14} Gauss. The intrinsic spectrum of the blazar is a power law with a spectral index $\alpha = 1.5$ and a cutoff energy $E_C = 10$ TeV.

as the energy increases. Figure 5.22 shows that this is indeed the case. As is apparent in the figure, both the halo extent and the *Fermi* PSF decrease with energy. However, above 10 GeV, the halo extent decreases much more rapidly while the PSF stabilizes to a constant value, as indicated by Figure 3.2. The signature of the EGMF is therefore an extended halo that becomes pointlike with increasing energy.

The exact energy at which the halo becomes pointlike depends on the field strength. A good proxy for whether the halo appears pointlike or extended is, of course, the ratio of the halo extent to the instrument resolution. If this ratio is near unity, then the halo is sufficiently extended for the instrument to distinguish it from a point source but not so dilute that it cannot be detected. Figure 5.23 demonstrates that, under one particular assumption

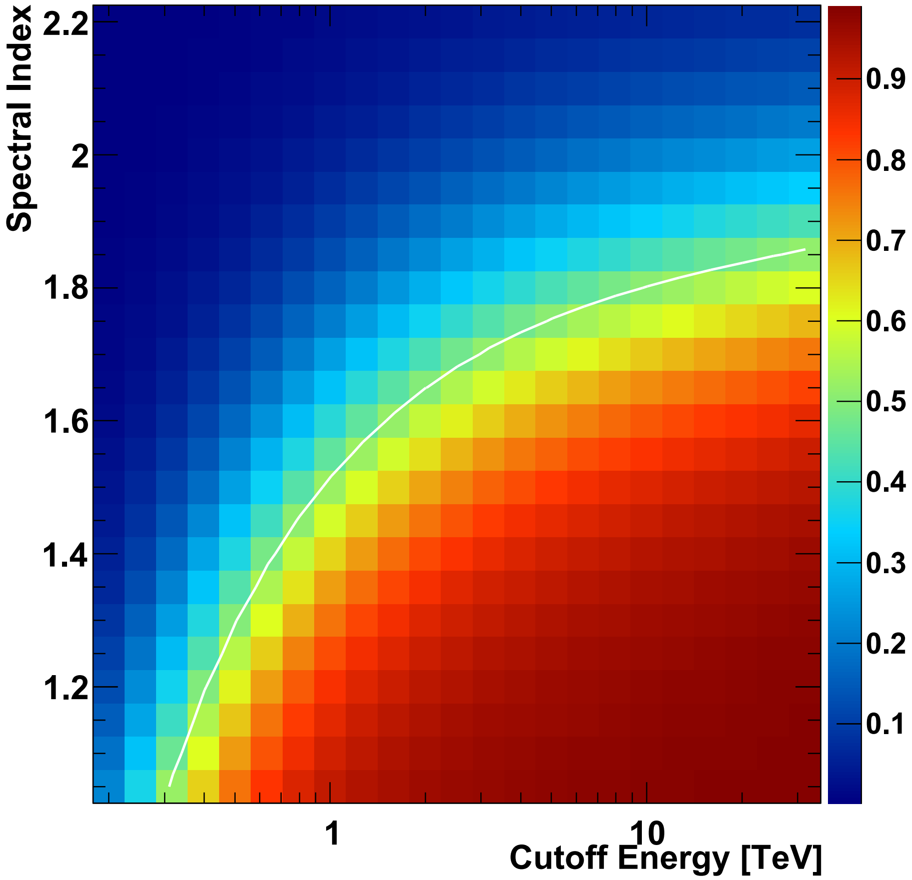

Figure 5.24: Fraction of gamma rays in the cascade as a function of spectral index and cutoff energy for a blazar at $z = 0.13$. The white contour indicates the region at which the total cascade and direct flux are equal.

about the intrinsic spectrum of the blazar, this ratio approaches unity for some energies in the *Fermi* energy range if the field strength lies between 10^{-17} and 10^{-14} Gauss. We therefore expect that a search for the energy-dependent morphology of the halo could deliver a positive detection of the EGMF if it is within this range.

Discrimination between pointlike and halo emission requires the halo flux to be at least comparable to the direct flux in the *Fermi* energy range. Figure 5.24 shows the ratio of the flux in the halo to the total flux as a function of the intrinsic spectral index and cutoff energy. The figure matches our expectation that hard sources with high cutoff energies will be cascade-dominated, while sources with soft spectra and low cutoff energies are dominated by the direct flux. In the presence of a magnetic field of sufficient strength, larger values of this ratio will lead to a stronger halo, whereas when the magnetic field is weak the cascade will enhance the pointlike emission from the blazar.

Blazars are, in general, highly variable objects both in the TeV and GeV energy bands. In determining the extent of the halo, we can neglect variability in the TeV range because short-term variations will be averaged out by the cascade process, the time scale for which can be on the order of 10^6 years. It is therefore important only to achieve an unbiased picture of the TeV emission over long time periods, averaging flaring states with periods of quiescent emission. However, the halo in the GeV range will of necessity be constant, since it is the average emission over the long time scales in the cascade. While variability in the *Fermi* observations is not ruled out by our model, we do expect any variability to be pointlike.

5.4.3 Time Profiles

In addition to the information available from the halo, it is possible to constrain the EGMF based on the time delays of gamma rays in the cascade with respect to the arrival of a flare of direct gamma rays. Since blazars are highly variable sources in the TeV energy band, we expect a characteristic decay of the light curve that is dependent on the field strength. Although such an investigation is beyond the scope of this work, it is in principle possible to detect this decay if the field strength is sufficiently weak, as indicated by Figure 5.25, in which the time delays of gamma rays in the cascade are plotted for field strengths of 0 and 10^{-18} Gauss. The average time delays for these three cases are, respectively, 10 minutes and 2 weeks. In the absence of evidence for a halo, the EGMF could be as weak as 10^{-18} Gauss if the blazar lifetimes are shorter than the time scales on which the cascade reaches steady state, in which case observations of the existence or absence of a decay in the light curve following a flare could be used to measure or constrain the field.

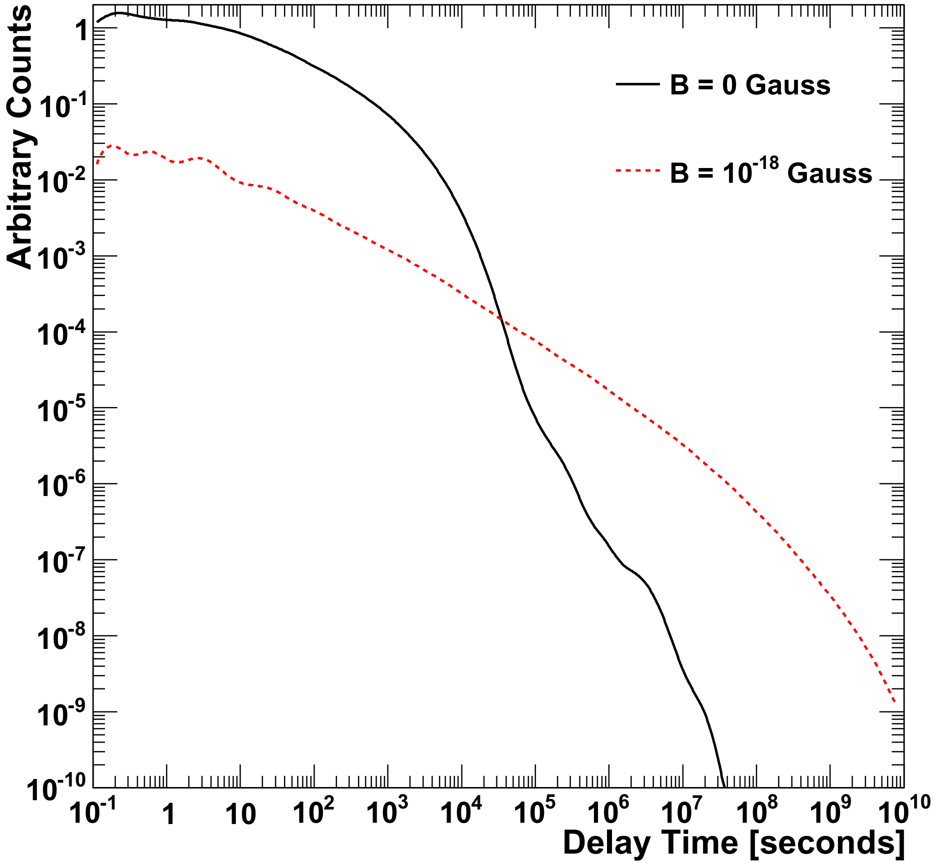

Figure 5.25: Characteristic time profiles of the cascade for a field strength at 0 and 10^{-18} Gauss. The fine structure in the curves is an artifact of the binning that should not be considered physical.

CHAPTER 6

THE SEARCH FOR BLAZAR HALOS IN THE EGMF CONTEXT

In this chapter, I present the results from a search for halos around select blazars and the interpretation of those results in the context of the EGMF. The Monte Carlo simulation described in Chapter 5 permits us to characterize the energy-dependent morphology of the cascade in the energy range accessible to the *Fermi* instrument, as well as to predict the spectrum measured by ground-based IACTs. While observations in these two energy bands individually are not very constraining, their combination can very strongly constrain the properties of the EGMF.

Using the semi-analytic model presented in Chapter 4, we found a lower limit on the EGMF strength of $\sim 3 \times 10^{-16}$ Gauss, but it was difficult to access the energy-dependent morphology of the halo of gamma rays around the blazar. The Monte Carlo simulation allows us to predict this halo straightforwardly and compare it to existing blazar observations. I use the simulation to conduct a general search for the specific energy-dependent morphology of the halo.

6.1 Assumptions

The interpretation of blazar halos is dependent on a large parameter space including the spectral properties of the source, the EBL, and the model for the EGMF. The difficulty of exploring this parameter space necessitates some assumptions regarding its properties. As in the rest of this work, I adopt the relatively low EBL model of Franceschini et al. (2008). For the EGMF model, I use a simple model that divides the volume of space into cubic "domains" of length L within which the field strength is constant. The orientation of the field within a domain is fixed to a random value independent of any other domain, so that L is representative of the correlation length as specified by Equation 1.2. The field strength is fixed to a constant value that is the same for every domain. In this way, we search for the dominant component of the EGMF in the voids of the LSS.

For blazars with a well measured redshift, the bulk of the remaining parameter space comprises characteristics of the spectrum intrinsic to the blazar itself. In cases where information on the properties of the blazar is available, we can use that information to narrow the parameter space. However, in general the time profile, relativistic beaming, and exact shape of the intrinsic spectrum are unknown. In such cases we estimate values that seem reasonable for an average blazar. The dominant parameters affecting the cascade are of course the spectral index and cutoff energy from Equation 3.1, since these two parameters control the level of the intrinsic flux in the TeV energy range that causes the cascade. As shown in Figure 5.24, these parameters strongly govern the capability of our search to detect a halo. We therefore allow these parameters to vary in our search while fixing all other parameters to reasonable estimates.

6.1.1 The Time Profile

As emphasized in Chapter 4, reliable blazar observations simultaneous in both the GeV and TeV energy ranges are limited to the past ~ 3 years. However, the time for gamma rays in the cascade to achieve a steady state can be on the order of 10^6 years, and there is no guarantee that the current activity of the blazar is representative of the activity over its lifetime. Periods of higher or lower activity in the past could affect the presently observed flux. Since 10^6 years is relatively short for galactic time scales, we therefore generally assume that the current observations of the blazar are representative of its average activity.

An additional complication is introduced because blazars are highly variable objects that tend to emit strong flares. As long as the EGMF is relatively strong, flares in the cascade will be averaged over the cascade time scale and we expect no time variation of the flux in the cascade. However, observations in the TeV band are sparse because the IACTs are pointed instruments, and the rate of flaring is unknown. Our adoption of a steady time profile for the flux therefore additionally assumes that the existing IACT observations are representative of the actual flaring rate averaged over the blazar lifetime.

6.1.2 Relativistic Beaming

Chapter 3 motivated the model of a blazar as relativistic populations of electrons boosted to a bulk Lorentz factor Γ, resulting in highly beamed objects. In the absence of direct measurements, we assume that $\Gamma = 10$, in accord, for example, with average measured values from misaligned AGN as determined by Hovatta et al. (2009). We furthermore assume that the viewing angle between the blazar jet direction and the line of sight to Earth is $\theta_V = 0$. We expect that the viewing angles of gamma-ray-detected AGN will be small because the opening angle of the beamed emission, which can be approximated as $\Gamma^{-1} \approx 5^\circ$, is relatively small. While misaligned AGN may exhibit halos, the direct flux in the TeV band is much weaker than in the aligned case (Neronov et al., 2010), making reliable estimates of the intrinsic spectrum that produces the cascade difficult.

6.1.3 Simulation Limits

As the electrons enter the Thomson regime, the number of gamma rays they produce increases inversely with the minimum energy for the gamma rays to be deemed observable, requiring roughly an order of magnitude more simulation time for every decade in energy. We therefore restrict our attention to cascade gamma rays above 1 GeV, ignoring any flux measured by *Fermi* from 100 MeV to 1 GeV. Since the lower-energy gamma rays are more sensitive to lower field strengths, the overall effect of this limitation is to raise the lower limit on the range of EGMF strengths to which our method is sensitive. However, given the flattening near 1 GeV of the curves in Figure 5.23, it is unlikely that including this information would substantially improve the sensitivity of our method.

6.1.4 The Intrinsic Spectrum

We assume that Equation 3.1 adequately models the blazar's intrinsic spectrum over the energy range from 1 GeV to 10 TeV. By scanning the spectral index α from 1.1 to 2.1 and the cutoff energy E_C from 200 GeV to 50 TeV, we explore the parameter space in a search for the cascade model that best reflects the existing observations for a particular blazar. Our assumed limits on α and E_C are particularly reasonable when the best-fit value is not at the edges of the space. In addition to avoiding an infinite-energy catastrophe, the exponential cutoff is physically motivated because primary gamma rays above 50 TeV are likely to interact sufficiently close to the blazar so that the electrons they produce sample not the EGMF in the voids, but rather the magnetic field local to the cluster hosting the blazar, as suggested by Figure 2.11. The very strong cluster field then isotropizes the electrons so that their upscattered emission forms an insignificant contribution to the cascade. The exponential cutoff can account for this lost flux in a natural way.

In principle, we could use additional information from low-energy observations to constrain the blazar spectrum further. However, we deliberately avoid this so that our conclusions are not based on any specific model of blazar emission. The models can be quite complicated, involving many parameters, and the existence of orphan flares (Kusunose & Takahara, 2006) implies that the emission mechanisms in blazars are not fully understood. An introduction to the basics of blazar modeling can be found in Aharonian (2004).

6.1.5 The EGMF Model

We assume that the correlation length of the magnetic field is $L_0 = 1$ Mpc, roughly the length over which an energetic electron cools to ~ 50 GeV, so that over their lifetimes the electrons sample only a single EGMF domain. If the correlation length is smaller, the electrons begin to experience a random walk across many domains, reducing the influence of the EGMF on the electrons' deflections. If halo features are predicted at a given angular size θ for a correlation length of L_0, then their apparent size when $L \ll L_0$ is, very roughly (Neronov & Semikoz, 2009),

$$\theta' \approx \sqrt{\frac{L}{L_0}}\theta. \tag{6.1}$$

A lower limit on the EGMF strength of B when $L = L_0$ will therefore become even more constraining if the correlation length is significantly smaller, since the field must be stronger than B to achieve the same deflection of the electrons.

6.1.6 Properties of the Cascade

Certain assumptions regarding the properties of the cascade are also necessary for the interpretation of halo data. Essey & Kusenko (2010) have noted that, since AGN may be sources of cosmic-ray nuclei, there could be an additional component to the cascade that arises due to cosmic-ray interactions with the EBL. Some observational evidence such as the existence of blazars at $z > 0.1$ with spectra that must be exceptionally hard to overcome the EBL attenuation may support this idea (Essey & Kusenko, 2011). However, it remains an open question whether significant cosmic-ray production occurs in blazars, so we assume that the cosmic-ray production by the blazars studied in this work is negligible.

We also make the assumption that inverse Compton and pair production are the dominant mechanisms for energy loss in the cascade. Recently, Broderick et al. (2011) pointed out that the cascades may be susceptible to plasma instabilities due to the electrons' interactions with the background of ionized hydrogen in extragalactic space, arguing that the rate of energy loss due to plasma instabilities is much larger than that due to inverse Compton scattering. A detailed study of the instabilities remains to be undertaken, however, and the precise nature of the role of plasma instabilities in the cascade is presently unclear. Lacking further information, we assume that this effect can be neglected.

6.2 Data Analysis

Data from both ground-based IACTs and the *Fermi* LAT are necessary for constraining the EGMF. Once the data are in hand, we proceed in the analysis by assuming a combination of intrinsic spectral index α, cutoff energy E_C, and EGMF strength B. For a given point in the parameter space, we use the results of the Monte Carlo simulation to predict the energy spectrum in the TeV range, along with the detailed energy-dependent morphology of the cascade in the GeV energy range. We explore the space by choosing 12 values of α from 1.1 to 2.1, 12 values of E_C from 200 GeV to 50 TeV, and 13 values of B, 12 evenly logarithmically spaced from 10^{-18} Gauss to 3.2×10^{-13} Gauss, as well as 0 Gauss, resulting in a parameter space of 1,872 separate models. We then fit the data to those predictions. At the point of fitting, the total luminosity of the source is the only remaining free parameter, and we determine the best-fit value consistent with data from both energy ranges.

6.2.1 Ground-Based Instruments

As discussed in Section 3.3, the present generation of IACTs includes VERITAS, HESS, and MAGIC, all of which have detected a number of blazars in the TeV energy range[1]. The sensitivities of these instruments extend from $\sim$ 100 GeV to greater than 30 TeV. We use the IACT observations to determine reliable spectra in the TeV-energy range in order to interpret the observed properties of a hypothetical halo resulting from interactions between the primary gamma rays and the EBL and CMB. Toward that end, we use the published spectra on specific blazars from observations performed by these instruments. Because these

---

[1] A detailed catalog of TeV sources can be found at http://tevcat.uchicago.edu/.

spectra are typically derived under the assumption that the source is pointlike, we must account for possible halo extension in the TeV energy range. We accomplish this with a simple, energy-independent model of the total gamma-ray PSF of the instrument, derived from Aharonian et al. (2006). The exact shape of the PSF is relatively unimportant, and we ignore any possible dependence on the energy of the measured gamma rays.

We next proceed by applying the simple PSF model to the simulated predictions in the TeV energy range. Recalling from Section 3.3 that a cut on θ^2 is used to define the point-source region in an IACT analysis, we count only the simulated photons that fall within the θ^2 cut, obtaining a prediction F_0 for the flux. Since the model of the PSF is known, we know the probability p for a pointlike gamma ray to be reconstructed within the θ^2 cut, and so we can correct the flux to obtain the "true" flux $F = F_0/p$. Obviously, this procedure does not determine the correct value of the flux if there is a halo present because the probability for a halo gamma ray to be reconstructed within the θ^2 cut is less than p due to its extension. Rather, this procedure mimics the analysis conducted to obtain the published spectrum, producing a value that can be compared to the published results and additionally accounting for any possible extension due to the halo, which can be important, especially at lower energies.

6.2.2 Fermi Data

We analyze publicly available data from more than three and a half years of *Fermi* LAT observations starting in August 2008 and ending in March 2012 to determine the flux in the GeV range. Our analysis employs version v9r23p1 of the *Fermi* tools, with the on-orbit instrument response functions P7SOURCE_V6[2]. In contrast to the analysis discussed in Chapter 4, in which we calculated the spectrum within the 68% containment radius of the *Fermi* PSF, we fully characterize the energy-dependent morphology of the cascade in an effort to maximize our use of the available information. After a binned analysis consisting of event selection, the creation of counts maps, and exposure computation, we conduct 1,872 separate likelihood analyses to assess the probability of every model in our parameter space.

For the pre-likelihood analysis, we select events of class 2, which are intended for general

---

[2] Further information on *Fermi* data analysis is available at the *Fermi* Science Support Center's website, http://fermi.gsfc.nasa.gov/ssc/.

source analysis. We also adopt a region of interest (ROI) size appropriate for analysis above 1 GeV of 20°, a counts cube size of 28°, and an exposure cube size of 70°. During the likelihood analysis, we include all sources within 30° of the position of our analyzed blazar, fixing all parameters of those sources greater than 10° from the ROI center and keeping free only the normalization for sources between 2° and 10° from the center. We also include the extragalactic diffuse model iso_p7v6source and the Galactic diffuse model gal_2yearp7v6_v0.

In order to include the predicted energy-dependent morphology of the blazar in our analysis, we eschew the standard *Fermi* point-source models and employ instead a MapCubeFunction, which is the same type of model used for the Galactic diffuse flux. The MapCubeFunction permits us to specify any arbitrary halo morphology at discrete energies. In constructing these source models from the simulated data, we use an ideal PSF that leaves the simulated gamma rays' directions unaltered, and we allow the gtsrcmaps tool to account for the *Fermi* IRFs.

Because the Galactic diffuse model is highly detailed, it occupies a large amount of computer memory. In order to reduce the memory requirements for a single run and thus facilitate the parallel processing of the 1,872 jobs, we replace the Galactic diffuse map with a smaller version trimmed to a 60° by 60° region centered on the position of the blazar. This smaller region will contain with very high certainty all of the gamma rays from the Galactic diffuse that could be reconstructed into our ROI. We verify that our trimmed version of the Galactic diffuse produces the same results as the full version by running standard likelihood analyses using both models. The "Point Source" row in Table 6.1 shows that these analyses are not substantially different. Additionally, we investigated whether different field models could be affected by the cut Galactic diffuse model, since the extent of the source depends on the field and this could make our results sensitive to other extended sources such as the Galactic diffuse. Selecting a cutoff energy of 11 TeV and a spectral index of 1.55 and trying three separate fields, we find that the cut Galactic diffuse model has little impact on the test statistic of the source for the fields, as shown in the lower three rows of Table 6.1. We are therefore confident that the cut Galactic diffuse model does not strongly influence our results and we use it routinely in our analysis.

	Full Diffuse Model			**Cut Diffuse Model**		
	Source TS	**Source Flux**	**Diffuse Flux**	**Source TS**	**Source Flux**	**Diffuse Flux**
Point Source	166.98	6.72 ±1.24	0.987 ±0.013	166.87	6.69 ±1.12	1.025 ±0.014
$B = 0$ **Gauss**	159.98	0.562 ±0.084	0.987 ±0.012	159.88	0.561 ±0.084	1.025 ±0.013
$B = 10^{-16}$ **Gauss**	156.24	0.657 ±0.099	0.987 ±0.012	156.09	0.655 ±0.099	1.025 ±0.013
$B = 10^{-13}$ **Gauss**	164.40	2.61 ±0.40	0.987 ±0.012	164.32	2.60 ±0.40	1.025 ±0.013

Table 6.1: Results from *Fermi* data analyses with the full Galactic diffuse and cut Galactic diffuse models for the blazar RGB J0710+591. The Galactic diffuse fluxes are with respect to the nominal value. The source fluxes are in 10^{-10} gamma rays cm^{-2} s^{-1} for the point source and relative to the best-fit TeV spectrum for the specific field models. Although the cut Galactic diffuse flux is systematically high by a slight amount, the test statistic for the source is not substantially different between the full and cut models.

6.2.3 Combining the Data

For the TeV data, we fit our predicted curve to a set of data points representing the measured spectrum, obtaining the χ^2 value of the fit. If we assume that the data are normally distributed, then we can write χ^2 as

$$\chi^2 = -2\ln(L_{\mathrm{TeV}}), \tag{6.2}$$

where L_{TeV} is the likelihood. The *Fermi* data analysis yields a test-statistic value T given by

$$T = -2\ln\left(\frac{L_0}{L_{\mathrm{GeV}}}\right), \tag{6.3}$$

where L_0 is the maximum likelihood of the data under the null hypothesis that no source is present, and L_{GeV} is the maximum likelihood for the source model given the data. By inspection of Equations 6.2 and 6.3, it is clear we can multiply the likelihoods L_{TeV} and L_{GeV} by constructing a total test statistic $\chi^2 - T$. Compared to the χ^2 value, the *Fermi* test statistic T is likely to be very large for strong sources because it is calculated with respect to the null hypothesis. However, when comparing two models, we are interested in the difference between the calculated values of $\chi^2 - T$, and the overall scale is unimportant (James, 2006).

For each of the 1,872 models, we construct the total test statistic values $\chi^2 - T$, leaving the total luminosity as the only free parameter describing the blazar. This is accomplished by performing repeated *Fermi* likelihood analyses with the luminosity fixed, adding the χ^2 value for the given luminosity, and adaptively scanning the luminosity space until the variation between points is sufficiently small. A parabolic fit to the measured points determines the final best-fit value for the combined statistic. We then project the total statistic onto the EGMF strength in a manner similar to our analysis in Section 4.2. By finding the point at which this curve surpasses its minimum by a certain value, we can measure or constrain the field at a desired level of confidence.

6.3 Data Verification

Detecting the relatively weak halo on top of the pointlike emission from the blazar requires a solid understanding of the *Fermi* instrument response. In order to gain confidence that the search described in this chapter would allow us to detect a halo if it did exist, we have conducted a set of rigorous tests to ensure the accuracy and stability of the method. Throughout this section, we focus on results from the blazar RGB J0710+591 to illustrate our data verification procedure.

6.3.1 Procedure

The testing procedure begins by selecting one of the 1,872 models and assuming that it gives the "correct" distribution of gamma rays from the source, which we refer to as the test model. Due to their large errors, in general the TeV data can be made to fit the spectrum well simply via the selection of an appropriate luminosity and sufficiently large cutoff energy, as shown in Section 5.4.1. Given that the VERITAS data on RGB J0710+591 extend to ~ 6 TeV, however, it is unlikely that the TeV data will plausibly be drawn from the test model distribution unless the cutoff energy is chosen to be above ~ 1 TeV. Nevertheless, we find that it can be instructive to include such models in the verification, so we place no limit on the intrinsic spectrum, and we focus on assessing the validity of the GeV-scale predictions.

We use the *Fermi* tool gtobssim to generate a simulated data set for the *Fermi* LAT using the actual pointing history of the spacecraft and a specified set of gamma-ray sources. Our simulated data set covers a time range of 10^8 seconds, slightly more than three years, beginning on 15 August 2008. For the sources we use the same set that we selected in Section 6.2.2, placing our test model for the blazar at the center of the ROI. Since some of the sources' spectra are modeled by functions that are unavailable to the gtobssim tool, we convert these spectra to power laws with similar normalization, expecting that the results of fits to the simulated data with these replacements will encompass only minor changes. We then treat the simulated data as real data, passing them through the analysis chain and finding the best-fit combined statistic for all 1,872 models, without using our knowledge of the "true" intrinsic spectrum to aid our analysis in any way. After projecting onto the field-strength axis, we expect with high confidence that the known "correct" field strength from the test model will be within the allowed region.

Running the verification procedure is highly processor-intensive. From start to finish, a single simulated data set requires more than 10^4 core-hours of processing time. For this reason, it is computationally infeasible to run many simulations for one test model and demonstrate that the confidence level accurately reflects the probability of finding the "correct" field strength from the test model within the quoted range. It is also time-consuming to process additional models; in total we use four separate models in the data verification procedure, one which we select with malice aforethought to give results similar to the real observations in the *Fermi* energy band, and three which we choose at random using a com-

Test	**Field [Gauss]**	α	E_C	**Counts**	**Fit Field [Gauss]**	**TeV** χ^2**/dof**
1	3×10^{-16}	1.55	18 TeV	132	$(3.9 \pm 1.6) \times 10^{-16}$	1.77/4
2	10^{-18}	1.9	200 GeV	1878	none	21.7/4
3	3×10^{-16}	1.83	50 TeV	214	none	2.11/4
4	10^{-15}	1.19	30 TeV	70	$(4.8 \pm 3.4) \times 10^{-16}$	1.98/4

Table 6.2: Parameters from one predetermined and three randomly selected models for the intrinsic spectrum of RGB J0710+591.

puter program. These latter three cases can therefore be thought of as double-blind tests of the analysis procedure. A summary of these tests, along with the parameters for their intrinsic spectra, the true field, the field reconstructed at 68% confidence, and the observed number of counts associated with our source, appears in Table 6.3.1. For two of these models, Tests 2 and 3, the blazar parameters are located in a region of Figure 5.24 unfavorable to halo detection. Consequently, our procedure fails to reconstruct any field strength. Tests 1 and 4, however, are in a favorable region for halo detection. In Test 1, the true field is well within the error range at 68% confidence, and for Test 4 the true field is only slightly outside this range. Since our overall method is sensitive only to the order of magnitude of the field strength, we expect that this verification procedure is adequate.

6.3.2 Tests

For our first test, we select a test model with a spectral index of $\alpha = 1.55$, a cutoff energy $E_C = 18$ TeV, and a field strength of $B = 3 \times 10^{-16}$ Gauss. This model is calculated to provide a high level of statistics for detecting the halo in an EGMF range for which the halo size is comparable to the instrument PSF. As a first test, it demonstrates the capability of the search to detect a halo in the optimum situation of a hard, high-energy source and a magnetic field amenable to producing a halo in the *Fermi* energy range. We summarize the results of this first test in Figure 6.1, in which it is evident that the correct field is well within the reconstructed range of $B = (3.9 \pm 1.6) \times 10^{-16}$ Gauss. This gives us confidence that our analysis procedure can reconstruct the field in an optimistic case.

As is evident by the number of counts shown in Table 6.3.1, the three double-blind

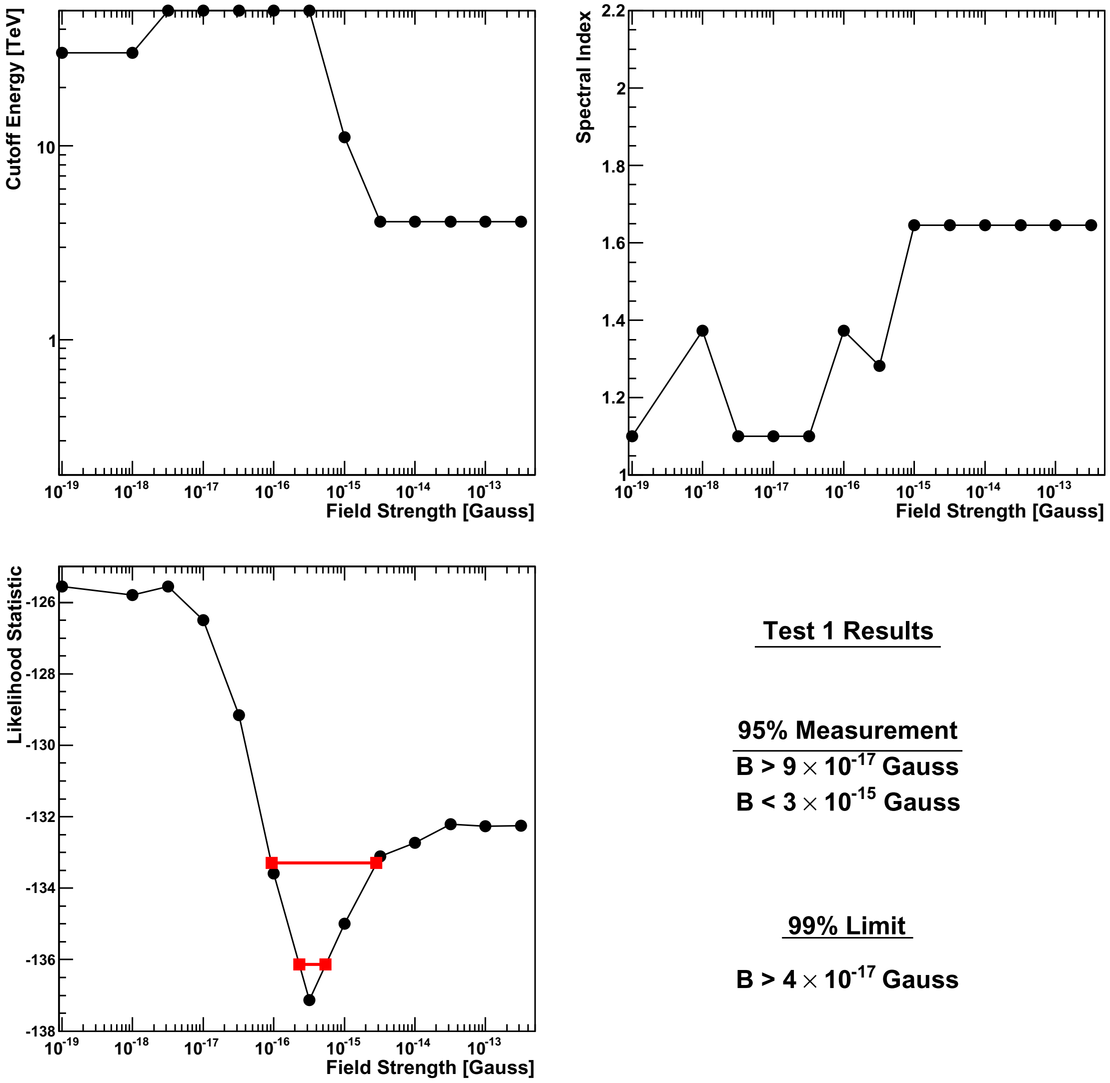

Figure 6.1: Summary of the results of Test 1 from Table 6.3.1. The best-fit spectral index and cutoff energy as a function of field strength appear in the top left and top right, respectively. The bottom left panel shows the likelihood statistic curve as a function of EGMF strength, while the bottom right panel summarizes the conclusions that can be drawn about the field strength for this test. The points at 10^{-19} Gauss are actually computed at 0 Gauss. The red bars indicate the 1-σ and 95% confidence measurements of the field.

tests fortuitously covered a wide range of intrinsic source models leading to very different predictions in the *Fermi* energy band. In the first test, the intrinsic spectrum spectrum is very pessimistic for detecting a halo: the spectral index is very soft at 1.9 and the cutoff energy of 200 GeV is as low as our analysis procedure tests. For this reason, even the TeV

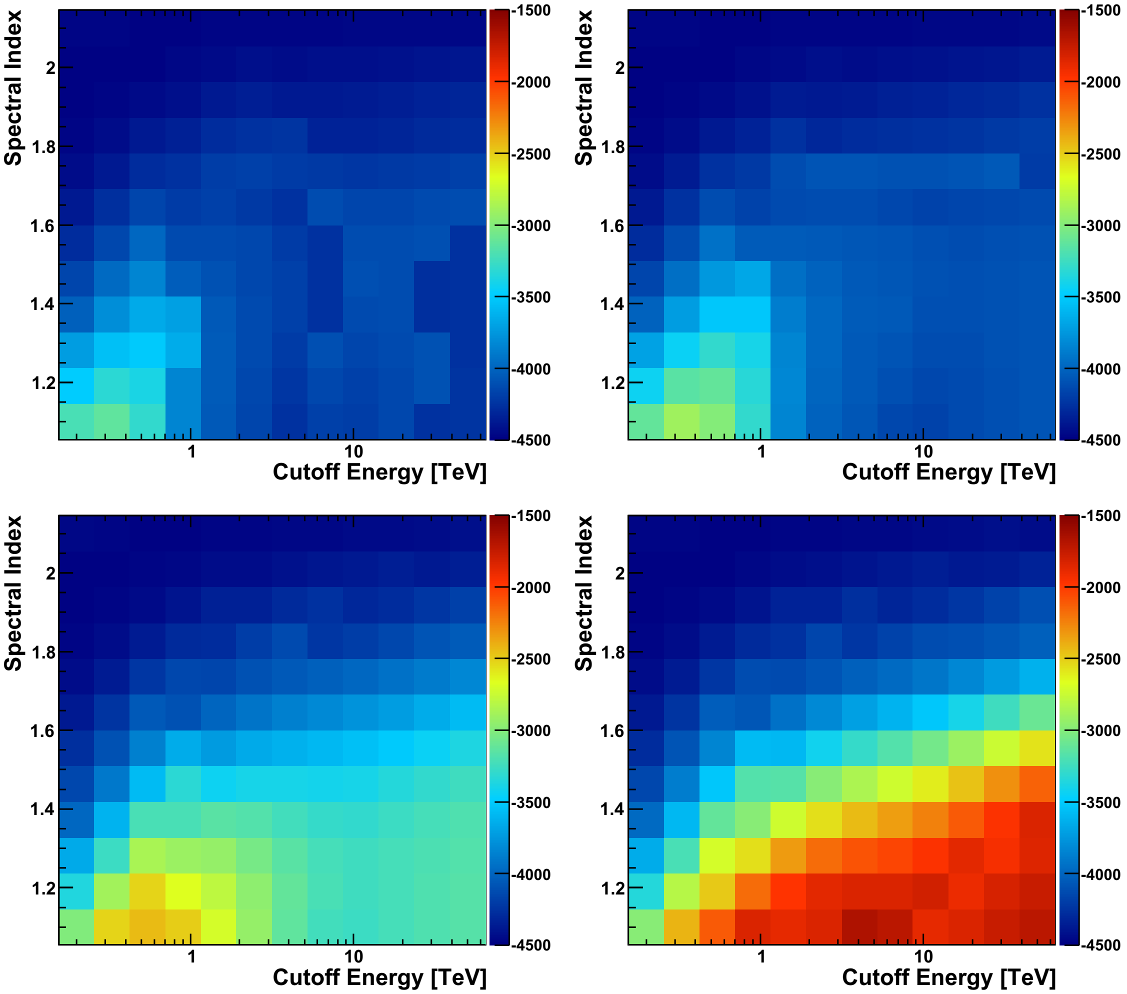

Figure 6.2: Likelihood statistic maps for Test 2 from Table 6.3.1. The EGMF strength in Gauss is 10^{-17} (top left), 10^{-16} (top right), 10^{-15} (bottom left), and 10^{-14} (bottom right).

fit to the spectrum alone is rather poor: the χ^2 of the fit per degree of freedom is 21.7/4, corresponding to a probability of 2.3×10^{-4}. The total luminosity must be greatly increased in order to achieve even this poor fit, and the very soft spectrum consequently dictates that the *Fermi* emission must be very high, leading to the production of a large number of gamma-ray counts. Additionally, the field strength of 10^{-18} Gauss is very low, implying that the halo will be undetectable and all of this very strong *Fermi* emission will appear pointlike, further softening the spectrum.

It is instructive to look at the likelihood statistic maps as a function of cutoff energy and spectral index, which appear in Figure 6.2 for four different values of the field strength.

In general, when the spectral index is soft, the models tend to fit well independent of the cutoff energy, since there are very few gamma rays with sufficient energies to generate the halo. For all fields, hard spectra with low cutoff energies fit poorly because there is again no halo, and the hard spectral index is a poor match to the "true" spectral index of 1.9 in the GeV energy range. For low fields, this problem can be remedied by moving to higher cutoff energies, where there is still no halo since the field is weak, but the overall effect of the cascade is to soften the spectrum, as anticipated by Figure 5.20, toward the correct value. When the field is strong, however, the cascade spreads out into the halo, and this softening is no longer possible, explaining the very poor fits in the bottom right corner of the plot for the 10^{-15} and 10^{-14} Gauss cases.

Figure 6.3 summarizes the results of the second test. It is obvious that the correct values of soft spectral index and low cutoff energy are strongly favored. As expected, this model provides no sensitivity to the EGMF strength. In fact, the trend in the bottom left plot of Figure 6.3 appears to be slightly negative, in the wrong direction. However, this trend is hardly significant, given the scale of the plot.

In the third test, the spectral index is again soft at 1.83 but the cutoff energy is an extremely high 50 TeV. As shown in Table 6.3.1, the fit to the TeV data is very good, so unlike the previous test we expect this test to reflect a plausible situation for the blazar, given the TeV data alone. The field strength for this test is right in the range where we should be able to detect it, so the only question is whether the high cutoff energy can win out over the soft spectral index and produce a large enough halo signal to be detected. However, Figure 5.24 shows that the expected fraction of gamma rays in the halo for this case is very nearly comparable to the fraction of direct gamma rays, so we do not expect the results to be very constraining. Additionally, according to Table 6.3.1, there are fewer gamma rays in this test. This is mainly due to the higher cutoff energy that permits a more reasonable total luminosity to be fit to the TeV data. We therefore expect that this test will have little sensitivity to the field strength, and that the overall scale of the likelihood curve will be smaller in magnitude that in the second test, owing to the smaller number of gamma rays associated with the source. Figure 6.4 confirms these expectations.

The fourth test also fits the TeV data very well. Although the cutoff energy is high at 30 TeV, the intrinsic spectrum for this test is rather weak when the hard spectral index $\alpha = 1.19$ is extrapolated to lower energies, so the number of simulated *Fermi* gamma rays is

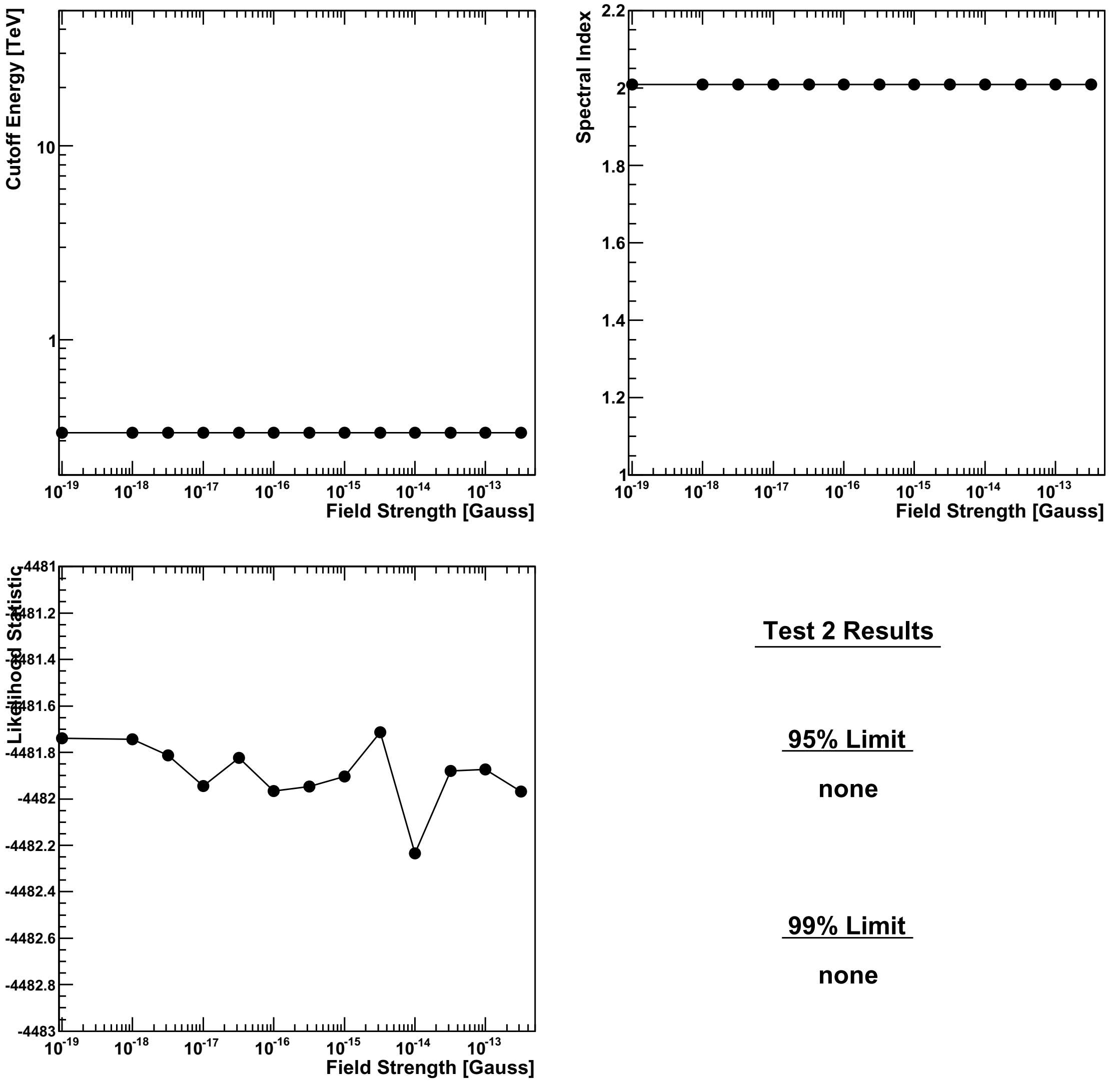

Figure 6.3: Summary of the results of Test 2 from Table 6.3.1. The best-fit spectral index and cutoff energy as a function of field strength appear in the top left and top right, respectively. The bottom left panel shows the likelihood statistic curve as a function of EGMF strength, while the bottom right panel summarizes the conclusions that can be drawn about the field strength for this test. The points at 10^{-19} Gauss are actually computed at 0 Gauss.

relatively low. The field of 10^{-15} Gauss is well within the detectable range, and according to Figure 5.24, the *Fermi* energy range should be dominated by halo gamma rays. As shown in Figure 6.5, our procedure reconstructs the field to be $B = (4.8 \pm 3.4) \times 10^{-16}$ at the 68% confidence level. The true field lies just slightly outside this range, but this is not surprising since the probability for this occuring is about 32%. At 95% confidence, our method allows

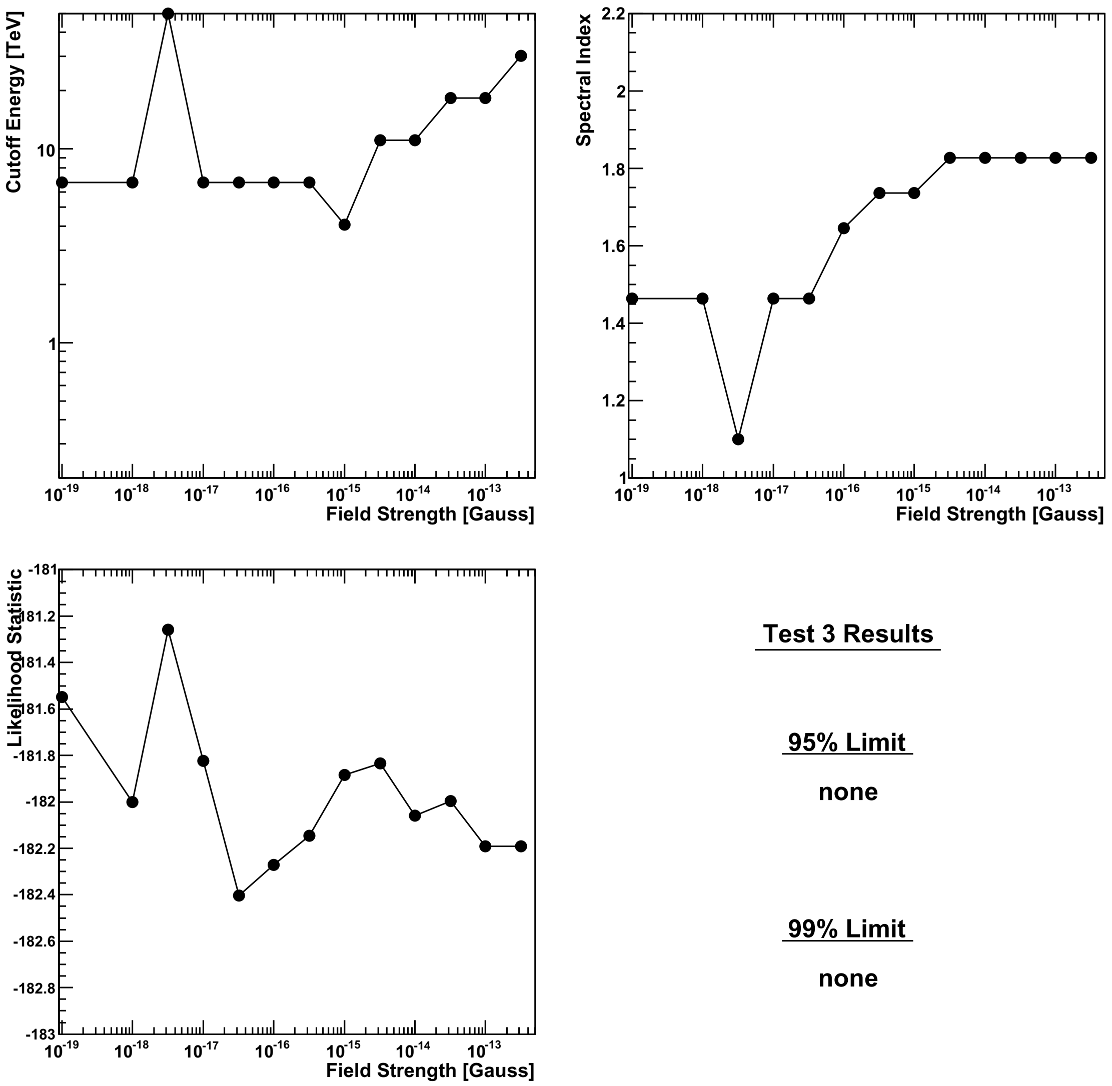

Figure 6.4: Summary of the results of Test 3 from Table 6.3.1. The description of the plots is the same as in Figure 6.1.

only a lower limit to be placed on the field strength, and in this case we find $B > 4 \times 10^{-17}$ Gauss, and the true field is clearly allowed.

The results of the data verification tests indicate that our procedure can accurately reconstruct the field strength in the event that a halo is detectable. Furthermore, the behavior of the fits matches our expectations from a qualitative analysis of each tested situation. As indicated in Figure 5.23, detectable field strengths range from $\sim 10^{-17}$ to $\sim 10^{-14}$ Gauss, above which the halo becomes too extended in the *Fermi* data for it to be distinguished

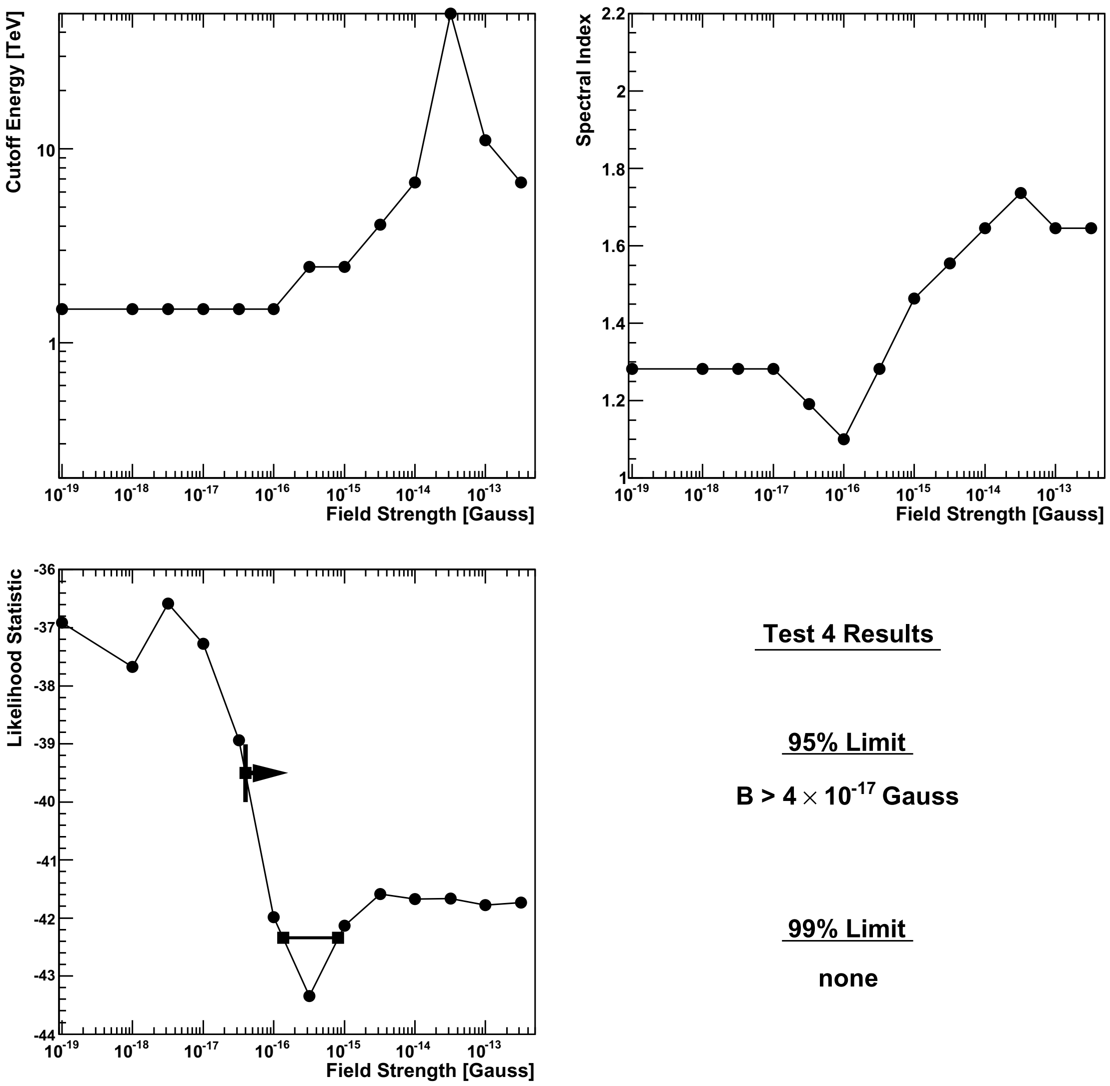

Figure 6.5: Summary of the results of Test 4 from Table 6.3.1. The description of the plots is the same as in Figure 6.1.

from the Galactic and extragalactic diffuse backgrounds. This upper limit should of course be considered rather loose; although it is true that the *Fermi* PSF may be similar to the halo size at large energies when the field is as strong as 10^{-14} Gauss, the flux of gamma rays generally decreases with energy, and *Fermi* may not collect enough gamma rays to be able to distinguish between the extended halo and a point source. With a high degree of confidence, however, we can search for EGMF strengths near $\sim 10^{-16}$ Gauss using our halo analysis procedure.

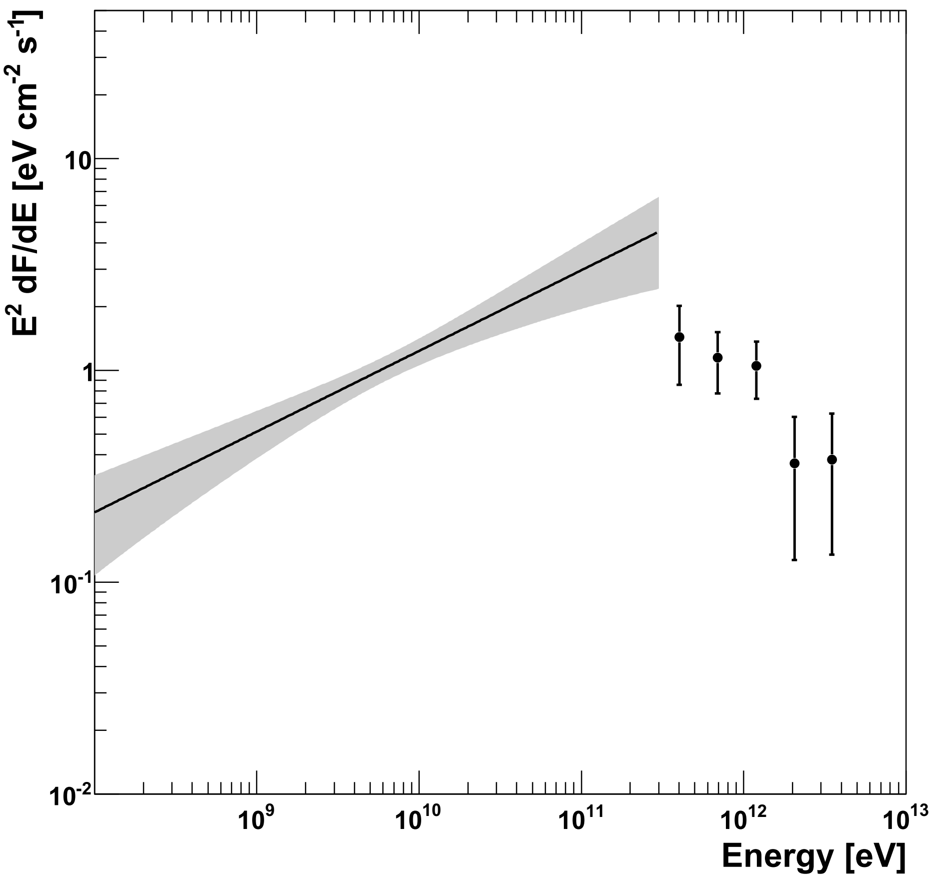

Figure 6.6: Total observed gamma-ray spectrum of RGB J0710+591, including the VERITAS data points from Acciari et al. (2010) and the *Fermi* best-fit spectrum (solid line) and confidence band (shaded region).

6.4 Halo Limits

We at last turn our attention to the results from the search for halos around blazars detected by both the *Fermi* LAT and the IACTs. I choose two HBL objects, RGB J0710+591, with a redshift of $z = 0.125$, and 1ES 0229+200, located at $z = 0.139$. For both of these sources, I use the predictions from the simulation run at a redshift of $z = 0.13$, which should provide a sufficient approximation to the redshift in either case.

6.4.1 RGB J0710+591

In Chapter 4, we placed limits on the strength of the EGMF based on spectral data from the blazar RGB J0710+591, which is located at a right ascension of $07^h10^m26.4^s$ (107.625°) and declination of $+59°09'00''$ (59.139°). The total spectrum of this blazar appears in Figure 6.6, in which the TeV-scale data points from the VERITAS observations (Acciari et al., 2010) and the GeV-scale data points from our own analysis are shown. We derive the *Fermi* data points using an unbinned likelihood analysis under the assumption that the spectrum is well modeled by a power law across the entire energy range accessible to *Fermi*. Additionally, we include the likelihood confidence band from the overall power-law fit to the total data set from 100 MeV to 300 GeV.

We conduct a binned *Fermi* analysis of the data in the vicinity of RGB J0710+591 as described in Section 6.2.2, after which we apply our analysis procedure to search for the extended halo emission. Figure 6.7 shows the likelihood statistic maps for the analysis, using the same fields that were presented in Section 6.3.2. It is clear that the results favor an EGMF that is relatively strong, since the minimum of the maps continues to decrease as the field strength increases.

Figure 6.8 summarizes the information from the analysis performed on RGB J0710+591. The best-fit cutoff energies and spectral indices lie well within the search range, giving us confidence that we have sufficiently explored the parameter space. The increase of both the cutoff energy and spectral index with field strength is driven by the need to match the IACT observations. That is, if the cutoff energy is low, within the TeV data, then the spectral index should become harder in order to match both ends of the TeV spectrum. Correspondingly, as the cutoff energy increases, it no longer affects the TeV data points, which are then best fit by a slightly softer power law.

Although our likelihood curve is insufficient for limiting the field at 99% confidence, we do achieve a 95% confidence limit of $B > 7 \times 10^{-16}$ Gauss. We interpret this limit as the absence of a halo. Our result validates previous results that used the spectral data alone to suggest that the strength of the EGMF is greater than $\sim 10^{-16}$ Gauss (Taylor et al., 2011). As anticipated by Figure 5.23, the likelihood curve flattens out above 10^{-14} Gauss, where our method becomes insensitive to the large extended halo around the point source. By selecting other blazar targets and applying the same analysis, we therefore expect that

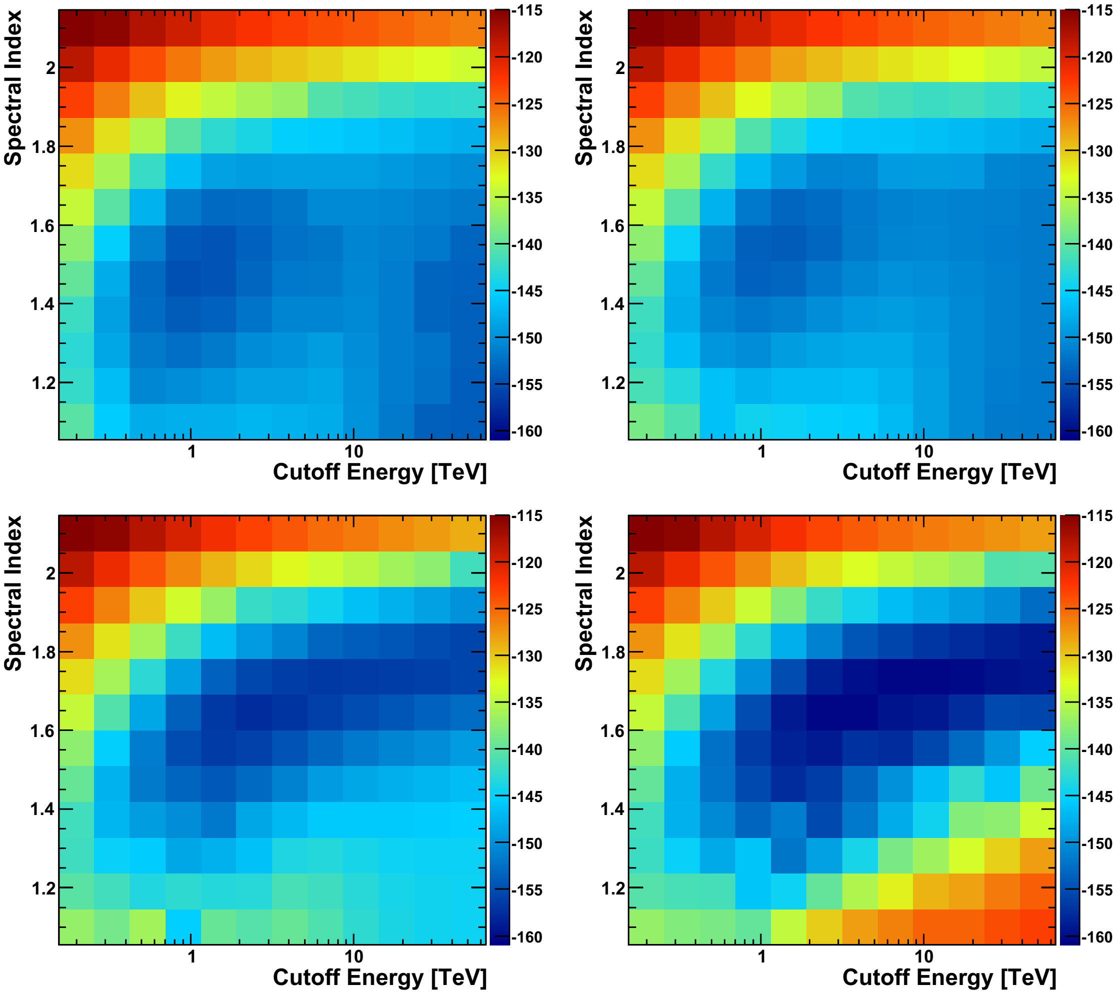

Figure 6.7: Likelihood statistic maps from the analysis of RGB J0710+591. The EGMF strength in Gauss is 10^{-17} (top left), 10^{-16} (top right), 10^{-15} (bottom left), and 10^{-14} (bottom right).

our method could rule out fields up to 10^{-14} Gauss at a confidence level greater than 95%.

6.4.2 1ES 0229+200

Another popular HBL for EGMF studies is 1ES 0229+200, located at a right ascension of $02^h32^m53.2^s$ (38.202°) and declination of $+20°16'21''$ (20.288°). The IACT spectrum for this blazar is measured by HESS (Aharonian et al., 2007), and it extends to 11 TeV, somewhat higher than the spectrum of RGB J0710+591. Also an HBL object, 1ES 0229+200 is only weakly detected by *Fermi*, as shown in Figure 6.9, in which we plot the combined GeV-TeV

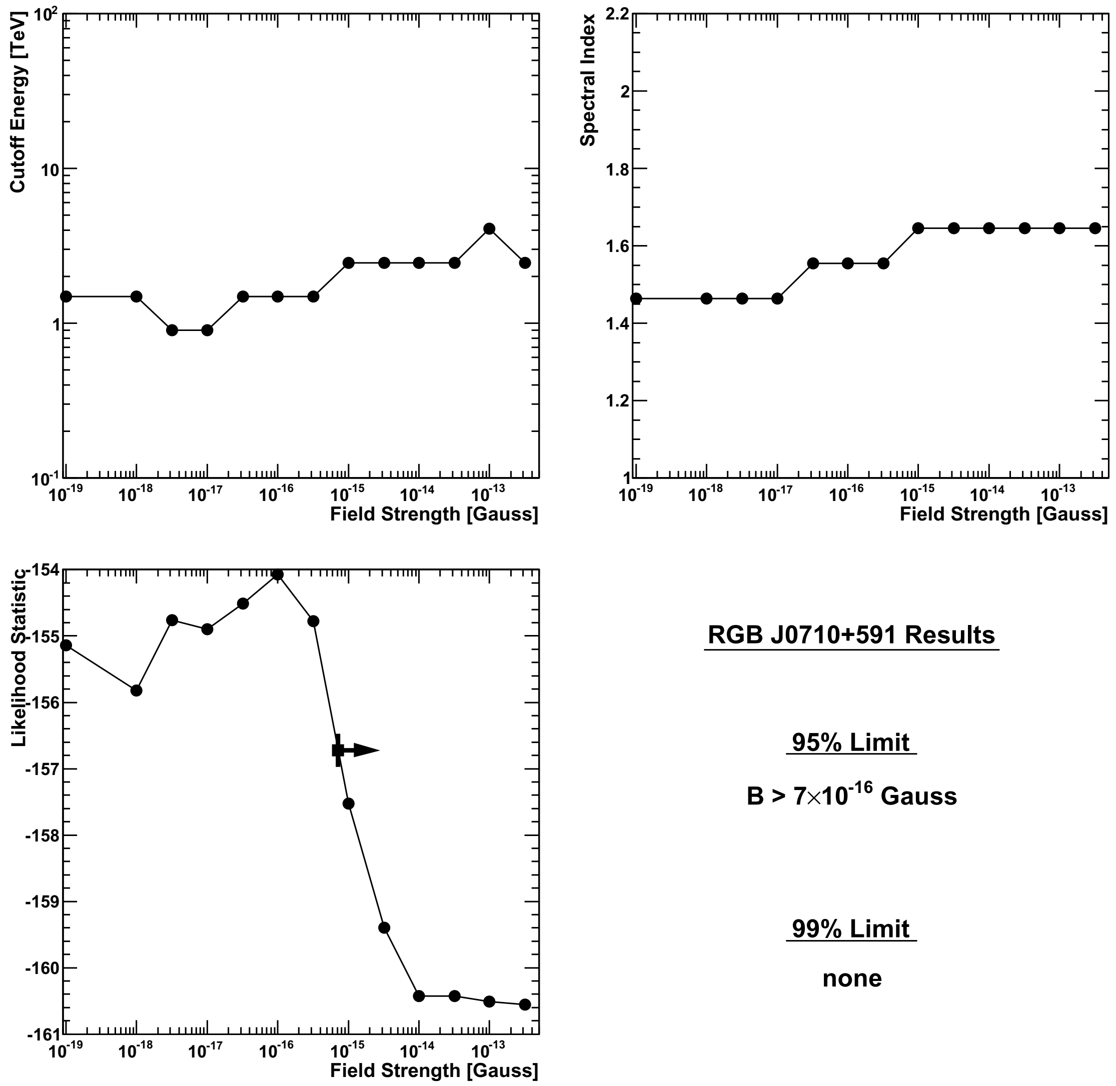

Figure 6.8: Summary of the results from the analysis of RGB J0710+591. The description of the plots is the same as in Figure 6.1.

spectrum. It is therefore unclear at the outset how the results of the halo search around 1ES 0229+200 will perform with respect to those around RGB J0710+591. Although the spectrum is more promising in the TeV band, likely extending to high cutoff energies, the weak *Fermi* detection suggests that the halo would be more difficult to detect.

The combined spectrum of 1ES 0229+200 appearing in Figure 6.9 again shows good agreement between the *Fermi* data points and the TeV observations, which are reported by the HESS experiment. Because 1ES 0229+200 is a weak source in the *Fermi* energy range,

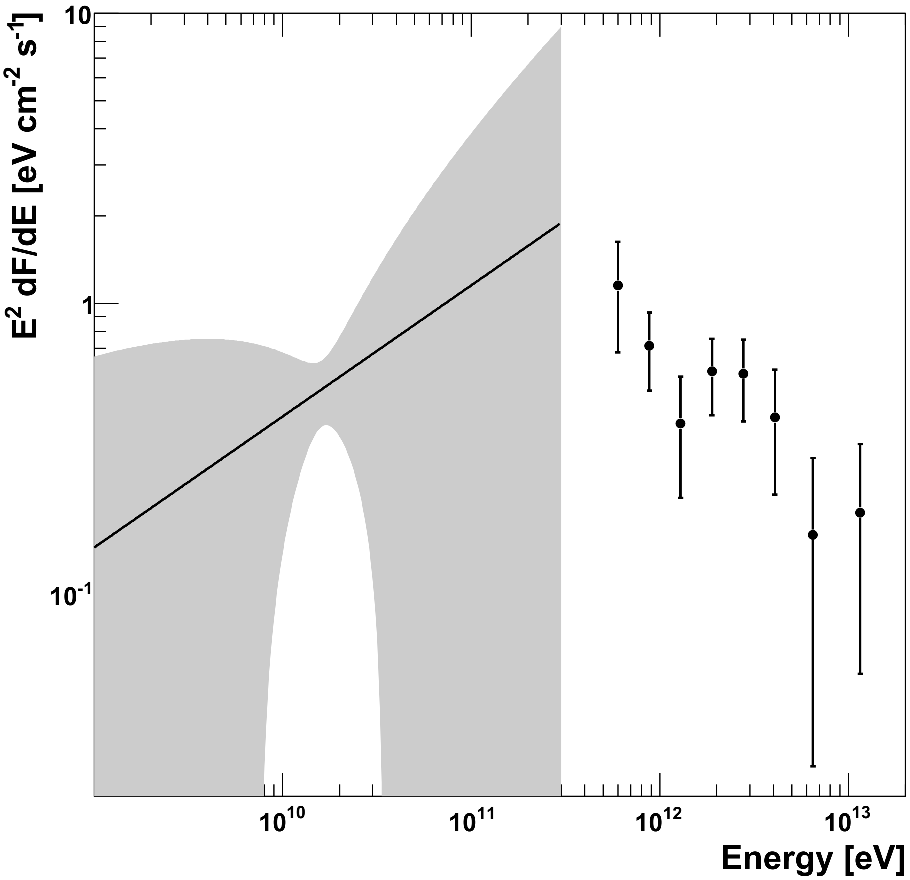

Figure 6.9: Total observed gamma-ray spectrum of 1ES 0229+200, including the HESS data points from Aharonian et al. (2007) and the *Fermi* best-fit spectrum (solid line) and confidence band (shaded region). The band is quite large because this source is very weakly detected.

the confidence band is quite large.

In Figure 6.10, I summarize the results from our halo search in the vicinity of 1ES 0229+200. In this case, although the best-fit cutoff energy is well within our search region, for low values of the EGMF strength, the spectral index reaches the lower bound of the parameter space, nearing a value of 1.1. In the optimum case, we should expand our search space to even harder values of the spectrum. As a practical matter, however, a spectral index of 1.1 is already much harder than conventional one-zone synchrotron self Compton (SSC) models for blazar gamma-ray production (Aharonian, 2001). Our results are therefore reasonable if the production of gamma rays by 1ES 0229+200 proceeds via this conventional mechanism. However, it may be fruitful to investigate the results from even harder spectra,

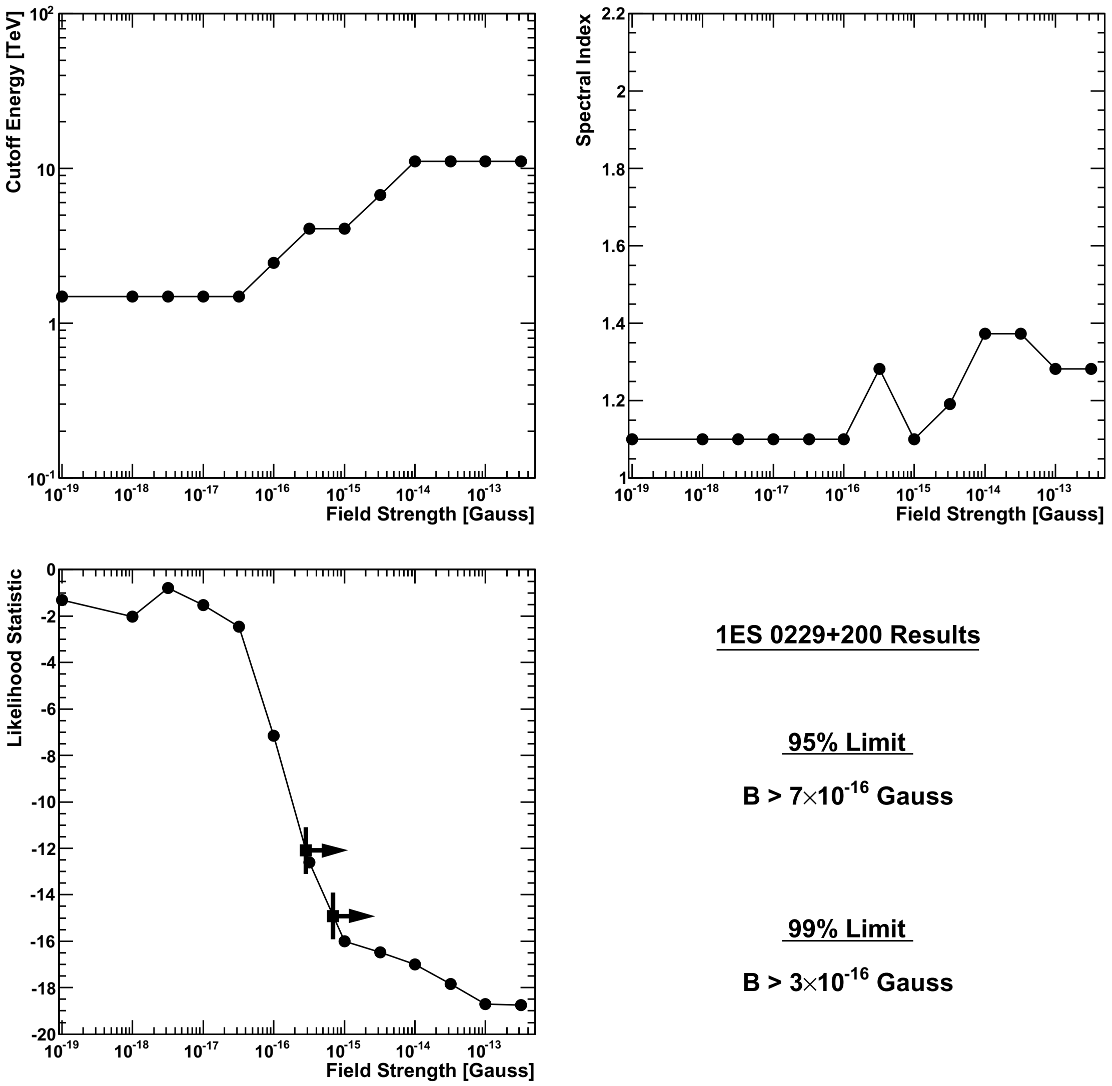

Figure 6.10: Summary of the results from the analysis of 1ES 0229+200. The description of the plots is the same as in Figure 6.1.

such as those permitted by the models of Böttcher et al. (2008) and Tavecchio et al. (2009). I leave this topic for a future study.

As shown in Figure 6.10, at 95% confidence we achieve the same lower limit on the field strength from 1ES 0229+200 that we did from RGB J0710+591. The results are then not only consistent; they also present the optimum situation for a combination of the two likelihood statistic curves. Additionally, the curve for 1ES 0229+200 admits a 99% confidence limit of $B > 3 \times 10^{-16}$ Gauss, due to the high confidence of rejection of the models with

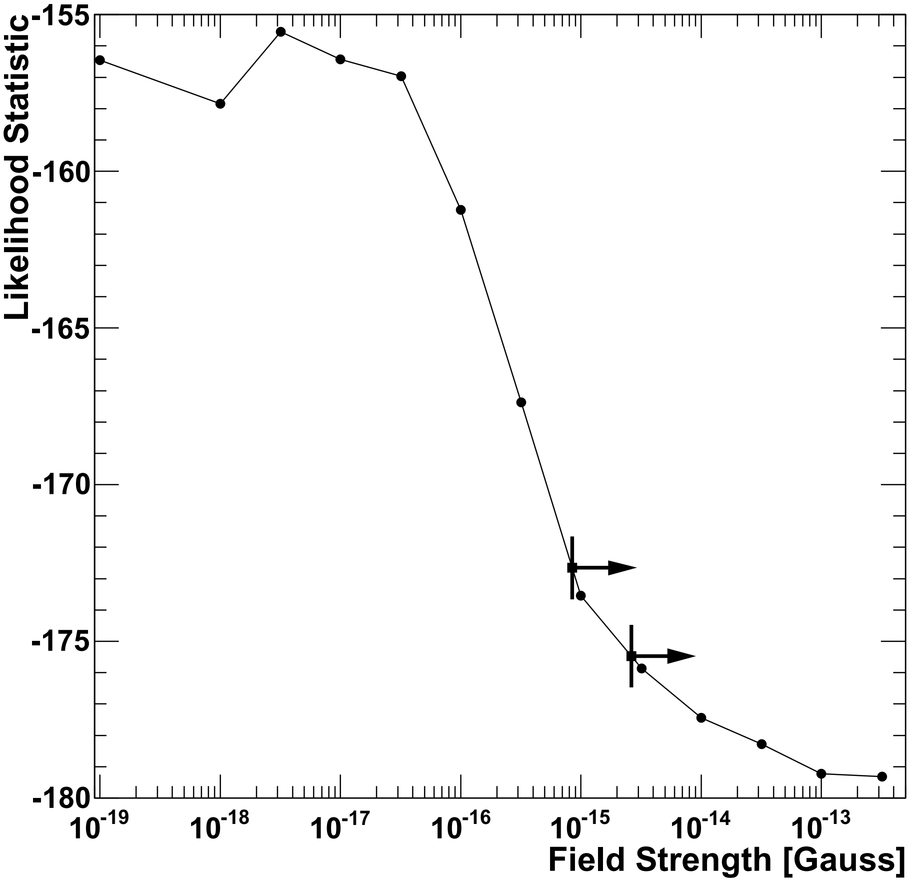

Figure 6.11: The combined likelihood statistic curve from the analysis of RGB J0710+591 and 1ES 0229+200.

low field strengths. However, these limits should be considered carefully since it relies on the rejection of spectral indices greater than 1.1 on the grounds that they are unphysical, and this justification may not hold up against some less conventional models going beyond the standard one-zone SSC model, such as those highlighted by Böttcher et al. (2008) and references therein.

6.4.3 Combined Limit

Because we can multiply likelihoods, it is a straightforward matter to combine the results of Figure 6.8 and Figure 6.10: we simply add the likelihood statistic curves. The summed curve appears in Figure 6.11, from which at 95% confidence we derive a robust lower limit on the EGMF strength of $B > 3 \times 10^{-15}$ Gauss. At 99% confidence, this limit becomes

$B > 8 \times 10^{-16}$ Gauss. Both of the blazars studied in this chapter show evidence that the expected halo of gamma rays in the energy range accessible to *Fermi* does not exist. This evidence is strengthened by the combination of the data from the analysis of each blazar individually.

CHAPTER 7

STRONG EXTRAGALACTIC MAGNETIC FIELDS

That the EGMF is strong is one possible interpretation of the analysis presented in this study. Certainly it is a compelling one. While at first it may seem surprising to find magnetic fields present where there is very little matter, the mechanisms proposed to generate them are based on established physics. In this chapter, I first consider the interpretation of the absence of any detectable halo, demonstrated by the analysis presented in this work, as being due to the presence of a strong EGMF. I then conclude with a few remarks on prospects for the future.

7.1 Interpretation of the Results

The astrophysical origin hypothesis, that the EGMF is generated by bulk outflows of magnetized material from radio galaxies (Kronberg, 1994; Kronberg et al., 2001), suffers only from the difficulty of filling a large fraction of the universe with magnetic fields without injecting a large mass along with them. Energetically, this process is trivial: the total amount of energy in the EGMF throughout every region in the observable universe is less than the magnetic energy contained in a single cluster as long as the EGMF strength is below 10^{-12} Gauss. However, the bulk transport of plasma into the voids is another matter entirely. Although such mechanisms could plausibly produce the observed intracluster fields, it may indeed be "downright hopeless," as Zweibel (2006) claims, for them to fill the voids. Since Dolag et al. (2011) have pointed out that the gamma-ray cascades are sensitive to the dominant component of the EGMF in the voids, the astrophysical origin mechanism may be disfavored by the detection of a strong EGMF. However, it may be possible for these processes to operate at earlier times, when the volume of the voids was smaller, or even prior to void formation, if there are sufficient numbers of active or starburst galaxies at $z \approx 6$ (Kronberg et al., 1999).

Perhaps a more likely candidate for the generation of the EGMF can be found in the primordial origin hypothesis, in which the EGMF is generated during phase transitions in the early universe. In this scenario, there are two main difficulties. First, the magnetic field must be generated with strength sufficient to avoid being diluted by the universal expansion to a present-day strength lower than the 10^{-15}-Gauss levels suggested by this analysis, while still being weak enough not to produce an observable anisotropic effect on that expansion. Models overcoming this difficulty do exist, although they require a degree of fine tuning to produce situations amendable to the standard Biermann battery mechanism (Grasso & Rubinstein, 2001), for example. The second difficulty is that the EGMF must survive to the present day without decaying due to magnetic diffusion. As shown in Figure 1.1, this requirement is not particularly stringent because the range of allowed correlation lengths is quite broad.

If the EGMF is primordial, then its strength is very compelling in the context of magnetic field generation due to differential rotation in galaxies, the α-ω dynamo mechanism. Although the dynamo efficiency is not well known, studies suggest that it can produce the magnetic fields observed in galaxies if the seed EGMFs lie above the very loose lower bound of $\sim 10^{-30}$ Gauss (Widrow, 2002). However, due to the existence of magnetic fields detected in galaxies at a redshift as distant as $z = 2$ Bernet et al. (2008), the seed fields may need to be much stronger because there are only a few cycles of galactic rotation during which the dynamo can operate, due to the limited amount of time since galaxy formation. Widrow (2002) notes that the lower bound may become much more constraining, falling somewhere in the range from 10^{-16} to 10^{-10} Gauss. The results of this work, which conclude that the EGMF may be rather strong, therefore can be taken as evidence in support of the α-ω dynamo theory of galactic magnetic field formation.

The ultra-high-energy cosmic rays (UHECRs), with energies above 10^{19} eV, are believed to be of extragalactic origin and are therefore influenced by the EGMF. In order to deflect the UHECRs significantly from their sources, the EGMF must be relatively strong, possibly even stronger than the lower limits suggested in this work. The degree of deflection is also related to the correlation length because for smaller correlation lengths the UHECRs' directions undergo a random walk as they cross EGMF domains. However, the same is true for the electrons in the cascade, and a smaller correlation length would imply an even more constraining lower limit on the field strength. This limit can be estimated via Equation 4.12.

Alternative interpretations of the absence for the halo also exist. Instrumental systematic errors are one possible explanation for our results. For instance, we rely on the accuracy of the P7SOURCE_V6 model of the instrument response functions for the *Fermi* LAT. If this model describes a broader PSF than the true PSF of the instrument, the effects of the halo could be obscured in the likelihood fit. Indeed, this exact problem arose with a previous model of the *Fermi* IRFs, P6_V3, for which Ando & Kusenko (2010) claimed a detection of the EGMF that was later shown to be most likely due to an instrumental effect (Neronov et al., 2011). The P7SOURCE_V6 model is derived from actual observations of what are assumed to be point sources, many of which may be blazars. It is possible that the halo could be incorporated into the model, obscuring the true signal. However, this is unlikely provided that the sources used in constructing the model are predominantly Galactic sources and nearby blazars lacking a strong TeV component. A finalized model of the *Fermi* LAT based on both observations and simulations is forthcoming. When this new model is available, we can improve the confidence in our results by using it in place of the P7SOURCE_V6 model.

Our analysis also depends on the assumptions we have made regarding the flaring activity of the blazar. The IACT observations are likely to be biased because the IACTs are more likely to point toward a blazar if it is determined to be in a flaring state. This issue can be remedied by performing unbiased observations on a selection of blazars likely to provide good limits on the EGMF. Dedicated observations by the existing IACTs or by the future Cherenkov Telescope Array (CTA) could accomplish these observations. Additionally, the High Altitude Water Cherenkov (HAWC) experiment, which will soon be operational, will provide continuous unbiased observations of many blazars now seen by the existing IACTs.

A more problematic assumption to overcome is that the blazars have been active for a period of time sufficiently long for the cascade to reach a steady state. If the field is as strong as 10^{-15} Gauss, then this time is on the order of 10^{6} years. Observations over this time scale are presently unavailable and will remain so for the foreseeable future. For this reason, a positive detection of the halo would be significant because it would provide confirmation that the blazar engines may be active for long periods of time. Since such a positive detection appears inaccessible to the *Fermi* instrument, we expect that the halo may become visible at energies accessible to the IACTs or CTA. However, in these cases, a high cutoff energy is needed to ensure that there is substantial cascade in the TeV energy range to produce a halo in the first place. The trends of increasing cutoff energy with field strength in Figures 6.8 and 6.10 are somewhat encouraging, but since the focus in these figures was on the EGMF strength, we can make no strong statistical statements about the true values of the cutoff energies. Nevertheless, a search for a TeV-scale halo in the 10^{-14} to 10^{-12} Gauss range may prove fruitful, and indeed could shed light on the question of the lifetime of blazar engines.

Broderick et al. (2011) have suggested that the absence of the halo could be due to the development of plasma instabilities in the interactions between the electrons and positrons in the cascade and the electrons in the intergalactic medium (IGM). For particularly strong blazars, the ratio of the density in the cascade to the density of the IGM becomes sufficiently large to trigger plasma instabilities operating on time scales shorter than the cooling time of the electrons via inverse Compton scattering. Such a process could dissipate the energy in the cascade into modes in the IGM, effectively destroying the halo before it has a chance to form. However, the calculations presented by Broderick et al. (2011) are dependent on the extrapolation of results from Bret et al. (2010) to extremely low density ratios, and it is unclear that the plasma approximations still hold. The time scale over which the plasma instabilities reach steady state is also uncertain. Regardless, the topic of plasma instabilities in the cascade is an intriguing idea that should be explored further in the future.

Two other theories have been advanced that would complicate the interpretation of the halo if it were detected. In more conventional terms, Essey & Kusenko (2010) pointed out that blazars may be sources of cosmic-ray nuclei in the energy range from 10^{16} to 10^{19} eV. These cosmic rays can interact with the EBL via the Δ resonance, producing pions that decay to gamma rays at the TeV scale. Since the cross section for this interaction is quite low, a small number of the cosmic rays can interact nearby Earth, producing TeV-scale gamma rays that appear to come from blazars too distant to be compatible with even the lower bounds on the EBL. If this process occurs, then the EGMF can be limited from above as well as below based on the observations of distant blazars, since if the EGMF is too strong then the cosmic rays will be deflected away from their sources and the correlation with the source would be destroyed. It is unclear, however, to what degree the stronger fields in the LSS affect the cosmic rays' trajectories. Unlike in the case of the electron-positron cascades, which are affected by the dominant component of the EGMF only, the cosmic rays are strongly affected by all fields along their trajectory, and their passage through a single cluster or filament could be enough to destroy the correlation with the source. Additionally, the total flux of cosmic rays observed at Earth can be used to place limits on the number of blazars that generate cosmic rays. A detailed study of this effect has yet to be undertaken.

Work by de Angelis et al. (2009) suggests a less conventional theory that the existence of axion-like particles (ALPs) could contribute to the detection of distant blazars. If such particles exist, then gamma rays can convert to ALPs in the magnetic field local to the source blazar, travel unimpeded by the EBL until they are relatively nearby, and convert back to gamma rays in the magnetic field of the Galaxy. While primarily theoretical, the existence of ALPs could affect the conclusions from our halo search, although the precise nature of their influence is presently unclear.

Finally, an investigation of the timing information available in the gamma-ray data could provide better limits on the EGMF. Since the cascade cannot show variability on short time scales, the observed variability in the *Fermi* energy band must be intrinsic to the source. We can set better limits by taking this information into account in our fits. Additionally, if the EGMF is weak because the blazar lifetimes are actually short, it may prove fruitful to search for the characteristic time delays that are expected to follow the flares. As suggested by Figure 5.25, the detection of such delays could provide direct evidence for an EGMF with a strength below $\sim 10^{-17}$ Gauss.

7.2 Prospects for the Future

The analysis presented in this work is one of many avenues of research available to increase our understanding of magnetic fields in the universe. There are several ways in which it could be improved. As demonstrated in Section 6.4.3, the most straightforward way of improving the results could be to combine the likelihood curves from several blazars. Alternatively, studying an individual blazar whose properties are well measured would eliminate our dependence on certain assumptions about the values of those properties. For instance, if the bulk Lorentz factor or viewing angle can be measured, we can use those values instead of the assumptions that we make in this study. Working to characterize the dependence of the conclusions on the uncertain lifetime of the blazars could also prove enlightening, and it may be possible to make better constraints by associating only steady *Fermi* measurements with the cascade.

The time is ripe for further investigations into the nature of the EGMF. As mentioned in the previous section, there are many avenues of investigation still open to improve our knowledge of the EGMF and enhance our understanding of the inner workings of blazars. With new instruments being built to study the TeV sky, and with the existing operational IACTs and the *Fermi* LAT, we are living in a golden age of gamma-ray astrophysics. It is essential that we make the best use that we can of these opportunities. As we narrow in on a better understanding of what the most extreme existing accelerators can teach us, ultimately we will learn more about the fascinating universe of which we are a small part.

APPENDIX A
EQUATIONS OF MOTION IN COMOVING COORDINATES

Particle tracking in a three-dimensional expanding space requires a careful selection of coordinates. We assume an FLRW cosmology with a metric specified by

$$ds^2 = c^2 dt^2 - R^2(t) d\vec{x}^2, \tag{A.1}$$

where $R(t)$ is the scale factor at cosmic time t. It is convenient to track the particles in terms of the redshift $z(t)$, which is defined in terms of the present-day scale factor $R(t_0)$ as

$$1 + z(t) = \frac{R(t_0)}{R(t)}. \tag{A.2}$$

The conversion between cosmic time and redshift is accomplished via the Hubble formula

$$H(t) = \frac{1}{R(t)} \frac{d}{dt} R(t) \tag{A.3}$$

by using the equation

$$\frac{dz}{dt} = -H(z)(1+z). \tag{A.4}$$

For an FLRW universe, $H(z)$ is given by

$$H(z) = H_0 \sqrt{\Omega_R (1+z)^4 + \Omega_M (1+z)^3 + \Omega_\Lambda + (1 - \Omega_C)(1+z)^2}, \tag{A.5}$$

where Ω_R, Ω_M, Ω_Λ, and Ω_C are respectively the radiation, matter, cosmological constant, and curvature densities in units of the critical density ρ_C. We assume that the Hubble parameter H_0 is 70 km/s/Mpc.

A.1 Particle Dynamics

Freely propagating particles follow geodesics given by

$$\frac{d^2 x^\mu}{d\lambda^2} + \Gamma^\mu_{\nu\rho} \frac{dx^\nu}{d\lambda} \frac{dx^\rho}{d\lambda} = 0, \tag{A.6}$$

where

$$\Gamma^{\mu}_{\nu\rho} = \frac{1}{2} g^{\mu\sigma} \left(\frac{\partial g_{\sigma\nu}}{\partial x^{\rho}} + \frac{\partial g_{\sigma\rho}}{\partial x^{\nu}} - \frac{\partial g_{\nu\rho}}{\partial x^{\sigma}} \right) \tag{A.7}$$

are the Christoffel symbols in terms of the metric $g^{\mu\nu}$ and λ is an affine parameter that characterizes the trajectory (Wald, 1984). The only nonzero Christoffel symbols for an FLRW cosmology are

$$\Gamma^{t}_{ii} = R\dot{R} \tag{A.8}$$

and

$$\Gamma^{i}_{it} = \Gamma^{i}_{ti} = \frac{\dot{R}}{R} \tag{A.9}$$

where t denotes the time direction and i and j denote spatial directions. The dot indicates the derivative with respect to cosmic time t. Using these Christoffel symbols and applying proper time τ as our affine parameter, we express Equation A.6 in comoving coordinates r^i as

$$\frac{d^2 r^i}{d\tau^2} + 2\frac{\dot{R}}{R}\frac{dr^i}{d\tau}\frac{dt}{d\tau} = 0. \tag{A.10}$$

The physical position of the particle at redshift z is obtained by multiplying the comoving position $\vec{r}$ by the scale factor $R(z)$.

Recognizing that the comoving momentum is

$$p^i = m\frac{dr^i}{dt} \tag{A.11}$$

and $\gamma = dt/d\tau$ is the Lorentz factor of the particle, we can rewrite Equation A.10 in terms of p^i and t as

$$\frac{dp^i}{dt} + 2\frac{\dot{R}}{R}p^i = 0 \tag{A.12}$$

The physical momentum ${p_p}^i$ of the particle, which enters into the inverse Compton, pair production, and Lorentz force calculations, should be measured in the Minkowski spacetime instantaneously tangent to the particle's position in spacetime. The time evolution of the scale factor is then irrelevant, and since the momentum is proportional to the time derivative of the position, we simply scale the comoving momentum by the scale factor to get the physical momentum

$${p_p}^i = R(t)p^i. \tag{A.13}$$

We then take the time derivative of ${p_p}^i$ and use Equation A.12 to get

$$\frac{d{p_p}^i}{dt} = -\frac{\dot{R}}{R}{p_p}^i. \tag{A.14}$$

The redshift evolution is then obtained by applying Equation A.4:

$$\frac{d}{dz}\vec{p}_p = \frac{\vec{p}_p}{1+z}, \tag{A.15}$$

and the solution to this equation gives the familiar expression

$$\vec{p}_p(z) = \frac{1+z}{1+z_0}\vec{p}_p(z_0). \tag{A.16}$$

We arrive at a similar equation for the evolution of the comoving position. If we adopt the convention to measure distances in terms of the present-day scale factor, then $R(t_0) = 1$ and by using Equation A.11 in conjunction with Equation A.13, we find that

$$\frac{d}{dt}\vec{r} = \frac{c(1+z)}{mc^2\gamma}\vec{p}_p(z) = (1+z)c\vec{\beta}(z), \tag{A.17}$$

where $c\vec{\beta}(z)$ is the velocity of the particle, and with the help of Equation A.4, we obtain

$$\frac{d}{dz}\vec{r} = -\frac{c}{mc^2\gamma H(z)}\vec{p}_p(z) = -\frac{c\vec{\beta}(z)}{H(z)}. \tag{A.18}$$

Although we have derived Equations A.15 and A.18 by using the proper time τ as the affine parameter, the final equations are independent of τ and are applicable to massless particles such as gamma rays.

A.2 Linear Motion

Several of the Monte Carlo simulation tests described in Section 5.1.3 rely on analytical calculations of particle motion in one dimension. These equations are derived in this section. To assess the error on the momentum tracking, for instance, we simply use Equation A.16. Solving Equation A.18 is more difficult, however, because of the presence of $H(z)$. For simplicity, we adopt a constant-dominated flat universe so that $H(z) = H_0$. In one dimension, Equation A.18 then becomes

$$\frac{dx}{dz} = -\frac{c\beta(z)}{H_0}. \tag{A.19}$$

We can express $\beta(z)$ in terms of the variable $q = p_0/mc^2$, where p_0 is the present-day momentum of the particle, as

$$\beta(z) = \left(1 + \frac{1}{q^2(1+z)^2}\right)^{-1/2}. \tag{A.20}$$

In the nonrelativistic limit, $q << 1$ and Equation A.20 can be approximated by

$$\beta_{\mathrm{NR}}(z) = q(1+z). \tag{A.21}$$

In this limit the solution to Equation A.19 for a particle propagating from redshift z_i to redshift z is

$$x_{\mathrm{NR}}(z) = \frac{qc}{2H_0}\left[(1+z_i)^2 - (1+z)^2\right]. \tag{A.22}$$

In the highly relativistic regime, $q >> 1$ and the approximation for Equation A.20 becomes

$$\beta_{\mathrm{HR}}(z) = 1 - \frac{1}{2y^2(1+z)^2}. \tag{A.23}$$

This alters the solution of Equation A.19 to

$$x_{\mathrm{HR}}(z) = \frac{c}{H_0}\left[(z_i - z) - \frac{1}{2q^2}\left(\frac{1}{1+z_i} - \frac{1}{1+z}\right)\right]. \tag{A.24}$$

The time delay of cascade particles relative to a gamma ray that propagates directly from the source may be of interest, for example, for characterizing the light curves of flares. The time for a particle to propagate a distance dx along the radial direction can be expressed via Equation A.17 as

$$dt = \frac{dx}{c\beta(z)(1+z)\cos\theta}. \tag{A.25}$$

Here, θ is the angle between the particle's direction and the radial direction. If the equivalent redshift of the radial gamma ray at the particle's spacetime position is $z_r(z)$, then the time delay $d\Delta t$ acquired in propagating through radial distance dx is the difference between dt

for the particle and $dt_r = dx/c(1+z_r)$ for the radial photon. We can therefore write

$$\frac{d\Delta t}{dt} = \frac{\frac{dx}{c\beta(z)(1+z)\cos\theta} - \frac{dx}{1+z_r(z)}}{\frac{dx}{c\beta(z)(1+z)\cos\theta}} = 1 - c\beta(z)\cos\theta\frac{1+z}{1+z_r(z)}, \tag{A.26}$$

which in terms of redshift is

$$\frac{d\Delta t}{dz} = -\frac{1}{(1+z)H(z)} + \frac{c\beta(z)\cos\theta}{(1+z_r(z))H(z)}. \tag{A.27}$$

In one dimension, $\cos\theta = 1$ and the time delay arises solely due to the effects of particle mass. Making this assumption and further simplifying Equation A.27 by assuming a constant-dominated universe, we arrive at

$$H_0\frac{d\Delta t}{dz} = -\frac{1}{1+z} + \frac{\beta(z)}{1+z_r(z)}. \tag{A.28}$$

It is evident that we require an expression for $z_r(z)$. This we straightforwardly obtain from

$$\begin{aligned}\frac{dz_r}{dz} =& \frac{dz_r}{dt_r}\frac{dt_r}{dt}\frac{dt}{dz} = ((1+z_r)H(z_r))\left(c\beta(z)\cos\theta\frac{1+z}{1+z_r}\right)\left(-\frac{1}{(1+z)H(z)}\right)\\ =& -\frac{H(z_r)}{H(z)}c\beta(z)\cos\theta.\end{aligned} \tag{A.29}$$

Again working in a constant-dominated cosmology, we find the ratio of Hubble expressions drops out of Equation A.29. The assumption of one-dimensional motion eliminates the $\cos\theta$, and in the nonrelativistic limit of Equation A.21 we obtain the solution

$$z_r(z) = z_i + \frac{q}{2}\left[(1+z_i)^2 - (1+z)^2\right]. \tag{A.30}$$

By inserting this into Equation A.28 and solving, we find

$$H_0\Delta t(z) = \ln\left(\frac{(1+z_i)^2}{(1+z)(1+z_y+\frac{q}{2}\left[(1+z_i)^2-(1+z)^2\right]}\right). \tag{A.31}$$

While the Monte Carlo code explicitly solves Equations A.17 and A.26 via the methods described in Section 5.1.3, we use the simple cases specified by Equations A.24 and A.31 to verify its accuracy.

A.3 Electromagnetic Fields

The presence of a magnetic field deflects charged particles away from the geodesic of Equation A.6. Following Jackson (1999) but inverting the sign of his metric to maintain consistency with the previous sections, we write the covariant Lorentz force equation as

$$\frac{dp_\mu}{d\tau} = qF_{\mu\nu}\frac{dx^\nu}{d\tau}, \tag{A.32}$$

where the electromagnetic tensor $F_{\mu\nu}$ generalizes in the FLRW cosmology to

$$F_{\mu\nu} = (\partial_\mu A_\nu - \Gamma^\rho_{\mu\nu}A_\rho) - (\partial_\nu A_\mu - \Gamma^\rho_{\nu\mu}A_\rho) = \partial_\mu A_\nu - \partial_\nu A_\mu, \tag{A.33}$$

and A_ν is the electromagnetic four-potential.

The equations of motion are a linear superposition of Equation A.32 with the covariant geodesic equation. Starting from Equation A.6, we multiply by $g_{\mu\sigma}$ and write

$$\frac{d(g_{\mu\sigma}p^\mu)}{d\tau} - p^\mu\frac{dg_{\mu\nu}}{d\tau} + \Gamma^\mu_{\nu\rho}p^\nu\frac{dx^\rho}{d\tau}g_{\mu\sigma} = 0. \tag{A.34}$$

Using the vanishing of the metric tensor under the total covariant derivative, we see that

$$\frac{dg_{\nu\rho}}{d\tau} = g_{\sigma\rho}\Gamma^\sigma_{\nu\mu}\frac{dx^\mu}{d\tau} + g_{\nu\sigma}\Gamma^\sigma_{\rho\mu}\frac{dx^\mu}{d\tau}, \tag{A.35}$$

and by inserting this into Equation A.34, we find

$$\frac{dp_\sigma}{d\tau} - p^\mu g_{\lambda\sigma}\Gamma^\lambda_{\mu\gamma}\frac{dx^\gamma}{d\tau} - p^\mu g_{\mu\lambda}\Gamma^\lambda_{\sigma\gamma}\frac{dx^\gamma}{d\tau} + \Gamma^\mu_{\nu\rho}p^\nu\frac{dx^\rho}{d\tau}g_{\mu\sigma} = 0. \tag{A.36}$$

The second and fourth terms in Equation A.36 cancel. After renaming dummy indices, we arrive at the covariant equations of motion

$$\frac{dp_\mu}{d\tau} = \Gamma^\rho_{\mu\nu}p_\rho\frac{dx^\nu}{d\tau}. \tag{A.37}$$

The total equations of motion are then

$$\frac{dp_\mu}{d\tau} = \Gamma^\rho_{\mu\nu}p_\rho\frac{dx^\nu}{d\tau} + qF_{\mu\nu}\frac{dx^\nu}{d\tau}. \tag{A.38}$$

It is now our task to turn Equation A.38 into something useful for particle tracking. Adopting an FLRW cosmology, we start with

$$\frac{dp_i}{d\tau} = R\dot{R}p_t\frac{dx^i}{d\tau} + \frac{\dot{R}}{R}p_i\gamma + qF_{ij}\frac{dx^j}{d\tau} + q\gamma F_{it}. \tag{A.39}$$

Converting the derivative to cosmic time t and rearranging terms gives us

$$\frac{dp_i}{dt} = -\dot{R}Rp^i + \frac{\dot{R}}{R}p_i + \frac{q}{m\gamma}F_{ij}p^j + qF_{it}. \tag{A.40}$$

We know that $p_i = g_{ii}p^i = R^2p^i$, so in terms of the physical momentum ${p_p}^i$, we have $p_i = R{p_p}^i$. Rewriting Equation A.40 in terms of the physical momentum gives us

$$\frac{d{p_p}^i}{dt} = -\frac{\dot{R}}{R}{p_p}^i + \frac{q}{m\gamma R^2}F_{ij}{p_p}^j + \frac{q}{R}F_{it}. \tag{A.41}$$

Specializing to the case of no electric field and a constant comoving magnetic field $\vec{B}_0 = R^2\vec{B}(z)$, we get the final equation of motion

$$\frac{d}{dt}\vec{p}_p = -H(z)\vec{p}_p + \frac{q}{m\gamma}\vec{p}_p \times \vec{B}(z). \tag{A.42}$$

APPENDIX B
MEAN FREE PATH SAMPLING FOR CONTINUOUS ENERGY LOSSES

Due to processes such as redshift that cause propagating particles to lose energy continuously, the mean free path for the particle at the beginning of its trajectory may be different from that at the end. For this reason, sampling the interaction distance from the original mean free path may give an incorrect result. I describe our solution to this problem in this section.

In the general case, the mean free path $\lambda(L)$ will be a function of the position L of the particle. The probability of survival for a particle traveling from position L_1 to position L_2 is then

$$P(L_1 \to L_2) = \exp\left(-\int_{L_1}^{L_2} \frac{dL'}{\lambda(L')}\right). \tag{B.1}$$

Let $\lambda_0 \leq \lambda(L)$ for all L. We make the claim that if we sample an interaction distance $L_I - L_1$ from an assumed mean free path λ_0, propagate the particle from L_1 to L_I, and cause it to interact with probability $\lambda_0/\lambda(L_I)$, then the particle's behavior will fulfill Equation B.1 in a statistical sense. We now seek to demonstrate that this is true.

If the sampled position L_I is beyond the maximum propagation point L_2, then the probability P_0 for survival with 0 chances to interact is obviously

$$P_0(L_1 \to L_2) = \exp\left(-\frac{L_2 - L_1}{\lambda_0}\right), \tag{B.2}$$

which fulfills

$$\frac{dP_0(L_1 \to L_2)}{dL_2} = -\frac{1}{\lambda_0}\exp\left(-\frac{L_2 - L_1}{\lambda_0}\right) = -\frac{P_0(L_1 \to L_2)}{\lambda_0}. \tag{B.3}$$

If the sampled value $L_I - L_1$ is less than $L_2 - L_1$, then according to our prescription the particle will survive the interaction with probability $1 - \lambda_0/\lambda(L_I)$. We can then write the probability to survive with one chance to interact P_1 as

$$dP_1(L_1 \to L_2) = \left(-\frac{dP_0(L_1 \to L_I)}{dL_I}dL_I\right)\left(1 - \frac{\lambda_0}{\lambda(L_I)}\right)P_0(L_I \to L_2), \tag{B.4}$$

where the first term on the right hand side represents the probability that the first interaction occurs at is L_I, the second term implements our survival prescription, and the third term is the probability for the particle to survive its propagation from L_I to L_2 with no additional interactions triggered. Replacing the first term with the result from Equation B.3 and the third term with that from Equation B.2 and integrating, we find

$$P_1(L_1 \to L_2) = \int_{L_1}^{L_2} dL_I \left[\exp\left(-\frac{L_I - L_1}{\lambda_0}\right)\right] \left(\frac{1}{\lambda_0} - \frac{1}{\lambda(L_I)}\right) \exp\left(-\frac{L_2 - L_I}{\lambda_0}\right), \tag{B.5}$$

which simplifies to

$$P_1(L_1 \to L_2) = \exp\left(-\frac{L_2 - L_1}{\lambda_0}\right) \int_{L_1}^{L_2} dL_I \left(\frac{1}{\lambda_0} - \frac{1}{\lambda(L_I)}\right). \tag{B.6}$$

Taking the derivative of this equation with respect to L_2 gives us

$$\frac{dP_1(L_1 \to L_2)}{dL_2} = -\frac{1}{\lambda_0} P_1(L_1 \to L_2) + \exp\left(-\frac{L_2 - L_1}{\lambda_0}\right) \left(\frac{1}{\lambda_0} - \frac{1}{\lambda(L_2)}\right), \tag{B.7}$$

and we see from Equation B.2 that this can be expressed as

$$\frac{dP_1(L_1 \to L_2)}{dL_2} = -\frac{P_1(L_1 \to L_2)}{\lambda_0} + \frac{P_0(L_1 \to L_2)}{\lambda_0} - \frac{P_0(L_1 \to L_2)}{\lambda(L_2)}. \tag{B.8}$$

In the general case, let us assume that we have $n+1$ candidate positions for interactions, all of which fail to interact according to our prescription. We can write the differential survival probability for this case when the first interaction occurs at position L_I as

$$dP_{n+1}(L_1 \to L_2) = \left(\frac{-dP_0(L_1 \to L_I)}{dL_I} dL_I\right) \left(1 - \frac{\lambda_0}{\lambda(L_I)}\right) P_n(L_I \to L_2). \tag{B.9}$$

Integrating to get the total interaction probability, we find

$$P_{n+1}(L_1 \to L_2) = \int_{L_1}^{L_2} dL_I \left[\exp\left(-\frac{L_I - L_1}{\lambda_0}\right)\right] \left(\frac{1}{\lambda_0} - \frac{1}{\lambda(L_I)}\right) P_n(L_I \to L_2). \tag{B.10}$$

If we differentiate Equation B.10 with respect to L_2, there are two terms. One of these is proportional to $P_n(L_2 \to L_2)$, which by Equation B.10 vanishes for $n > 0$. The second term gives us

$$\begin{aligned}\frac{dP_{n+1}(L_1 \to L_2)}{dL_2} = &-\int_{L_1}^{L_2} dL_I \left[-\exp\left(-\frac{L_I - L_1}{\lambda_0}\right)\right]\left(\frac{1}{\lambda_0} + \frac{1}{\lambda(L_I)}\right) \times \\ &\times \frac{dP_n(L_I \to L_2)}{dL_2}.\end{aligned} \tag{B.11}$$

Inspired by Equation B.8, let us make the assumption that

$$\frac{dP_n(L_1 \to L_2)}{dL_2} = -\frac{P_n(L_1 \to L_2)}{\lambda_0} + \frac{P_{n-1}(L_1 \to L_2)}{\lambda_0} - \frac{P_{n-1}(L_1 \to L_2)}{\lambda(L_2)}. \tag{B.12}$$

Plugging this into Equation B.11 gives us

$$\begin{aligned}\frac{dP_{n+1}(L_1 \to L_2)}{dL_2} = &\int_{L_1}^{L_2} dL_I \left[-\exp\left(-\frac{L_I - L_1}{\lambda_0}\right)\right]\left(\frac{1}{\lambda_0} - \frac{1}{\lambda(L_I)}\right) \times \\ &\times \left(-\frac{P_n(L_1 \to L_2)}{\lambda_0} + \frac{P_{n-1}(L_1 \to L_2)}{\lambda_0} - \frac{P_{n-1}(L_1 \to L_2)}{\lambda(L_2)}\right).\end{aligned} \tag{B.13}$$

The integrals can be evaluated using Equation B.10, giving

$$\frac{dP_{n+1}(L_1 \to L_2)}{dL_2} = -\frac{P_{n+1}(L_1 \to L_2)}{\lambda_0} + \frac{P_n(L_1 \to L_2)}{\lambda_0} - \frac{P_n(L_1 \to L_2)}{\lambda(L_2)} \tag{B.14}$$

Equation B.12 is therefore valid by induction.

The total probability of survival with any number of interactions is

$$P(L_1 \to L_2) = \sum_{n=0}^{\infty} P_n(L_1 \to L_2). \tag{B.15}$$

Obviously,

$$\frac{dP(L_1 \to L_2)}{dL_2} = \sum_{n=0}^{\infty} \frac{dP_n(L_1 \to L_2)}{dL_2}. \tag{B.16}$$

We can plug Equation B.12 it into Equation B.16 to get

$$\begin{aligned}\frac{dP(L_1 \to L_2)}{dL_2} = &-\sum_{n=0}^{\infty} \frac{P_n(L_1 \to L_2)}{\lambda_0} + \sum_{n=1}^{\infty} \frac{P_{n-1}(L_1 \to L_2)}{\lambda_0} - \\ &- \sum_{n=1}^{\infty} \frac{P_{n-1}(L_1 \to L_2)}{\lambda(L_2)}.\end{aligned} \tag{B.17}$$

The first and second sums in Equation B.17 cancel. The third sum over the probability is just the total probability of surviving given any number of proposed interactions. Equation B.17 therefore reduces to

$$\frac{dP(L_1 \to L_2)}{dL_2} = -\frac{P(L_1 \to L_2)}{\lambda(L_2)} \tag{B.18}$$

the solution to which is Equation B.1. This demonstrates that our prescription delivers the expected behavior for the particle.

APPENDIX C

GLOSSARY OF TLAS AND TMLAS

Acronym	**Description**
AGN	Active Galactic Nucleus
ARGO-YBJ	Astrophysical Radiation with Ground-based Observatory at Yangbajing
BBN	Big-Bang Nucleosynthesis
COBE	Cosmic Background Explorer
CMB	Cosmic Microwave Background
DIRBE	Diffuse Infrared Background Experiment
EBL	Extragalactic Background Light
EGMF	Extragalactic Magnetic Field
HAWC	High-Altitude Water Cherenkov telescope
HBL	High-frequency-peaked Bl Lacertae Object
HESS	High-Energy Stereoscopic System
IACT	Imaging Atmospheric Cherenkov Telescope
IBL	Intermediate-frequency-peaked Bl Lacertae Object
IGM	Intergalactic Medium
ISO	Infrared Space Observatory
IRF	Instrument Response Function
LAT	Large-Area Telescope
LBL	Low-frequency-peaked Bl Lacertae Object
ΛCDM	Lambda Cold Dark Matter
LSS	Large-Scale Structure
MAGIC	Major Atmospheric Gamma-ray Imaging Cherenkov telescopes
PSF	Point-Spread Function
ROI	Region of Interest
SSC	Synchrotron Self Compton
TLA	Three-Letter Acronym
TMLA	Too-Many-Letter Acronym
UHECR	Ultra-High-Energy Cosmic Ray
VERITAS	Very-high-Energy Radiation Imaging Telescope Array System
WHIM	Warm-Hot Intergalactic Medium

Table C.1: List of TLAs and TMLAs.

REFERENCES

Acciari, V. A. et al. 2010, ApJ, 715, L49

Ackermann, M. et al. 2011, ApJ, 743, 171

Aharonian, F. et al. 2007, A&A, 475, L9

—. 2006, A&A, 457, 899

Aharonian, F. A. 2001, in International Cosmic Ray Conference, Vol. 27, International Cosmic Ray Conference, ed. K.-H. Kampert, G. Heinzelmann, & C. Spiering, I250

Aharonian, F. A. 2004, Very high energy cosmic gamma radiation : a crucial window on the extreme Universe, ed. Aharonian, F. A.

Aharonian, F. A., Coppi, P. S., & Voelk, H. J. 1994, ApJ, 423, L5

Ahlers, M. 2011, Phys. Rev. D, 84, 063006

Aielli, G. et al. 2012, Nuclear Instruments and Methods in Physics Research A, 661, 50

Ando, S., & Kusenko, A. 2010, ApJ, 722, L39

Atkins, R. et al. 2004, ApJ, 608, 680

Atwood, W. B. et al. 2009, ApJ, 697, 1071

Beck, R. 2008, in American Institute of Physics Conference Series, Vol. 1085, American Institute of Physics Conference Series, ed. F. A. Aharonian, W. Hofmann, & F. Rieger, 83–96

Bernet, M. L., Miniati, F., Lilly, S. J., Kronberg, P. P., & Dessauges-Zavadsky, M. 2008, Nature, 454, 302

Biermann, L. 1950, Z. Naturforsch., 5

Blasi, P., Burles, S., & Olinto, A. V. 1999, ApJ, 514, L79

Blumenthal, G. R., & Gould, R. J. 1970, Reviews of Modern Physics, 42, 237

Böttcher, M., Dermer, C. D., & Finke, J. D. 2008, ApJ, 679, L9

Bret, A., Gremillet, L., & Dieckmann, M. E. 2010, Physics of Plasmas, 17, 120501

Broderick, A. E., Chang, P., & Pfrommer, C. 2011, ArXiv e-prints

Butcher, J. C. 2008, Numerical Methods for Ordinary Differential Equations, ed. Jackson, J. D.

Bykov, A. M., Paerels, F. B. S., & Petrosian, V. 2008, Space Sci. Rev., 134, 141

Cen, R., & Ostriker, J. P. 1999, ApJ, 514, 1

de Angelis, A., Mansutti, O., Persic, M., & Roncadelli, M. 2009, MNRAS, 394, L21

Dermer, C. D., Cavadini, M., Razzaque, S., Finke, J. D., Chiang, J., & Lott, B. 2011, ApJ, 733, L21

Deyoung, T., & et al. 2010, in 38th COSPAR Scientific Assembly, Vol. 38, 2319

Dolag, K., Grasso, D., Springel, V., & Tkachev, I. 2005, J. Cosmology Astropart. Phys., 1, 9

Dolag, K., Kachelrieß, M., Ostapchenko, S., & Tomàs, R. 2009, ApJ, 703, 1078

Dolag, K., Kachelriess, M., Ostapchenko, S., & Tomàs, R. 2011, ApJ, 727, L4+

Elyiv, A., Neronov, A., & Semikoz, D. V. 2009, Phys. Rev. D, 80, 023010

Essey, W., Ando, S., & Kusenko, A. 2011, Astroparticle Physics, 35, 135

Essey, W., & Kusenko, A. 2010, Astroparticle Physics, 33, 81

—. 2011, ArXiv e-prints

Eungwanichayapant, A., & Aharonian, F. 2009, International Journal of Modern Physics D, 18, 911

Fegan, D. J. 1997, Journal of Physics G Nuclear Physics, 23, 1013

Fossati, G., Maraschi, L., Celotti, A., Comastri, A., & Ghisellini, G. 1998, MNRAS, 299, 433

Franceschini, A., Rodighiero, G., & Vaccari, M. 2008, A&A, 487, 837

Gilmore, R. C., Madau, P., Primack, J. R., Somerville, R. S., & Haardt, F. 2009, MNRAS, 399, 1694

Gould, R. J., & Schréder, G. P. 1967, Physical Review, 155, 1408

Grasso, D., & Rubinstein, H. R. 2001, Phys. Rep., 348, 163

Hanna, D. et al. 2008, Nuclear Instruments and Methods in Physics Research A, 588, 26

Hillas, A. M. 1996, Space Sci. Rev., 75, 17

Hovatta, T., Valtaoja, E., Tornikoski, M., & Lähteenmäki, A. 2009, A&A, 494, 527

Huan, H., Weisgarber, T., Arlen, T., & Wakely, S. P. 2011, ApJ, 735, L28+

Ichiki, K., Inoue, S., & Takahashi, K. 2008, ApJ, 682, 127

Jackson, J. D. 1999, Classical Electrodynamics, ed. Jackson, J. D.

James, F. 2006, Statistical Methods in Experimental Physics: 2nd Edition, ed. James, F. (World Scientific Publishing Co)

Jauch, J. M., & Rohrlich, F. 1976, The theory of photons and electrons. The relativistic quantum field theory of charged particles with spin one-half, ed. Jauch, J. M. & Rohrlich, F.

Jones, F. C. 1968, Physical Review, 167, 1159

Kim, K.-T., Kronberg, P. P., Giovannini, G., & Venturi, T. 1989, Nature, 341, 720

Kolb, E. W., & Turner, M. S. 1990, The early universe., ed. Kolb, E. W. & Turner, M. S.

Kronberg, P. P. 1994, Reports on Progress in Physics, 57, 325

Kronberg, P. P. 2001, in American Institute of Physics Conference Series, Vol. 558, American Institute of Physics Conference Series, ed. F. A. Aharonian & H. J. Völk, 451–462

Kronberg, P. P., Dufton, Q. W., Li, H., & Colgate, S. A. 2001, ApJ, 560, 178

Kronberg, P. P., Kothes, R., Salter, C. J., & Perillat, P. 2007, ApJ, 659, 267

Kronberg, P. P., Lesch, H., & Hopp, U. 1999, ApJ, 511, 56

Kronberg, P. P., & Perry, J. J. 1982, ApJ, 263, 518

Kulsrud, R., Cowley, S. C., Gruzinov, A. V., & Sudan, R. N. 1997a, Phys. Rep., 283, 213

Kulsrud, R. M., Cen, R., Ostriker, J. P., & Ryu, D. 1997b, ApJ, 480, 481

Kusunose, M., & Takahara, F. 2006, ApJ, 651, 113

Li, T., & Ma, Y. 1983, ApJ, 272, 317

Mather, J. C. et al. 1994, ApJ, 420, 439

Mazin, D., & Raue, M. 2007, A&A, 471, 439

MILAGRO Collaboration. 2006, Nuclear Physics B Proceedings Supplements, 151, 101

Murase, K., Takahashi, K., Inoue, S., Ichiki, K., & Nagataki, S. 2008, ApJ, 686, L67

Neronov, A., Semikoz, D., Kachelriess, M., Ostapchenko, S., & Elyiv, A. 2010, ApJ, 719, L130

Neronov, A., & Semikoz, D. V. 2007, JETP Lett., 85, 473

—. 2009, Phys. Rev. D, 80, 123012

Neronov, A., Semikoz, D. V., Tinyakov, P. G., & Tkachev, I. I. 2011, A&A, 526, A90

Neronov, A., & Vovk, I. 2010, Science, 328, 73

Pan, D. C., Vogeley, M. S., Hoyle, F., Choi, Y.-Y., & Park, C. 2012, MNRAS, 421, 926

Peskin, M. E., & Schroeder, D. V. 1995, An Introduction to Quantum Field Theory, ed. Peskin, M. E. & Schroeder, D. V. (Westview Press)

Plaga, R. 1995, Nature, 374, 430

Protheroe, R. J. 1986, MNRAS, 221, 769

Ryu, D., Kang, H., Cho, J., & Das, S. 2008, Science, 320, 909

Sigl, G., Miniati, F., & Enßlin, T. A. 2004, Phys. Rev. D, 70, 043007

Tavecchio, F., Ghisellini, G., Bonnoli, G., & Foschini, L. 2010a, arXiv:1009.1048

Tavecchio, F., Ghisellini, G., Foschini, L., Bonnoli, G., Ghirlanda, G., & Coppi, P. 2010b, MNRAS, 406, L70

Tavecchio, F., Ghisellini, G., Ghirlanda, G., Costamante, L., & Franceschini, A. 2009, MNRAS, 399, L59

Taylor, A. M., Vovk, I., & Neronov, A. 2011, A&A, 529, A144

The Fermi-LAT Collaboration. 2011, ArXiv e-prints

Urry, C. M., & Padovani, P. 1995, PASP, 107, 803

Vovk, I., Taylor, A. M., Semikoz, D., & Neronov, A. 2012, ApJ, 747, L14

Wald, R. M., ed. 1984, General relativity

Weekes, T. C. 1988, Phys. Rep., 160, 1

Widrow, L. M. 2002, Reviews of Modern Physics, 74, 775

Zdziarski, A. A. 1988, ApJ, 335, 786

Zweibel, E. G. 2006, Astronomische Nachrichten, 327, 505